CFD ANALYSIS OF A VISCOUS OPTIMIZED CONICAL WAVE RIDER IN THE MARTIAN ATMOSPHERE

A Project
Presented to
The Faculty of the Department of Aerospace Engineering
San José State University

In Partial Fulfillment
of the Requirements for the Degree
Master of Science in Aerospace Engineering

by
Carlos Pagan
May 2025

approved by
Dr. Yawo Ezunkpe
Faculty Advisor

© 2025

Carlos Pagan

ALL RIGHTS RESERVED

ABSTRACT

CFD ANALYSIS OF A VISCOUS OPTIMIZED CONICAL WAVE RIDER IN THE MARTIAN ATMOSPHERE

by Carlos Pagan

This study investigates the aerodynamic performance of a viscous-optimized conical waverider in the Martian atmosphere using SolidWorks Flow Simulation. Waveriders are hypersonic vehicles that achieve high lift-to-drag ratios (L/D) by riding on their own attached shock waves. This research focuses on evaluating the University of Maryland's optimized waverider design under entry conditions at Mach 19 and two Martian altitudes, 20 km and 30 km across a fully laminar, fully turbulent, and transitional flow regimes.

Simulations show that at lower altitude, the turbulent model produces the highest lift but also the greatest skin friction drag, resulting in the lowest L/D. The transitional flow regime produced the most favorable performance by balancing lift and drag. At higher altitudes, all aerodynamic forces decreased due to the lower density, and the laminar model showed the best efficiency. For both altitudes the pressure drag predictions closely matched referenced values, while friction drag was consistently over predicted, likely due to turbulence modeling and wall resolution limitations.

The results demonstrate that SolidWorks Flow Simulation can be used for preliminary hypersonic design and Martian entry analysis, though higher-fidelity tools are recommended for detailed performance prediction. These findings support the continued development of waverider configurations for future spaceflight applications, including aero-gravity assist and planetary reentry missions.

ACKNOWLEDGMENTS

I would like to express my heartfelt gratitude to my advisor, Dr. Yawo Ezunkpe, whose guidance, expertise, and encouragement have been invaluable. Their insightful feedback and unwavering support helped me navigate the complexities of my project work. I appreciate the time that they have dedicated to mentoring me and their commitment to fostering a collaborative learning environment.

In addition, I would like to acknowledge Dr. Nikos Mourtos, the head of Aerospace Engineering, for their leadership and support within the department. Their vision and dedication to academic excellence have created an enriching environment that has greatly benefited all students. I also want to recognize my fellow students and friends at San Jose State University for their camaraderie and support during this challenging yet rewarding experience.

TABLE OF CONTENTS

LIST OF TABLES

LIST OF FIGURES

Latin Symbols

A	Surface area [m^2]
a, b, c	Triangle side lengths for area calculation
C_L	Coefficient of lift, $C_L = \frac{L}{qS}$
C_D	Coefficient of drag, $C_D = \frac{D}{qS}$
C_{D_p}	Coefficient of pressure drag
C_{D_f}	Coefficient of friction drag
C_M	Pitching moment coefficient
C_f	Local skin friction coefficient
$C_{f,TR}$	Transitional skin friction coefficient
D	Total drag force [N]
D_p	Pressure drag force [N]
D_f	Friction drag force [N]
E	Total energy per unit mass [J/kg]
e	Internal energy [J/kg]
F	Force [N]; also used in optimization and real gas formulations
g	Function used in friction correlation
H	Total enthalpy per unit mass [J/kg]
h	Static enthalpy per unit mass [J/kg]
k	Turbulent kinetic energy
l	Waverider centerline length [m]
L	Lift force [N]
M	Mach number
M_e	Edge Mach number
m	Mass flow rate [kg/s]
p	Static pressure [Pa]
p_∞	Freestream pressure [Pa]
q	Dynamic pressure [Pa]
q_w	Wall heat flux [W/m^2]
Re	Reynolds number
S	Reference area (wetted or planform) [m^2]
T	Temperature [K]
T_w	Wall temperature [K]
T_0	Total (stagnation) temperature [K]
u, v, w	Velocity components [m/s]
u_∞	Freestream velocity [m/s]
V	Total velocity magnitude [m/s]
V_c	Circular orbit velocity [m/s]
V_r, V_θ	Velocity components in conical coordinates
x, y, z	Cartesian coordinates [m]
Δt	Time step [s]

Greek Symbols

α Reflection coefficient (simplex method)
β Contraction coefficient (simplex method); also flow angle
δ Boundary layer thickness [m]; also deflection angle
ε Turbulent dissipation rate
γ Ratio of specific heats
κ von Kármán constant, typically 0.405
λ Viscous interaction parameter
μ Dynamic viscosity [Pa·s]
ρ Density [kg/m^3]
σ Stefan–Boltzmann constant [W/m^{2}K^4]
τ Shear stress [Pa]
θ Flow deflection angle [rad or deg]; also angular coordinate
ϕ Electric potential (used in Joule heating)

Operators and Derived Quantities

∇ Gradient operator
$\int$ Integral operator
$\dot{m}$ Mass flow rate [kg/s]
q'' Heat flux [W/m^2]
τ_w Wall shear stress [Pa]
ψ Stream function
δ_p Pressure correction
U Vector of conserved variables

1. Introduction

1.1 Motivation

The motivation behind this project is to conduct preliminary research into the aerodynamics of an air-breathing single-stage-to-orbit (SSTO) space vehicle operating at extreme hypersonic speeds. Unlike traditional multi-stage launch systems that rely on vertically stacked expendable rocket stages, an SSTO vehicle is designed to achieve orbital velocity in a single, reusable platform. This concept, if realized, promises a revolutionary leap in space access by drastically reducing launch costs, increasing flight frequency, and improving system reliability through full reusability.

A key enabler of SSTO feasibility lies in efficient hypersonic aerodynamics and propulsion integration. Since the vehicle must travel through the atmosphere for a substantial portion of its ascent, minimization of aerodynamic drag and thermal loads is critical. Here, the waverider configuration emerges as a highly suitable candidate. Waveriders are designed to ”ride” their attached shock wave, maximizing lift while minimizing wave drag. This property is particularly valuable in the high-Mach, high-altitude regime encountered both during the acceleration to orbit and during atmospheric reentry, where thermal and structural loads are severe.

The goal of this project is to replicate and analyze existing waverider designs using Computational Fluid Dynamics (CFD), with a focus on understanding their behavior at high Mach numbers. By reproducing validated results from known literature, the aim is to deepen understanding of waverider performance and assess its applicability for an air-breathing orbital vehicle. This work serves both as a validation exercise for CFD tools in extreme hypersonic conditions and as a foundation for future design optimization, potentially extending toward planetary entry scenarios such as Mars, where similar aerodynamic and thermal challenges arise.

1.2 Literature Review

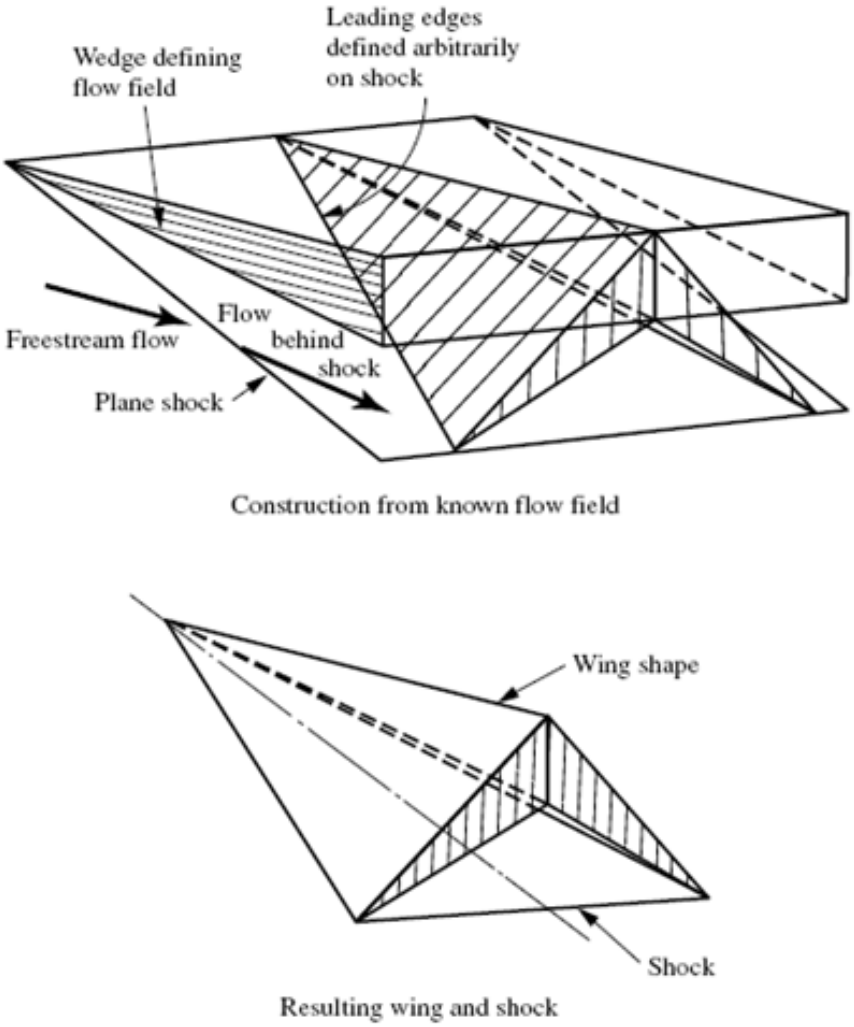

Figure 1.1. Caret wing (1).

A wave rider is a specially shaped vehicle design which uses attached shock waves generated when going faster than the speed of sound to generate additional lift. This increases its lift-to-drag ratio in a phenomenon known as compression lift. The idea was first proposed by Terence Nonweiler in 1959 (2). Nonweiler's original design was based on planar 2d shocks, used a caret wing shape which had sharp leading edges, and did not include viscous effects. Researchers later updated the caret wing design using 3d conical shock theory to produce a class of wave riders known as conical flow wave riders. Both the caret wing and

conical flow wave rider designs do not take into account the viscous effects of the fluid. The third breakthrough in wave rider design came when computational power increased to the point that CFD could be used to combine viscous effects with 3d conical shock theory and optimization to produce another class of wave riders known as viscous optimized wave riders (3).

Figure 1.2. Prof. Terence Nonweiler (4).

Wave riders are ideal for supersonic and hypersonic flight due to the efficient use of the shockwaves generated to increase lift and decrease drag. This design creates the greatest lift-to-drag ratio at high Mach numbers (5). Another advantage that wave riders have as a space vehicle compared to the space shuttle and blunt body style reentry capsules is its ability to maneuver during reentry. At the upper atmospheres, during the reentry phase of flight at Mach 25, the thin atmosphere does not provide enough flow over the control surfaces of the space shuttle type vehicle for maneuvering. A wave rider would be able to take advantage of the compression lift for maneuvering during reentry by controlling its lift distribution.

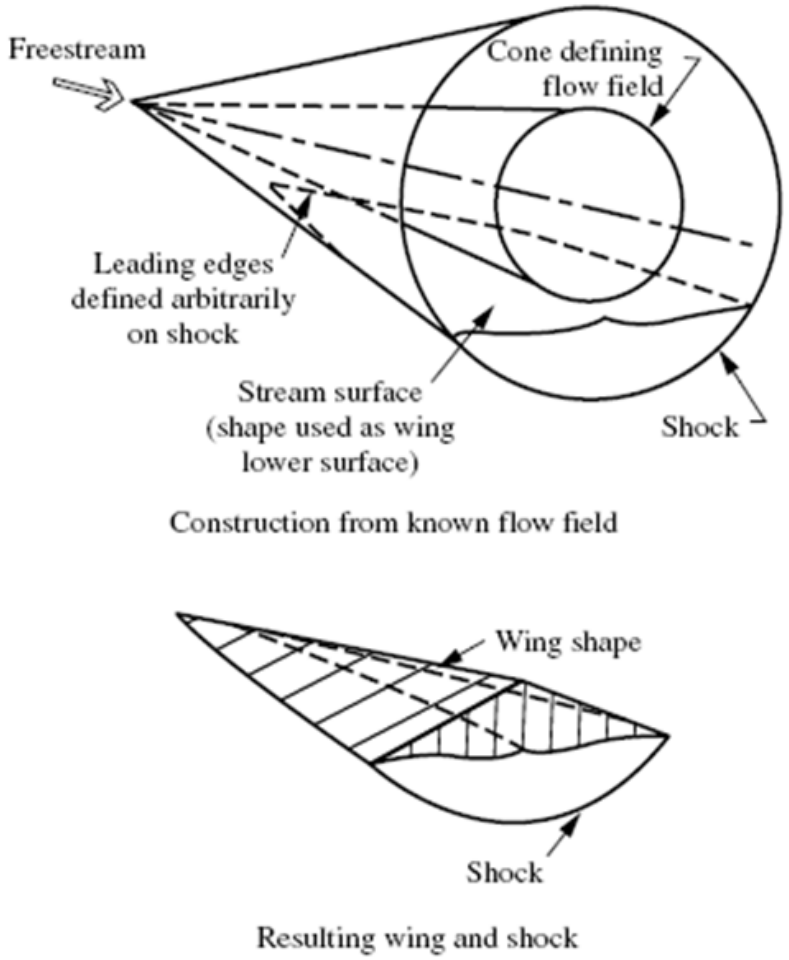

Figure 1.3. Conical flow wave rider (6).

In space, wave riders can take advantage of the aerogravity assist maneuver (7). The aerogravity assist maneuver differs from a traditional gravity assist by having the spacecraft fly into the edge of the upper atmosphere of a planetary body and use compression lift to augment the gravity assist. The additional compression lift results in a higher change in velocity compared to a pure gravity assist.

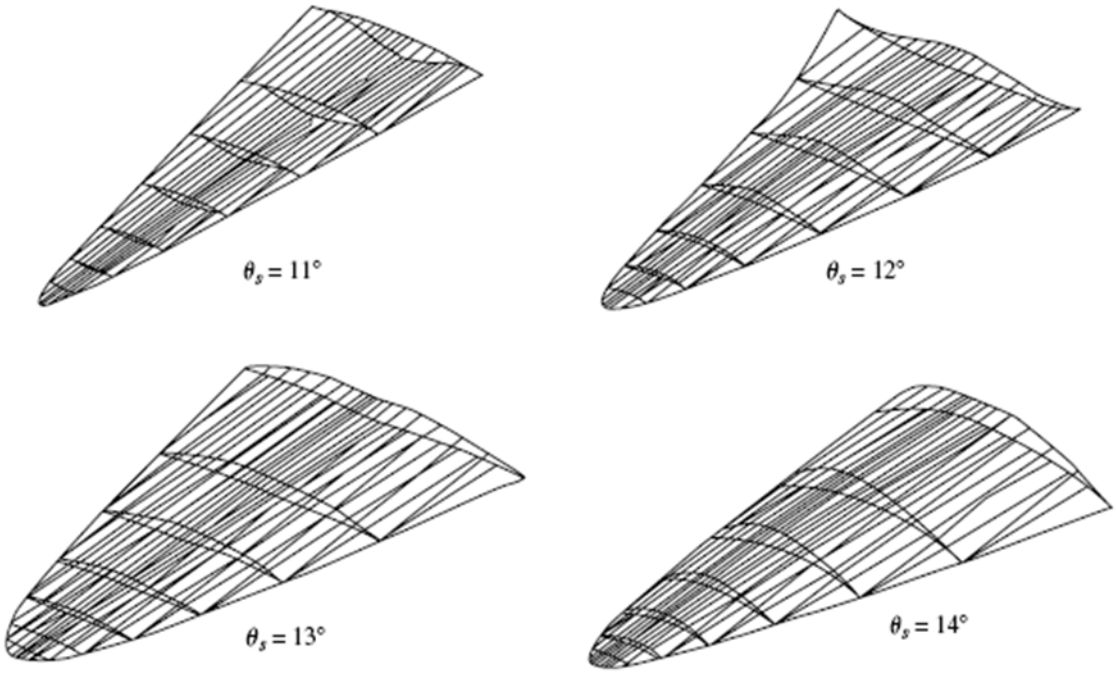

Figure 1.4. Viscous optimized wave rider (8).

The Mach 25 capable single stage to orbit space vehicle idea is based on the X-30 National Aero-Space Plane (9). The X-30 National Aero-Space Plane was a joint project between NASA and the Department of Defense from 1986-1993. The goal of the project was to develop a single stage to orbit spacecraft that could take off and land like a conventional aircraft.

Figure 1.5. X-30 hypersonic scramjet SSTO concept (10).

The X-30 featured a wave rider design with a flat conical nose and integrated engine and fuselage. The propulsion system consisted of a turbine-based combined-cycle scramjet engine and used slush hydrogen as fuel. The slush hydrogen would also be used to keep the surface of the airframe cool (11). The X-30 would take off like a conventional aircraft from a runway and accelerate to Mach 25 to reach orbit without the aid of rockets. It was eventually canceled when it was determined that Mach 20 was the theoretical maximum achievable speed because of the technological limitations of the time. Mach 25 was the theoretical speed required to achieve orbit without using rockets. The research done on the X-30 was then carried over to the X-43 program.

Wave riders are designed to travel at hypersonic speeds, which are defined as speeds greater than Mach 5 (approximately 3,800 miles per hour or 6,200 kilometers per hour). These vehicles utilize a unique aerodynamic phenomenon called ”shockwave compression lift” to generate lift and achieve stable flight at hypersonic speeds. Wave riders are specifically designed to ride on the shockwaves generated by their own flight, allowing them to efficiently travel at extremely high speeds.

Figure 1.6. X-43 (12).

To understand how hypersonic wave riders work, it is important to grasp the basic aerodynamic principles involved. At hypersonic speeds, the air surrounding an aircraft becomes highly compressed due to the intense pressure generated by its motion. This compression leads to the formation of shockwaves, which are abrupt changes in air density and temperature.

Conventional aircraft typically aim to minimize the effects of shockwaves, as they can cause drag and instability. However, wave riders take advantage of these shock waves to generate lift and maintain stability. By carefully shaping the body and wings of the vehicle, engineers can create a lifting surface that interacts with the shock wave in a beneficial way.

Shockwave compression lift is the key concept behind hypersonic wave rider design. When an aircraft reaches hypersonic speeds, the shockwaves it generates compress the air beneath its wings. This compression increases the air density and creates additional lift force on the aircraft. Wave riders are specifically designed with a sharp leading edge and

a wedge-like shape to maximize the compression effects. The leading edge of the vehicle creates a strong shockwave that compresses the air underneath, while the wedge shape helps to maintain stability by distributing the forces evenly across the vehicle's surface (13).

By riding on these shockwaves and utilizing shockwave compression lift, hypersonic wave riders can achieve stable flight at hypersonic speeds with relatively low drag. This enables them to travel faster and more efficiently than traditional aircraft designs. Designing and operating hypersonic wave riders presents numerous challenges and limitations. The extreme speeds involved introduce significant thermal and aerodynamic stresses on the vehicle, requiring advanced materials and cooling systems to withstand the high temperatures generated by air friction.

Boundary layer shock interaction is especially important and is an important phenomenon that needs to be controlled at hypersonic speeds. Boundary layer shock interaction refers to the phenomenon that occurs when a shock wave interacts with the boundary layer of a fluid flow (14). In aerodynamics, the boundary layer is the thin layer of fluid adjacent to a solid surface where viscous effects dominate. When a shock wave impinges on this boundary layer, it can have significant effects on the flow properties and lead to various flow phenomena.

When a shock wave interacts with the boundary layer, several important phenomena occur. These include shockwave/boundary-layer interaction (SBLI), shock-induced separation, shock-induced transition, and shock-induced combustion instability. Understanding these interactions is crucial for optimizing aerodynamic designs at hypersonic speeds and improving the performance of the wave rider concept (14).

SBLI is a complex phenomenon that arises due to the interaction between the high-pressure region of a shock wave and the low-pressure region within the boundary layer. The interaction can lead to changes in flow properties such as pressure, temperature, density, and velocity. SBLI can cause significant alterations in the boundary layer structure and influence the overall aerodynamic characteristics of a vehicle or aircraft and has been shown to cause damage and control surface problems in the X-15.

SBLI effects include shock-induced separation, shock-induced transition, and shock-induced combustion instability within the propulsion system.

Shock-induced separation refers to the separation of the boundary layer from a solid surface due to the presence of a shock wave. This phenomenon is particularly relevant in high-speed flows where shocks can cause adverse pressure gradients leading to flow separation. Separation can result in increased drag, reduced lift, and compromised control authority, impacting the performance and maneuverability of an aircraft or vehicle.

Shock-induced transition occurs when a shock wave triggers a laminar-to-turbulent transition within the boundary layer. The transition from laminar to turbulent flow alters the flow characteristics and can affect heat transfer rates, skin friction, and overall aerodynamic performance. Controlling shock-induced transition is essential for designing high-performance inlets for hypersonic vehicles and optimizing the heat transfer on the skin surface.

In the context of scramjet engines or supersonic combustion, shock-induced combustion instability can occur when a shock wave interacts with the combustion process. This interaction can lead to unsteady combustion, pressure oscillations, and even flame extinction. Managing

shock-induced combustion instability is needed to ensure stable and efficient combustion in high-speed propulsion systems.

Another challenge is the control and stability of wave riders at hypersonic speeds. The interaction between shockwaves and the vehicle's surfaces can lead to complex flow patterns and instabilities, making it vital to develop sophisticated control systems that can maintain stability in such conditions. Because of the immense speed hypersonic vehicles travel, aerodynamic forces are amplified, and the outside environment becomes hazardous due to intense heat, and other atmospheric effects. Challenges in the control and stability of wave riders are numerous and include dealing with the significant increase in aerodynamic forces, such as drag, lift, and pitching moment at hypersonic speeds. These forces can cause instability and affect the vehicle's control. The intense heat generated during hypersonic flight can cause thermal degradation of materials, affecting the vehicle's structure and performance. The atmosphere's density and composition change with altitude, leading to variations in aerodynamic forces and heat transfer rates.

Still greater challenge hypersonic vehicles have is the limited control surfaces due to their high speeds, making it difficult to maintain stability and control. On reentry, the Space Shuttle can reach speeds of up to Mach 25, with the control surfaces having no effect on maneuvering.

The high velocity also makes it a challenge for data processing and communications. The high data rates generated during hypersonic flight require much more powerful computers with advanced data processing and communication systems to manage and transmit the information required for control and stability.

Several strategies have been proposed to address the challenges of controlling and maintaining stability in hypersonic vehicles such as using model-based control, adaptive control, and machine learning algorithms to overcome the limitations of traditional control systems and maintain stability at hypersonic speeds. Optimizing the vehicle's shape and using modern advanced materials can reduce aerodynamic forces and improve stability.

At such high velocities, aerodynamic heating will be a major challenge and will require active cooling systems, such as cryogenic cooling or liquid cooling, to be used in combination with thermal protection systems, like ablative or reusable insulation. This is essential to mitigate the effects of intense heat on the vehicle's structure and performance. Advanced sensors that can withstand the intense heat will need to be developed to be able to provide accurate data for the fly-by-wire control system for stability at hypersonic speeds. The use of advanced materials and manufacturing techniques, such as metal 3D printing, will be required to improve the vehicle's structural integrity and heat dissipation.

Additionally, the propulsion systems for hypersonic wave riders must be capable of providing sufficient thrust to overcome drag forces at hypersonic speeds. Various propulsion technologies, such as ramjets, and scramjets are being explored to meet these requirements.

Scramjet (Supersonic combustion ramjet) engines are a key technology for achieving hypersonic speeds. Unlike traditional jet engines that rely on rotating compressor blades to compress incoming air, scramjets compress air using supersonic combustion. This allows for efficient propulsion at extremely high speeds. Scramjets operate by ingesting atmospheric air

through an inlet and then compressing it before mixing it with fuel. The mixture is ignited and expands through a nozzle, generating thrust. Since scramjets rely on atmospheric oxygen for combustion, they are most effective at high altitudes where the air density is low.

Ramjet engines are similar to scramjets but operate at lower speeds. They compress incoming air using subsonic combustion rather than supersonic combustion. Ramjets are typically used for speeds up to Mach 5 and can transition into scramjets at higher speeds. Ramjets work by slowing down incoming air to subsonic speeds using a diffuser, compressing it, mixing it with fuel, igniting the mixture, and then accelerating it through a nozzle. While ramjets provide efficient propulsion at high speeds, they require initial acceleration before they can start operating effectively.

Ramjets and scramjets have limitations in that they cannot be started on their own and can only operate when the vehicle is already moving faster than the speed of sound. A possible solution being developed is the use of Turbine or rocket-based combined cycle engines.

A turbine-based combined cycle propulsion system (TBCC) is a turbine engine combined with a ramjet and scramjet. It will allow the vehicle to take off using a traditional turbojet engine and transition to ramjet/scramjet operation when it reaches the speed of sound (15).

Figure 1.7. NASA combined cycle engine large scale inlet mode transition experiment (CCE LIMX) (15).

Rocket-based combined cycle (RBCC) engines combine elements of both scramjets and rockets. The main components of an RBCC engine typically include a rocket combustion chamber, an air-breathing inlet, a supersonic combustion ramjet (scramjet), and an exhaust nozzle. The rocket combustion chamber is responsible for providing initial thrust during takeoff and ascent. Once the vehicle reaches a certain altitude and speed, the air-breathing inlet begins to collect atmospheric air, which is then compressed and mixed with fuel in the scramjet. The mixture is ignited and burned in the scramjet, generating additional thrust. Finally, the exhaust gases are expelled through the exhaust nozzle, providing further propulsion.

The RBCC engine operates in different modes depending on the flight conditions. At lower speeds, it functions as a ramjet or scramjet, utilizing atmospheric air for combustion. As the vehicle accelerates and climbs to higher altitudes, it transitions to rocket mode, where

it carries its own oxidizer and operates similarly to traditional rockets. An RBCC engine was originally proposed for the X-30 National Space Plane concept.

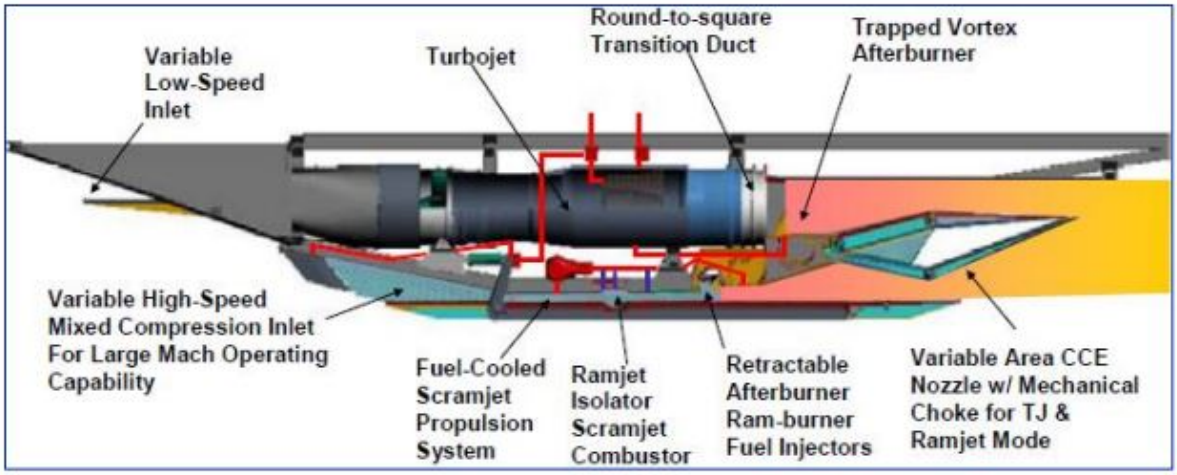

Figure 1.8. Turbine based combined cycle (TBCC) propulsion system (15).

As previously stated, the Wave rider design concept was first developed by Terence Nonweiler, a British aerospace engineer, in the 1950s. Nonweiler's concept aimed to create a supersonic aircraft that could travel at hypersonic speeds while generating lift through the compression of air underneath its wings, rather than relying solely on conventional aerodynamic lift. Nonweiler proposed that by shaping an aircraft's body in a specific manner, it would be possible to capture and utilize the shockwaves generated during hypersonic flight. This unique design would allow for increased stability and control at high speeds, as well as improved aerodynamic efficiency.

Early research into hypersonic flight began with the X-15 program. The X-15 was a rocket-powered aircraft designed to be air-launched from a modified B-52 bomber. It featured a slender fuselage with a delta-wing configuration, providing stability during high-speed flight. The aircraft's structure was primarily constructed from titanium alloy, which allowed it to withstand the intense heat generated during re-entry. The X-15 reached speeds up to Mach 6.7 and was used to gather valuable data on hypersonic flight characteristics. These early experiments laid the foundation for future hypersonic designs (16).

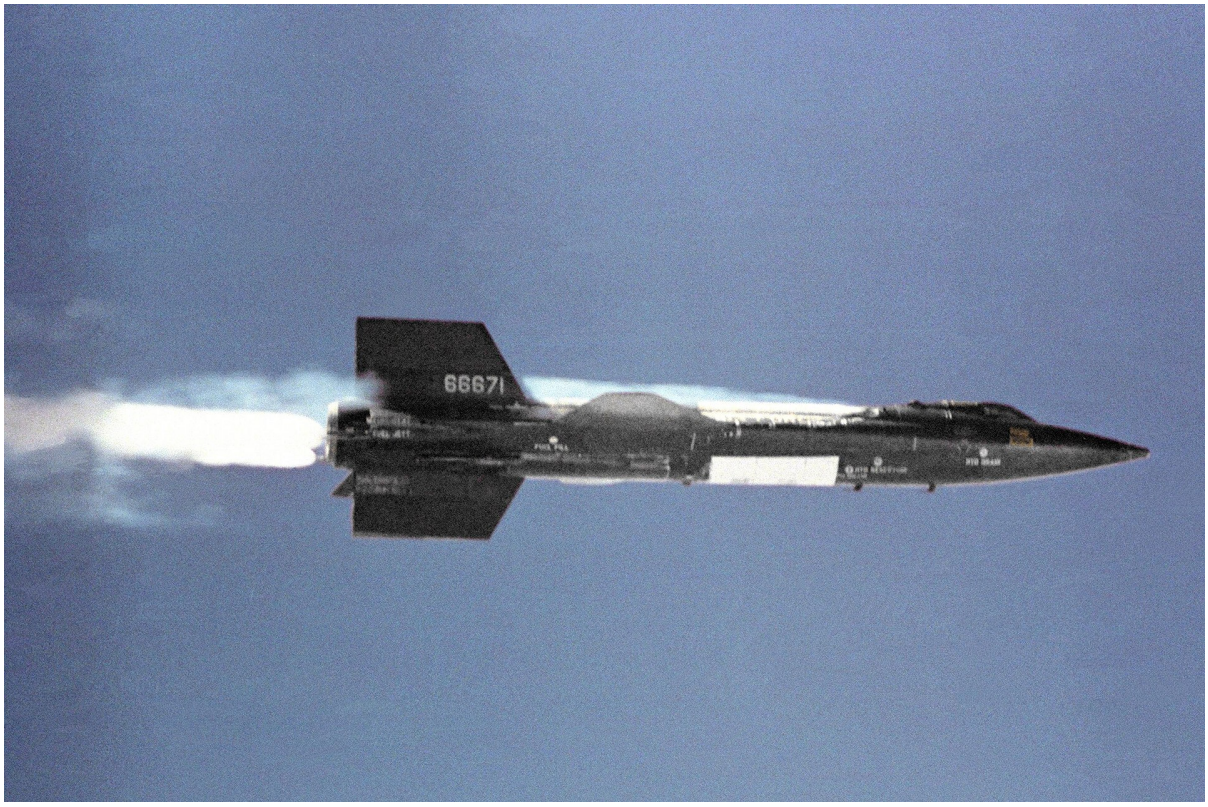

Figure 1.9. North American X-15 (16).

The X-15 was powered by a Reaction Motors XLR-99 rocket engine, which burned a mixture of liquid oxygen and anhydrous ammonia. The engine provided thrust for the aircraft during its high-speed flights, enabling it to reach speeds exceeding Mach 6 (approximately 4,520 mph) and altitudes above 350,000 feet. In the 1980s, the X-30 National Aerospace Plane (NASP) program made significant progress in hypersonic research. The X-30 NASP program was a joint research effort by NASA and the United States Department of Defense (DoD) in the late 1980s and early 1990s. The primary objective of the program was to develop a reusable spaceplane that could take off from conventional runways, reach hypersonic speeds, and then return to Earth for rapid turnaround and reuse. The National Aerospace Plane was also to be single-stage-to-orbit and capable of flying at speeds up to Mach 25. Various configurations were explored, including air-breathing engines combined with rocket propulsion systems. The proposed spaceplane would have been powered by a revolutionary air-breathing engine called the Combined-Cycle Engine (CCE), which was designed to operate efficiently at both subsonic and supersonic speeds. The X-30 NASP program faced numerous technological challenges that ultimately contributed to its cancellation in 1993. Some of the key challenges included:

- Thermal Management: The extreme temperatures generated during hypersonic flight posed significant challenges in terms of thermal protection systems and managing heat transfer throughout the vehicle structure.
- Structural Integrity: The high speeds and dynamic loads experienced during hypersonic flight required the development of lightweight yet structurally robust materials and designs.
- Propulsion System: The development of the air-breathing CCE engine proved to be a significant technical challenge, as it required complex integration of various propulsion modes (ramjet, scramjet, and rocket) into a single engine.
- Cost and Funding: The X-30 NASP program faced increasing budgetary pressures and concerns over its cost-effectiveness, leading to its eventual cancellation.

Despite significant progress in developing advanced technologies for hypersonic flight, the X-30 NASP program was officially canceled in 1993 due to technical difficulties, schedule delays, and rising costs. The cancellation of the program marked a shift in priorities for both NASA and the DoD, with subsequent focus on other space transportation initiatives such as the Space Shuttle program and the development of expendable launch vehicles.

However, the research conducted under the X-30 NASP program laid the foundation for future advancements in hypersonic flight and aerospace technology. Many of the lessons learned from this program have been applied to subsequent projects, including current efforts to develop reusable spaceplanes and hypersonic vehicles. The next significant research project into hypersonic flight was the X-43 program. The X-43 aircraft was an experimental hypersonic aircraft developed by NASA. The X-43A specifically focuses on the development of scramjet technology and has set several speed records for an air-breathing aircraft. The X-43A is an unmanned aircraft designed to fly at hypersonic speeds, which are speeds greater than Mach 5 (five times the speed of sound). It was developed by NASA's Dryden Flight Research Center (now Armstrong Flight Research Center) in collaboration with other industry partners. The primary goal of the X-43A program was to demonstrate the feasibility and effectiveness of scramjet engines for high-speed flight.

The X-43A aircraft underwent a series of flight tests to validate the performance and capabilities of scramjet technology. These tests involved launching the aircraft from a B-52 bomber at high altitudes and speeds, after which it would separate and ignite its scramjet engine. The X-43A would then fly autonomously at hypersonic speeds, collecting data on aerodynamics, propulsion, and other relevant parameters.

Figure 1.10. X-43A under B-52 (17)

The initial flight tests of the X-43A were conducted using a modified Pegasus rocket booster to accelerate the aircraft to its desired speed and altitude. Later flights utilized an air-launch method, where the X-43A was dropped from a B-52 bomber before igniting its scramjet engine. The data collected from these flight tests helped researchers gain valuable insights into hypersonic flight and scramjet technology. It contributed to advancements in aerodynamics, propulsion systems, materials science, and other areas related to high-speed flight (12).

The success of the X-43A program paved the way for future endeavors such as the Boeing X-51 Wave rider program. In the early 2000s, the United States Air Force (USAF) initiated the X-51 program to develop a practical hypersonic wave rider vehicle. Boeing was awarded the contract to build and test the X-51 Wave rider demonstrator. This unmanned vehicle was designed to be air-launched from a B-52 bomber and reach speeds up to Mach 5. The X-51 utilized a scramjet engine and had a slender, missile-like shape optimized for

high-speed flight. It successfully completed several test flights, including a record-breaking flight in 2013 where it sustained hypersonic speeds for over six minutes (12).

In 2003 the Defense Advanced Research Projects Agency (DARPA) launched the Falcon (Force Application and Launch from Continental United States) project, aiming to develop an operational hypersonic wave rider vehicle. The project focuses on developing technologies for responsive and affordable access to space. Under the Falcon program, various wave rider designs have been explored, including the Hypersonic Technology Vehicle 2 (HTV-2) and the Hypersonic Air-breathing Weapon Concept (HAWC). These vehicles incorporate advanced materials, improved aerodynamics, and state-of-the-art propulsion systems to achieve sustained hypersonic flight (18). Hypersonic wave rider technology continues to evolve rapidly, with ongoing research and development efforts worldwide. Several countries, including the United States, China, Russia, and Australia, are actively pursuing hypersonic capabilities.

Figure 1.11. DARPA FALCON project (18).

In recent years, advancements in materials science, computational modeling, and propulsion systems have enabled the design of more efficient and capable hypersonic wave riders. Future applications of this technology include military reconnaissance, space access, and high-speed transportation.

During the Cold War, the Soviet Union also made significant contributions to hypersonic wave rider research. In the 1960s, Soviet scientists developed the concept of a "lifting reentry vehicle" (LRV) as part of their space program. The LRV was designed to return cosmonauts from orbit to Earth and featured a wave rider-like shape to enhance its aerodynamic performance during reentry. Additionally, the Soviet Union conducted extensive research on hypersonic flight with their Buran space shuttle program. Although the Buran was not a wave rider per se, it incorporated many design principles relevant to hypersonic flight, including advanced thermal protection systems and aerodynamic configurations suitable for high-speed travel (19).

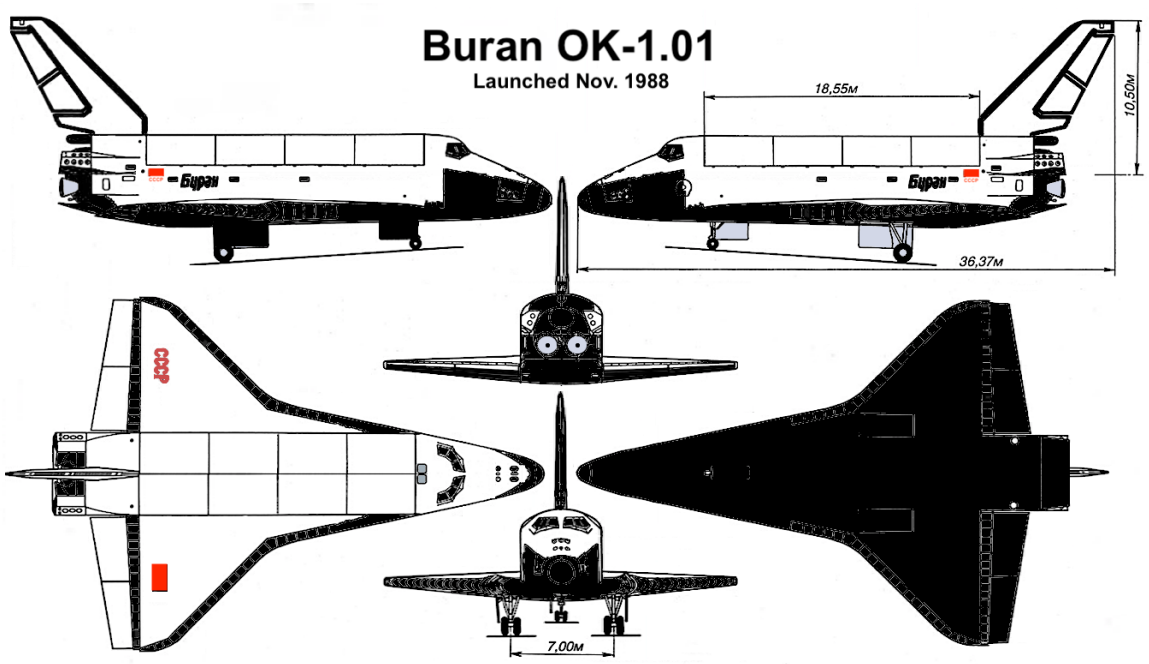

Figure 1.12. USSR Buran (19).

Several countries have continued to invest in hypersonic wave rider technology, aiming to develop practical applications for both civilian and military purposes. Notably, China has made significant strides in this field. In 2018, China successfully tested its Xingkong-2 (Starry Sky-2) hypersonic wave rider vehicle, which reached speeds up to Mach 6 (approximately 4,563 mph or 7,346 km/h). This achievement marked a major milestone in China's pursuit of hypersonic technology (20). The United States has also intensified its efforts in hypersonic research and development. The Defense Advanced Research Projects Agency (DARPA) has

been actively involved in various hypersonic projects, including the Hypersonic Air-breathing Weapon Concept (HAWC) program. This program aims to develop an air-launched hypersonic cruise missile using wave rider technology.

Figure 1.13. China's Starry Sky 2 (20).

The development of hypersonic wave riders has the potential to revolutionize transportation, defense, and space exploration. Hypersonic passenger aircraft could significantly reduce travel times for long-haul flights, enabling faster global connectivity. In the military domain, hypersonic wave riders could provide rapid response capabilities and enhanced maneuverability, challenging existing defense systems. Furthermore, the knowledge gained from hypersonic research may contribute to advancements in space exploration, reentry vehicles, and satellite deployment.

Hypersonic wave riders have numerous practical applications including military, commercial and Space. In the military domain, hypersonic propulsion offers several advantages. Hypersonic weapons can travel at high speeds, making them difficult to intercept or defend against. They provide shorter response times and increased precision for striking time-sensitive targets. Additionally, hypersonic vehicles can be used for reconnaissance purposes due to their ability to cover large distances quickly. Hypersonic propulsion also holds potential for commercial applications such as high-speed passenger travel. With hypersonic aircraft, long-distance flights could be completed in significantly shorter time frames. However, challenges such as cost-effectiveness, safety considerations, and environmental impact need to be addressed before commercial hypersonic travel becomes a reality.

Wave riders will play a crucial role in advancing space exploration capabilities. The ability to reach hypersonic speeds will lead to SSTO and reduce the time for launch. Wave rider technology could be used in spacecraft reentry vehicles, allowing them to safely return to Earth from orbit at hypersonic speeds. The unique shape also allows the use of an aerogravity assist maneuver for inter planetary travel (21).

1.3 Project Proposal

This project aims to evaluate the aerodynamic performance of a conical viscous-optimized waverider under Martian atmospheric entry conditions using SolidWorks Flow Simulation CFD. Hypersonic waveriders are designed to ride along their own attached shock waves, yielding exceptionally high lift-to-drag ratios (L/D)—a critical aerodynamic feature for vehicles undergoing planetary entry at extreme speeds. The conical viscous-optimized waverider further improves traditional inviscid designs by accounting for boundary layer development and viscous effects, which are especially significant in the low-density, carbon dioxide rich Martian atmosphere.

Mars presents a complex entry environment. Its thin atmosphere, roughly 1% the density of Earth's, leads to low Reynolds numbers, more pronounced viscous interactions, and altered shock layer behavior. In such an environment, even small aerodynamic inefficiencies can drastically affect deceleration, heating, and trajectory control. Accurate aerodynamic modeling is essential for designing vehicles that can survive and perform well during entry, descent, and landing phases. Waveriders, with their superior high-speed aerodynamic performance, are strong candidates for these missions—particularly when integrated with gravity assist maneuvers used in interplanetary flight (21).

In this study, SolidWorks Flow Simulation will be used to model the flow around a conical viscous-optimized waverider geometry under conditions that mimic those encountered during gravity-assisted Martian entry. The simulation will estimate surface pressure distribution, skin friction, heat flux, and most importantly, the lift-to-drag ratio at different altitudes and entry angles. Although SolidWorks is traditionally used for subsonic and low-supersonic applications, its performance will be evaluated under extreme hypersonic conditions. The results will be compared with existing research to assess the accuracy, suitability, and validity of SolidWorks Flow Simulation.

1.4 Methodology

The waverider model selected for this study is derived from the University of Maryland's viscous-optimized waverider design, as presented in the foundational work by Anderson Jr. (21). Unlike conventional waverider geometries that are typically derived from inviscid flow assumptions, this design incorporates the effects of viscous boundary layers, which become increasingly significant in low Reynolds number, low-density environments such as the Martian atmosphere. By accounting for viscous effects during the shaping process, the model offers more accurate predictions of real-world aerodynamic behavior, particularly in areas

critical to hypersonic planetary entry, including aerodynamic heating, shear stress distribution, and flow separation control. These characteristics are essential for assessing the feasibility and survivability of entry vehicles operating at high Mach numbers in extraterrestrial atmospheres.

To support computational analysis, a three-dimensional conical waverider geometry—based on this viscous-optimized design—has been sourced from the open-access modeling repository Thingiverse (22). The geometry closely follows the parameters established in the University of Maryland's Martian waverider study and captures the essential aerodynamic features needed for hypersonic CFD evaluation, including a sharp leading edge, curved compression surface, and shock-adapted body profile. These features ensure proper shock attachment and optimal lift generation during high-speed flight, making the model suitable for detailed simulation under planetary entry conditions.

The 3D waverider model will be imported into SolidWorks Flow Simulation, a commercial CFD tool integrated within the SolidWorks CAD environment. The simulation will be set up to model a high-speed compressible flow environment at Mach 19, representing a realistic velocity for a spacecraft entering Mars' atmosphere for a lift enhanced gravity-assist maneuver.

The Martian atmospheric conditions will be defined at two characteristic altitudes, 20 km, and 30 km to reflect realistic entry interface conditions and compare to previous work (21). Each scenario will incorporate Mars-specific environmental parameters, including ambient pressure, temperature, and a carbon dioxide-dominated atmospheric composition, consistent with the Mars Global Reference Atmosphere. These conditions are essential to correctly model the thermodynamic behavior of the gas, capture shock-layer development, and replicate the aerothermal environment experienced during entry. To enhance accuracy, the CFD setup will include laminar-to-turbulent transition, as this can significantly affect thermal loads and pressure distribution during hypersonic entry in thin atmospheres.

The simulation results will provide detailed insight into the vehicle's aerodynamic performance, including the lift-to-drag ratio, surface pressure coefficients, heat flux, and shear stress distributions. The analysis will also assess the capability and accuracy of SolidWorks Flow Simulation when applied to extreme hypersonic conditions outside its conventional subsonic and transonic use cases.

2. Wave Rider Design Methodology

2.1 Caret Wing

In 1959, Prof. Terence Nonweiler came up with the wave rider idea while working on a reusable reentry vehicle for the British space program. His design methodology relied on known solutions to an inviscid flow field using the $\theta - \beta - M$ relation shown below as equation 2.1.

$$\tan(\theta) = \frac{2\cot(\beta)}{M^2 \sin^2(\beta) - 1} \tag{2.1}$$

First, a design Mach number is selected. Then a 2D flow field for an arbitrary wedge with a half angle θ was solved using equation 2.1. The solution to the 2D flow field gives the deflection angle of the shock wave β. Figure 2.1 shows the oblique shock line generated by the wedge in green.

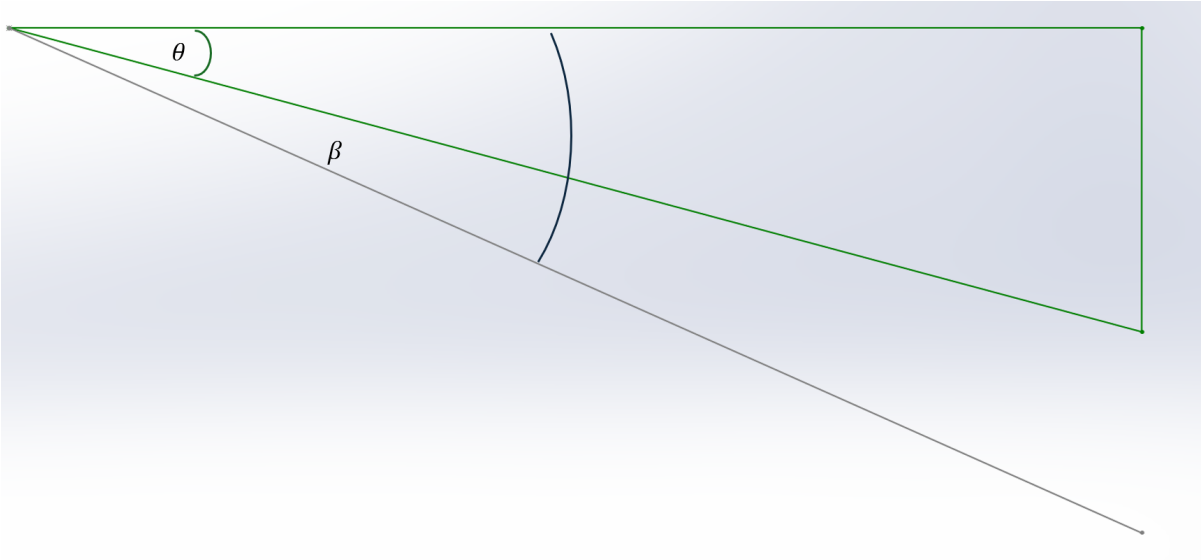

Figure 2.1. 2D wedge with oblique shock.

This 2D wedge can be extended to an infinitely long 3D wedge and the shock line becomes a shock plane as shown in figure 2.2. Then an arbitrary surface is chosen that connects from the top of the wedge to the bottom of the shock plane in the direction perpendicular to the flow as shown in Figures 2.3 and 2.4. This forms the side profile of the caret wing and ensures that the oblique shock remains attached to the leading edges of the caret wing.

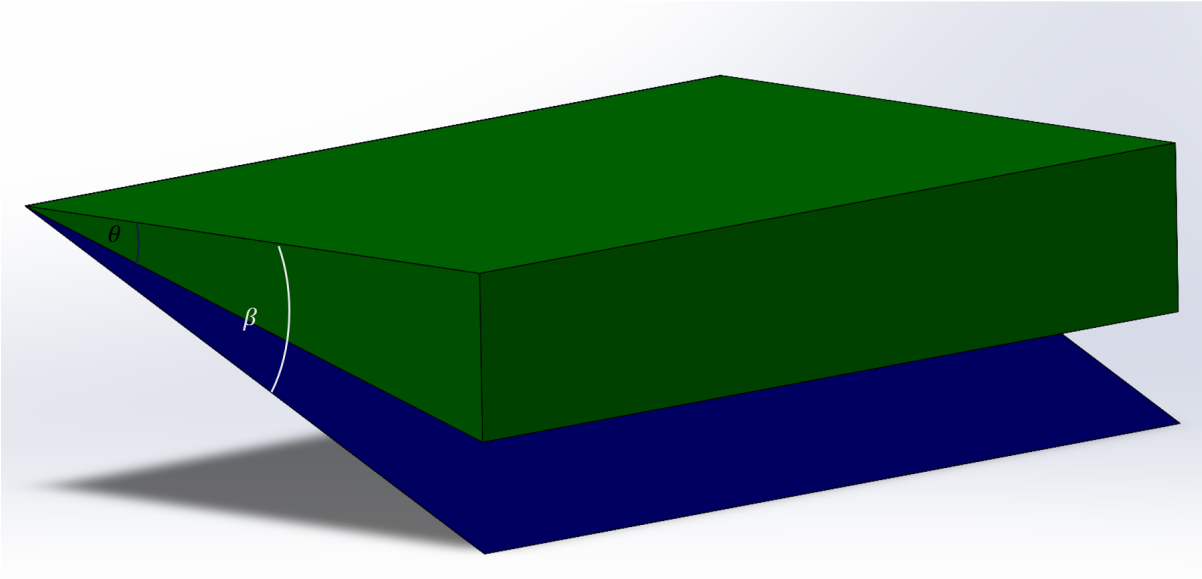

Figure 2.2. 3D wedge with oblique shock plane.

The bottom profile of the caret wing is generated by following the streamlines of the flow which form a streamsurface. This is done by solving the following set of equations:

$$\psi(x,y) = constant \tag{2.2}$$

$$u = \frac{\partial \psi}{\partial y} \tag{2.3}$$

$$v = -\frac{\partial \psi}{\partial x} \tag{2.4}$$

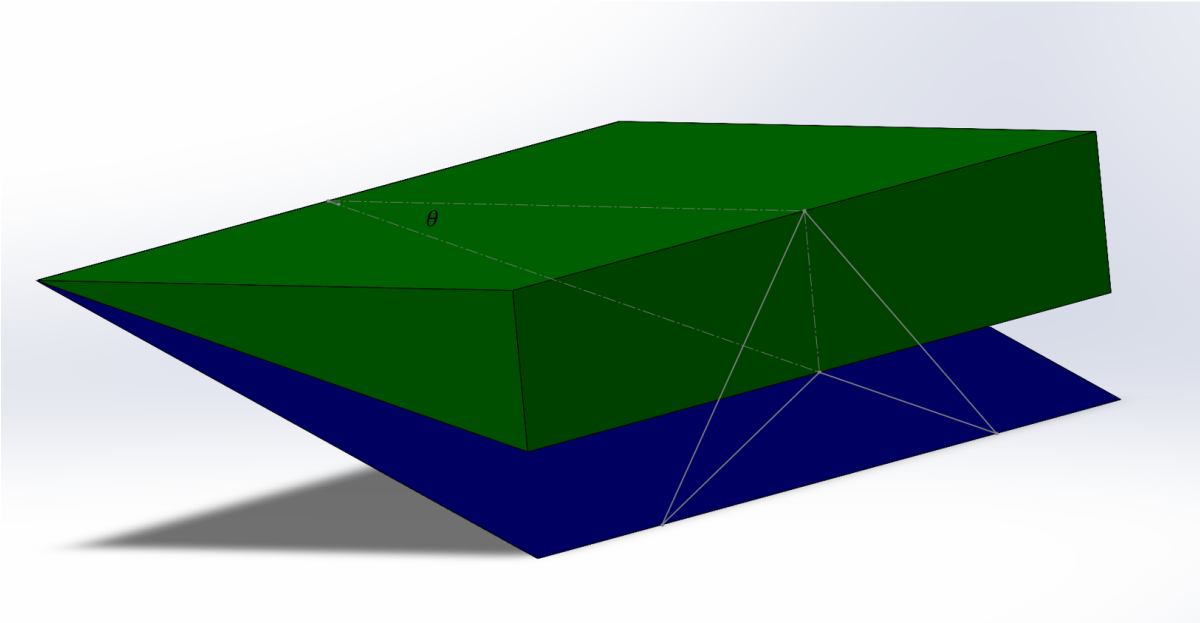

Figure 2.3. Rear profile.

Figure 2.3 shows the rear profile staring to form. The arbitrary surface which extends from the top of the wedge to the bottom of the shock is traced out from the rear and will be cut out to form the profile in the next step.

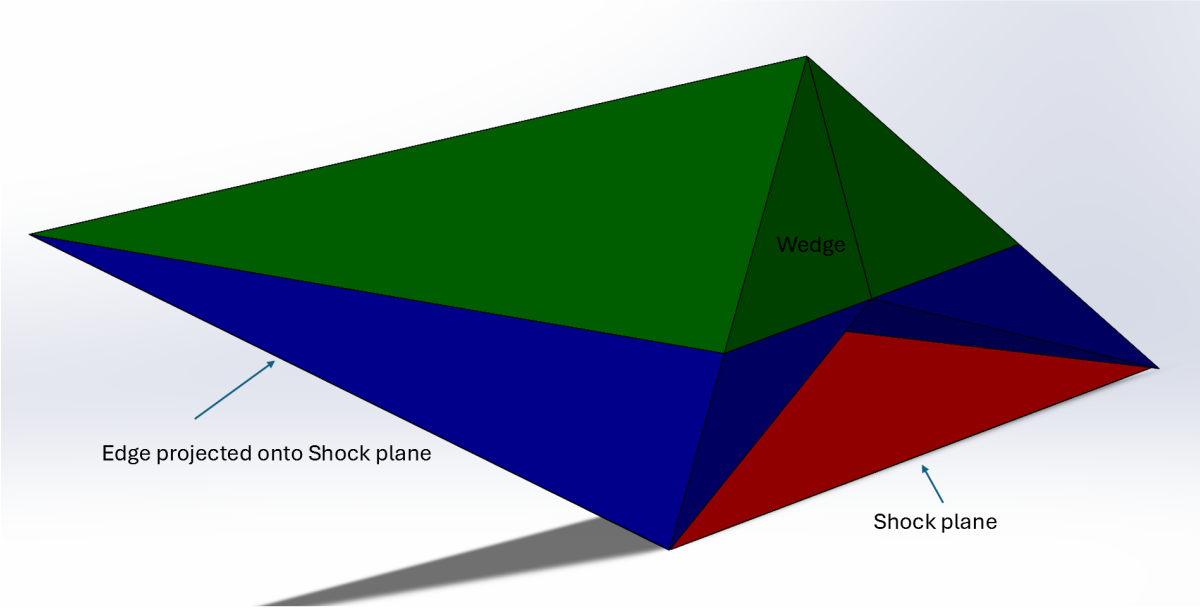

Figure 2.4. Caret waverider shape.

Figure 17 shows the side profile of the caret wing that extends down to the oblique shock. Notice that the center of the caret wing is the original 2D wedge profile with angle θ. The green surface is the part of the original inflinately long 3D wedge geometry. The surfaces in blue are the flow field extended down into the shock plane, shown in red.

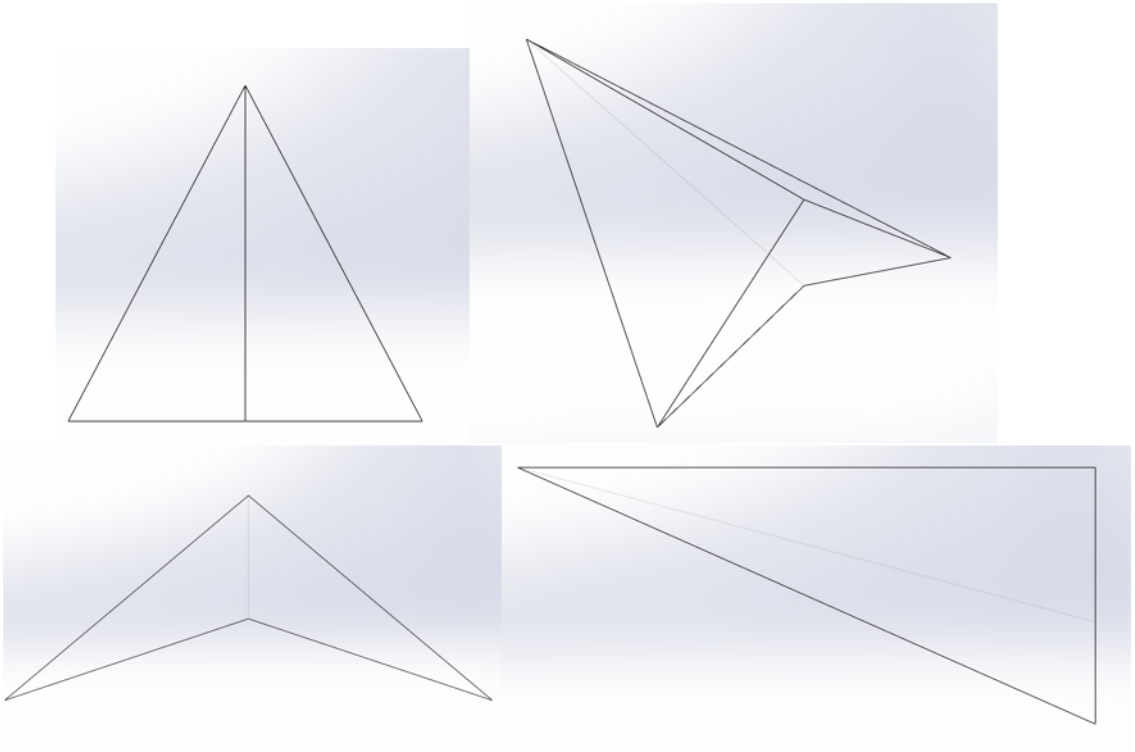

Figure 2.5. Multiview orthographic projection of caret wing waverider.

Figure 2.5 shows the final caret wing wave rider geometry. Notice that the top, wings, and nose have a sharp leading edge. If this geometry was built and flown, the sharp nose and leading edges would melt at hypersonic speeds due to the intense heat generated from the air friction as our current understanding of material science has not produced anything that can withstand such a high temperature concentrated in such a tiny volume.

2.2 Conical Wave Riders

The next development in wave rider design came from in 1963 from Jones (23). The 2D oblique shock flow field was extended into an axisymmetric 3D flow field using cones. This method is similar Nonweiler's of solving the flow field of a wedge. but instead of an arbitrary wedge, a cone shape is selected, and the flow field that is generated by the cone and it's oblique shock is found using the Taylor Maccoll equation below (23).

$$\frac{(\gamma-1)}{2}\left[V_{max}^2 - V_r^2 - \left(\frac{dV_r}{d\theta}^2\right)\right]\left[2V_r + \frac{dV_r}{d\theta}\cot(\theta) + \frac{d^2V_r}{d\theta^2}\right] - \frac{dV_r}{d\theta}\left[V_r\frac{dV_r}{d\theta} + \frac{dV_r}{d\theta}\left(\frac{d^2V_r}{d\theta^2}\right)\right] = 0 \tag{2.5}$$

The Taylor-Maccoll equation gives a solution for conical flow fields. It is an ordinary differential equation with the dependent variable V_r. V_R is a function of θ with

$$V_\theta = \frac{dV_r}{d\theta} \tag{2.6}$$

The solution to the Taylor-Maccoll equation must be solved numerically as no analytical solution has been found (23). Typically, the velocity V is non-dimensionalized as

$$V' \equiv \frac{dV_r}{d\theta} \tag{2.7}$$

to simplify solving the numerical solution. Then equation 2.5 becomes

$$\frac{\gamma-1}{2}\left[1 - (V_r')^2 - \left(\frac{dV_r'}{d\theta}^2\right)\right]\left[2V_r' + \frac{dV_r'}{d\theta}\cot(\theta) + \left(\frac{d^2V_r'}{d\theta^2}\right)\right] - \frac{dV_r'}{d\theta}\left[V_r'\frac{dV_r'}{d\theta} + \frac{dV_r'}{d\theta}\left(\frac{d^2V_r'}{d\theta^2}\right)\right] = 0 \tag{2.8}$$

with the non dimensional V' expressed as a function of the mach number

$$\frac{V}{V_{max}} \equiv V' = \left[\frac{2}{\gamma-1}M^2 + 1\right]^{\frac{-1}{2}} \tag{2.9}$$

Where $V' = f(M)$, given M, V' can be found (23).

2.2.1. Numerical Solution to the Taylor-Maccoll Equation

The steps to numerically solve the Taylor-Maccoll Equation taken from (23) are as follows

1. First assume a shock wave angle θ_s and a free stream Mach number M_∞. From this, the Mach number and flow deflection angle, M_2 and δ, immediately behind the shock can be found from the oblique shock relations. Note that, unlike equation 2.1, the flow deflection angle is here denoted by δ so as not to confuse it with the polar coordinate θ.

2. From M_∞ and δ, the radial and normal components of flow velocity, V_r' and V_θ', directly behind the shock can be found from the geometry of Figure 2.6. Note thatV' is obtained by inserting M_2 into Equation (10.16).

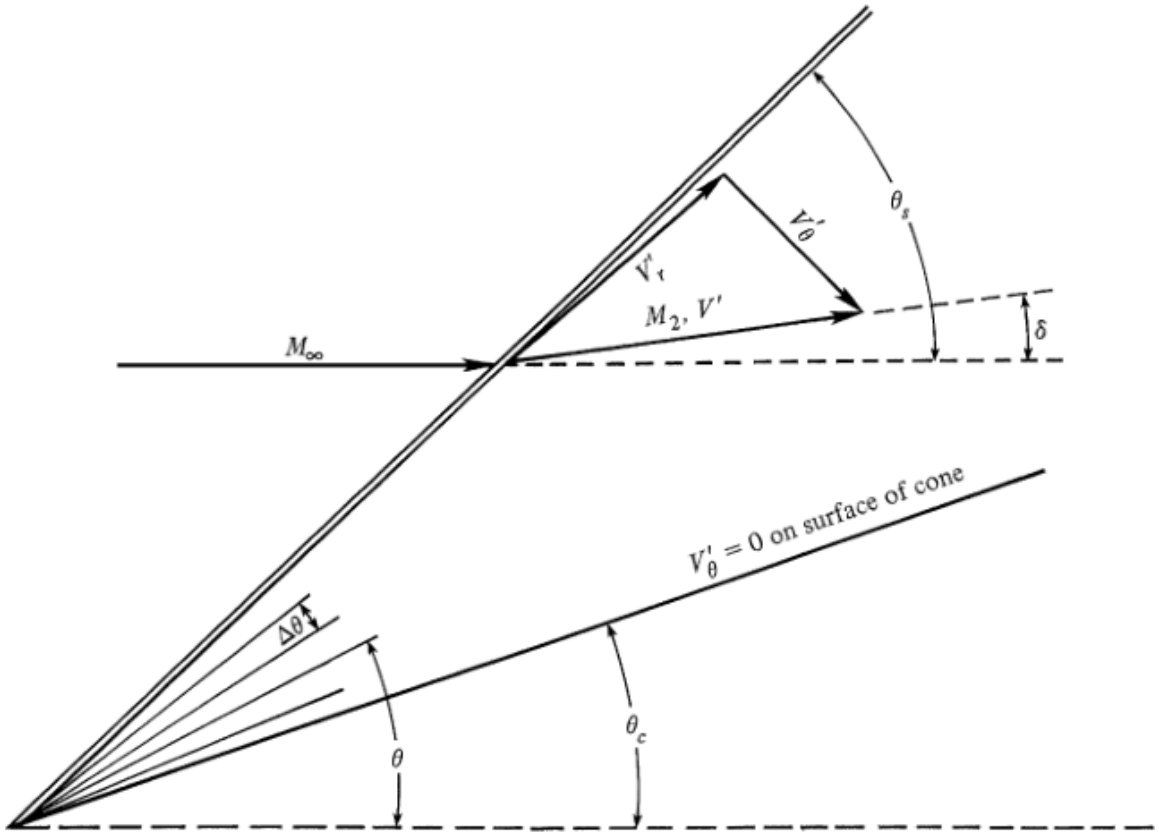

Figure 2.6. Geometry for the numerical solution of flow over a cone (23).

3. Using the above value of V_r' directly behind the shock as a boundary value, solve Equation 2.9 for V_r' numerically in steps of θ, marching away from the shock. Here, the flow field is divided into incremental angles $\Delta\theta$, as sketched in Figure 2.6. The ordinary differential equation 2.8 can be solved at each $\Delta\theta$ using any standard numerical solution technique, such as the Runge-Kutta method.

4. At each increment in θ, the value of V_θ' is calculated from Equation 2.6. At some value of θ, namely $\theta = \theta_c$, we will find $V_\theta' = 0$. The normal component of velocity at an impermeable surface is zero. Hence, when $V_\theta' = 0$ at $\theta = \theta_c$ then θ_c must represent the surface of the particular cone that supports the shock wave of given wave angle θ_s at the given Mach number M_∞ as assumed in step 1. That is, the cone angle compatible with M_∞ and θ_s is θ_c. The value of V_r' at θ_c gives the Mach number along the cone surface via Equation 2.9.

5. In the process of steps 1 through 4 here, the complete velocity flow field between the shock and the body has been obtained. Note that, at each point (or ray), $V' = \sqrt{(V_r')^2 + (V'\theta)^2}$ and M follow from Equation 2.9. The pressure, density, and temperature along each ray can then be obtained from the isentropic relations

H

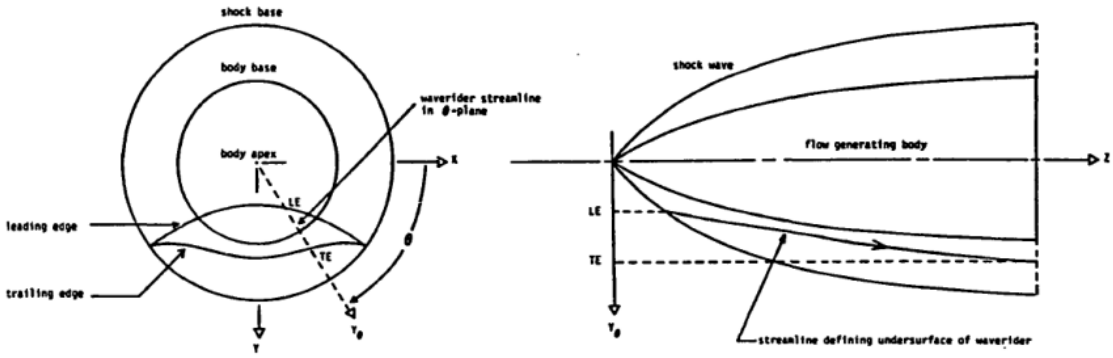

Figure 2.7. Streamline tracing axes geometry (24).

$$\frac{P_0}{P} = \left(1 + \frac{\gamma - 1}{2} M^2\right)^{\frac{\gamma}{\gamma - 1}} \tag{2.10}$$

$$\frac{\rho_0}{\rho} = \left(1 + \frac{\gamma - 1}{2} M^2\right)^{\frac{\gamma - 1}{\gamma -}} \tag{2.11}$$

$$\frac{T_0}{T} = \left(1 + \frac{\gamma - 1}{2} M^2\right) \tag{2.12}$$

If a different value of M_∞ and/or θ_s is assumed in step 1, a different flow field and cone angle θ_c will be obtained from steps 1 through 5. By a repeated series of these calculations, tables or graphs of supersonic cone properties can be generated.

2.2.2. Bottom Surface Streamline tracing

After solving the flowfield using the Taylor-Maccoll equations, the lower surface can be found by solving the streamfunction using the steps outlined below (24):

1. The values of the density ρ, and the z component of velocity, denoted by w are discretized in the axial and radial directions. Axis directions are shown in figure 2.7.

2. FIt a cubic spline for as a prduct of the density and z component of velocity, ρw, such that

$$\rho w(y_j, z) = a_j + b(y - y_j) + c_j(y - y_j)^2 + d_j(y - y_j)^3 \tag{2.13}$$

for each (n-1) intervals of the n grip points discretiozed along the z direction. a_j, b_j, c_j, d_j are all constant coefficients and y is the coordinates in the vertical direrction such that

$$y_j \leq y \leq y_{j+1} \tag{2.14}$$

with j being a grid point on the index.

3. Calculate the mass flow $\dot{m}$ between grid points as

$$\dot{m} = \int_{y_j}^{y_{j+1}} (\rho w_j) dy \tag{2.15}$$

Subsiting equation 2.13 into equation 2.15, the mass flow per unit width becomes

$$\dot{m} = a_j \Delta y + \frac{1}{2} b_j \Delta y^2 + \frac{1}{3} c_j \Delta y^3 + \frac{1}{4} d_j \Delta y^4 \tag{2.16}$$

with

$$\Delta y = y_{j+1} - y_j \tag{2.17}$$

4. In terms of the streamfunction, the mass per unit width can be written as

$$\dot{m} = \psi_{j+1} - \psi_j \tag{2.18}$$

The mass flow between each pair of grid points was found in step 3. Therefore the streamfunction at $j+1$ can be found using equation 2.18 assuming the value of the streamfunction is known at point j. By arbitrarily setting the value of the streamfunction to zero at the surface of the body, the discretized values of the streamfunction along z can be found.

5. Fit a cubic spline to the y variation of the streamfunction at each z location. The y coordinate of a given streamline is calculated at each grid point. The streamline can then be traced through the flow field.

The top surface of the waverider is generated by following the freestream from the leading edge to the rear. The pressure on the upper surface is simply the freestream pressure, $p\infty$.

In the 1980s, this method was expanded upon using right circular cones and elliptic cones to develop flow fields utilizing hypersonic small disturbance theory and calculus of variations (1).

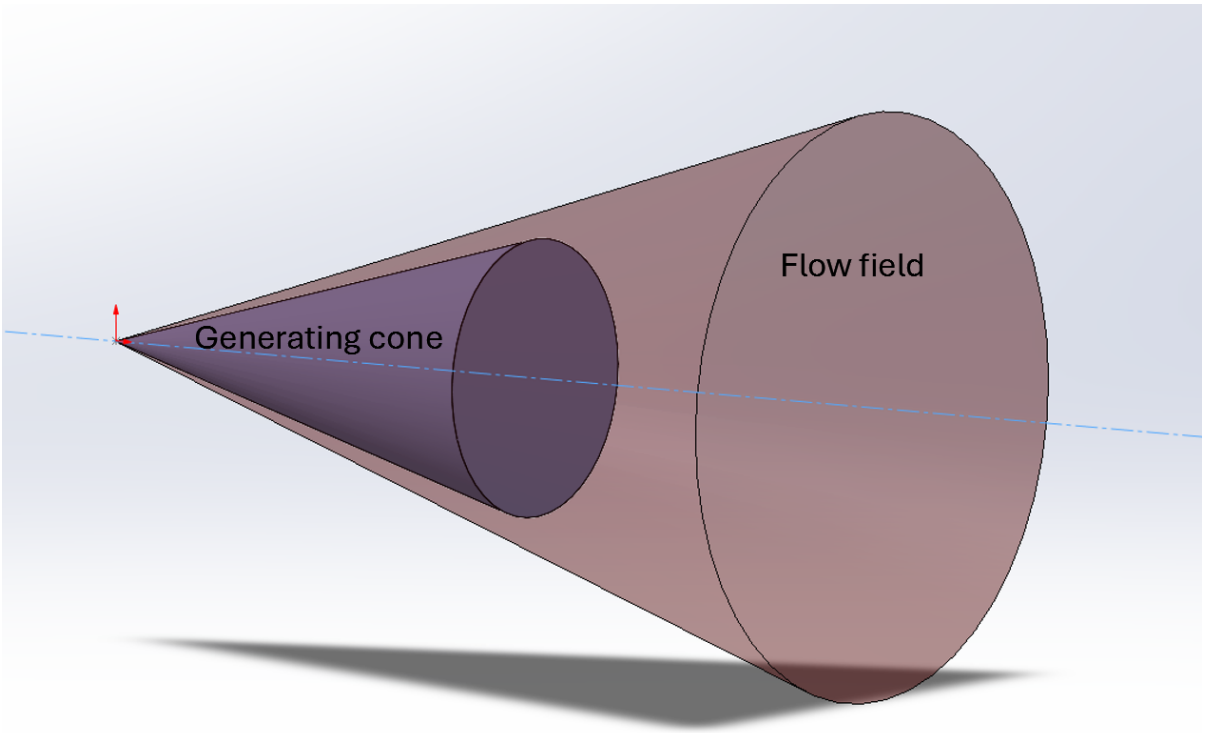

Figure 2.8. Solution to conical flow field.

Figure 2.8 show the flow field generated by an arbitrary cone shape. The flow field was solved using the Taylor-Mccoll equation.

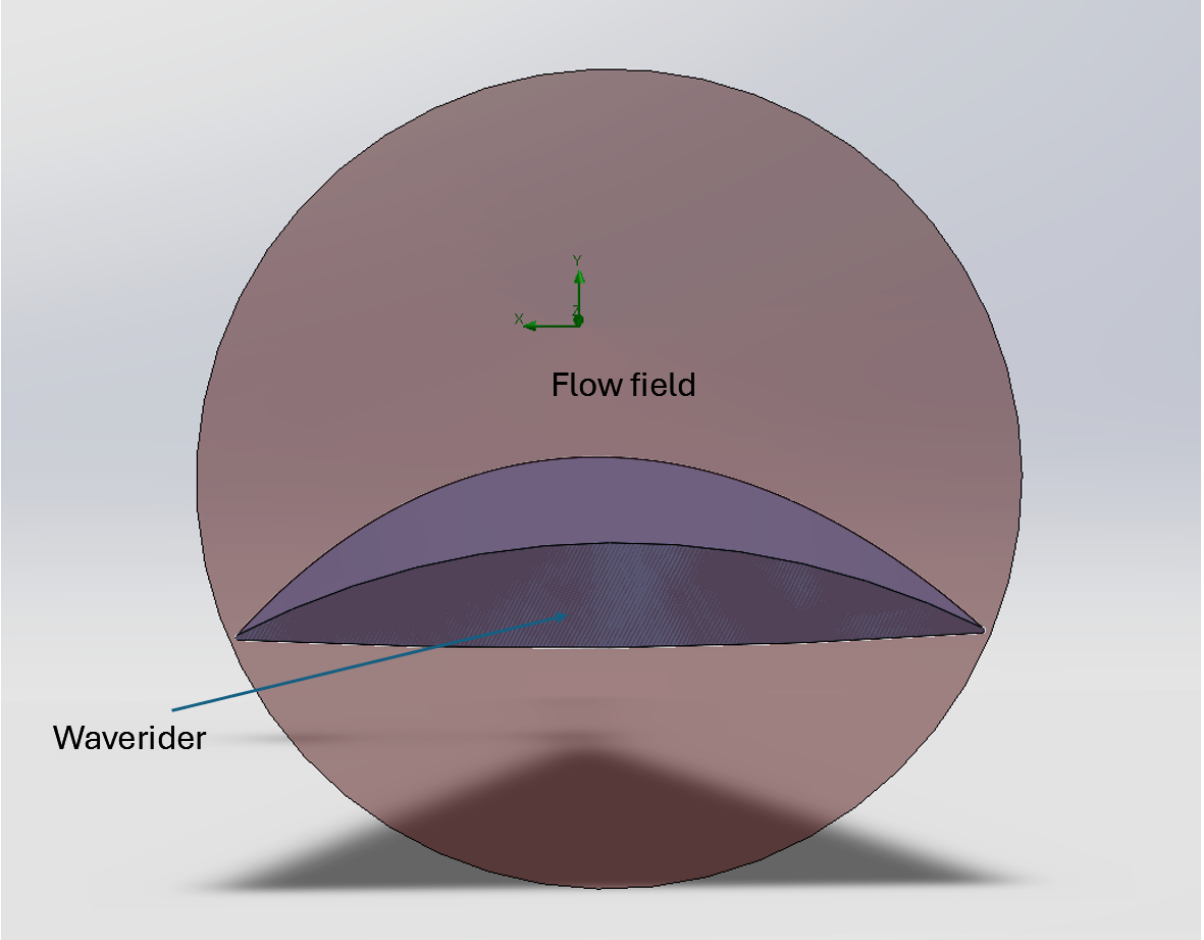

Figure 2.9. Conical waverider being carved out of the inviscid flow field.

Then the waverider shape can be generated by carving out the lower surface by following the streamlines of the flow field.The upper surface follows the freestream flow. Note that the edges of the conical waverider lie on the edge of the generated shock. This ensures that the shock is attached along the leading edge of the conical waverider.

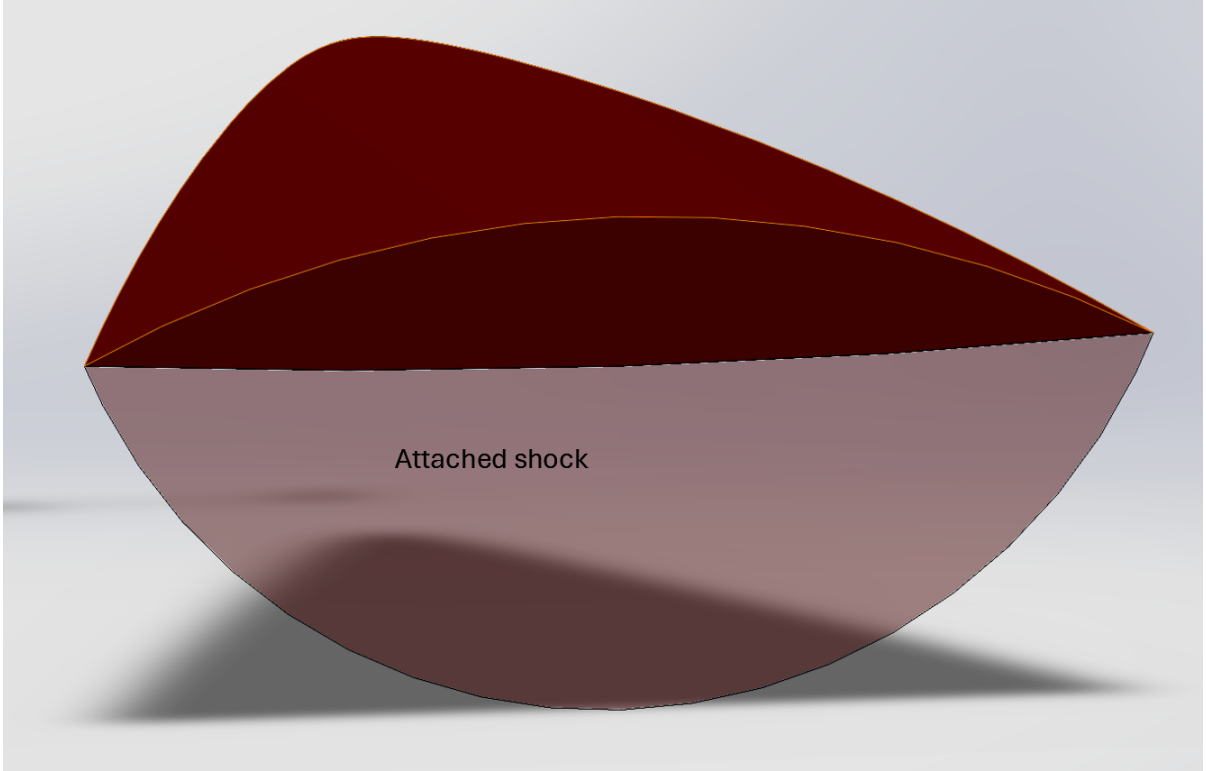

Figure 2.10. Conical waverider with attached shock.

Figure 2.10 shows the resulting conical waverider geometry with the attached shock all along the leading edge to the rear of the waverider. This provides a high pressure region for the waverider to ”ride” on. The attached shock ensures no spillage of the high pressure region from the bottom to the top. This is what increases the efficiency of the waverider and allows it to obtain high values of the lift to drag ratio.

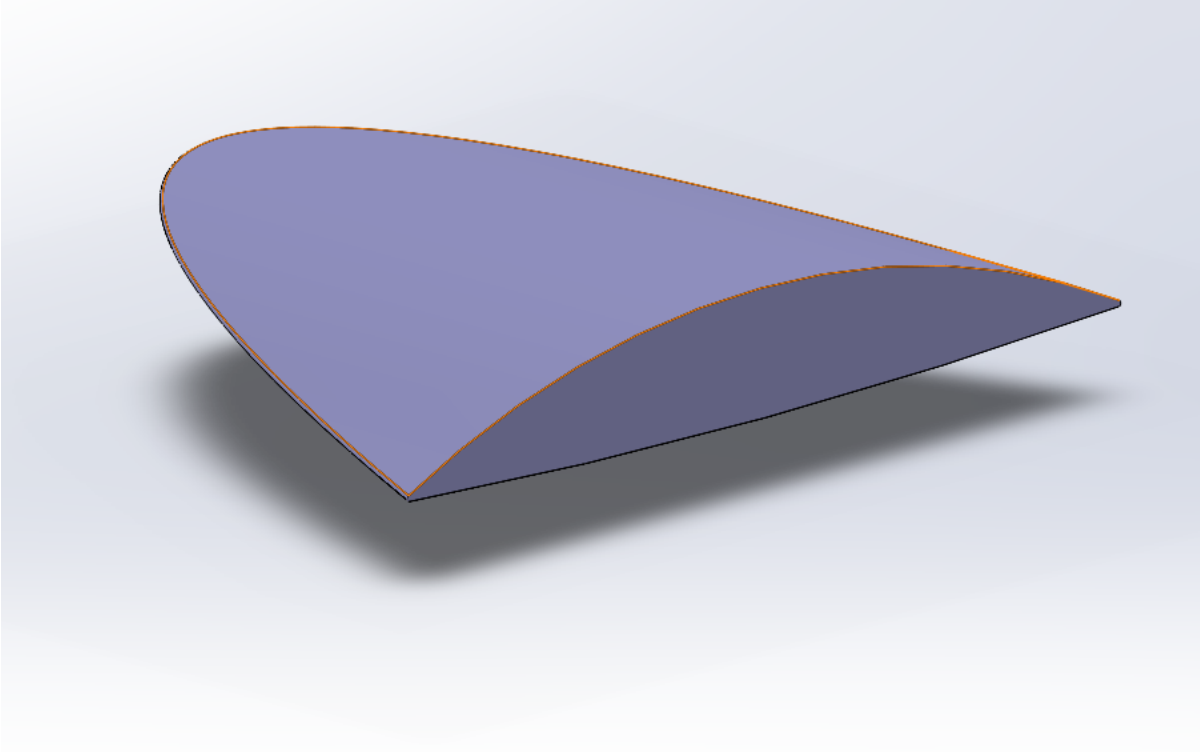

Figure 2.11. Final conical waverider shape.

2.3 Viscous Optimized Waveriders

The caret wing and conical flow waveriders previously described are designed using inviscid flow theory. Skin friction and boundary layer interaction are not factored in to the predicted lift to drag ratio. Only the effects of wave drag are included, resulting in exaggerated lift to drag values.

Starting in 1987, John Anderson and his students at the University of Maryland began to develop methods for including the skin friction effects into the design of hypersonic waveriders, optimizing the waverider geometry for Mach number as well as viscous effects; creating a new class of waveriders known as viscous optimized waveriders. The approach to designing viscous optimized waveriders relies on using numerical optimization based on the simplex method. The steps taken to design a viscous optimized waverider are as follows from (23):

1. The lower (compression) surface was generated by a stream surface behind a conical shock wave. The inviscid conical flow field was obtained from the numerical solution of the Taylor-Maccoll equation, discussed in 2.2.1.

2. The upper surface was treated as an expansion surface, generated in a manner similar to that for the inviscid flow about a tapered, axisymmetric cylinder at zero angle of attack, and calculated by means of the axisymmetric method of characteristics.

3. The viscous effects were calculated by means of either a reference temperature method or an integral boundary-layer analysis following surface streamlines, including transition from laminar to turbulent flow.

4. Blunt leading edges were included to the extent of determining the maximum leading-edge radius required to yield acceptable leading-edge surface temperatures, and then the leading-edge drag was estimated by modified newtonian theory.

5. The final waverider configuration, optimized for maximum L/D at a given Mach number and Reynolds number with body fineness ratio as a constraint, was obtained from the numerical simplex method taking into account all of the effects itemized in steps 1–4 within the optimization process itself.

2.3.1. Calculation of Viscous effects

Two separate methods can be used to calculate the viscous effects of early viscous optimized waveriders. The Integral Boundary layer method of Walz (25) or the Reference Temperature method of Eckert (26).

2.3.2. Integral Boundary Layer Method

The first method to predict the laminar-viscous interaction of the boundary layer is known as Walz's integral method (25). Walz's method requires a solution of a set of coupled first-order ordinary differential equations given by the boundary layer momentum and mechanical energy (27) (28).

$$Momentum : Z' + \frac{u'_e}{u_e} F_1 Z - F_2 = 0 \tag{2.19}$$

$$Mechanical\ Energy : W' + \frac{u'_e}{u_e} F_3 W - \frac{F_4}{Z} = 0 \tag{2.20}$$

$$Z = \delta_2 \left(\frac{\rho_e u_e \delta_2}{\mu_w} \right) \tag{2.21}$$

$$W = \delta_3 / \delta_2 \tag{2.22}$$

Boundary layer thicknesses δ being

$$Displacement\ :\ \delta_1 \equiv \int_0^\delta \left(1 - \frac{\rho u}{\rho_e u_e} \right) dy \tag{2.23}$$

$$Momentum\ :\ \delta_2 \equiv \int_0^\delta \frac{\rho u}{\rho_e u_e} \left(1 - \frac{u}{u_e} \right) dy \tag{2.24}$$

$$Energy\ :\ \delta_3 \equiv \int_0^\delta \frac{\rho u}{\rho_e u_e} \left(1 - \frac{u^2}{u_e^2} \right) dy \tag{2.25}$$

$$F_1 = 3 + 2H - M_e^2 + n\frac{\mu_w'/\mu_w}{u'/u_e}, \quad n = \begin{cases} 0, & T_w = \text{constant} \\ 1, & T_w \neq \text{constant} \end{cases} \tag{2.26}$$

$$F_2 = \frac{2a}{b} \tag{2.27}$$

$$F_3 = 1 + H + r(\gamma - 1)M_e^2\left(1 - \frac{\tilde{\theta}}{W}\right) \tag{2.28}$$

$$F_4 = \frac{(2\beta - aW)}{b} \tag{2.29}$$

In the above equations, prime represents differentiation with respect to x, the boundary layer coordinate in the streamline direction. The variables in equations 2.26-2.29 are defined as

$$H = \frac{\delta_1}{\delta_2} = bH_{12} + r\frac{\gamma - 1}{2}M_e^2(\bar{W} - \tilde{\theta}) \tag{2.30}$$

$$a = 1.7261(W^* - 1.515)^{0.7158} \tag{2.31}$$

$$b = \frac{(\delta_2)_u}{\delta_2} = 1 + r\frac{\gamma - 1}{2}M_e^2(\bar{W} - \tilde{\theta})(2 - W) \tag{2.32}$$

$$r = \sqrt{Pr} \tag{2.33}$$

$$\tilde{\theta} = \frac{T_{aw}(x) - T_w(x)}{T_{aw}(x) - T_e(x)} \tag{2.34}$$

$$\beta = \beta_u \chi \tag{2.35}$$

$$H_{12} = 4.0306 - 4.2845\,(W^* - 1.515)^{0.3886} \tag{2.36}$$

$$T_{aw} = T_e + \frac{ru_e^2}{2c_p} \tag{2.37}$$

$$W^* = \frac{(\delta_3)_u/(\delta_2)_u}{W/\psi} \tag{2.38}$$

$$\psi = 1 + \frac{(\psi_{12} - 1)M_e}{M_e + \frac{\psi_{12} - 1}{\psi_0}} \tag{2.39}$$

$$\psi_{12} = \frac{2-(\delta_1)_u/\delta}{W^*\tilde{\theta}} + \frac{1-(\delta_1)_u/\delta}{W^* g}(1-\tilde{\theta}) \tag{2.40}$$

$$\psi_0' = 0.0144(2-W^*)(2-\theta)^{0.8} \tag{2.41}$$

$$(\delta_1)_u/\delta = 0.420 - (W^* - 1.515)^{0.424} W^* \tag{2.42}$$

$$g = 0.324 + 0.336(W^* - 1.515)^{0.555} \tag{2.43}$$

$$\beta_u = 0.1564 + 2.1921(W^* - 1.515)^{1.70} \tag{2.44}$$

$$\chi = \frac{[1 + r(\frac{\gamma-1}{2})M_e^2[1.16W^* - 1.072 - \tilde{\theta}(2W^* - 2.581)]]^{0.7}}{[1 + r(\frac{\gamma-1}{2})M_e^2(1-\tilde{\theta})]^{0.7}} \tag{2.45}$$

Finally, the local skin friction coefficient of the laminar flow can be calculated from (27)

$$C_f(x) = \frac{\tau_w}{\frac{1}{2}\rho_e u_e^2} = 2\frac{a}{b}\left(\frac{\mu_w}{\rho_e u_e \delta_2}\right) = 2\frac{a}{b}\left(\frac{\mu}{\rho_e u_e w}\right)^{1/2} \tag{2.46}$$

After the boundary layer transition, the viscous interaction of the turbulent boundary layer is calculated using the method of White and Christoph (29). This method requires the solution of one of two first-order differential equations along the boundary layer edge streamlines, which depend on the parameter $\frac{\lambda}{\lambda_{max}}$ (27) (28) where

$$\lambda = \sqrt{\frac{2}{C_f}} \tag{2.47}$$

$$\lambda_{max} = 8.75 log_{10} Re^* \tag{2.48}$$

$$S = \frac{\left(\frac{T_{aw}}{T_e}\right)^{1/2}}{sin^{-1}A + sin^{-1}B} \tag{2.49}$$

$$Re^* = \frac{-\rho_e}{\mu_w}\left(\frac{T_e}{T_w}\right)^{1/2}\frac{u_e^2}{u_e'} \tag{2.50}$$

with the parameters A,B in equation 2.49 defined as

$$A = a/c \tag{2.51}$$

$$B = b/c \tag{2.52}$$

with

$$a = \frac{T_{aw} + T_w}{T_e} - 2 \tag{2.53}$$

$$b = \frac{T_{aw} + T_w}{T_e} \tag{2.54}$$

$$c = \left[\left(\frac{T_{aw} + T_w}{T_e} \right)^2 - 4\frac{T_w}{T_e} \right]^{1/2} \tag{2.55}$$

T_{aw} is given by equation equation 3.52 with the recovery factor being the turbulent value

$$r = Pr^{1/3} \tag{2.56}$$

From (29), if $\frac{\lambda}{\lambda_{max}} < 0.36$ or $Re^* < 0$ then

$$\lambda' = \frac{1}{8}\frac{\rho_e}{\rho_w}\left(\frac{T_e}{T_w}\right)^{1/2} u_e exp\left(-0.48\frac{\lambda}{S}\right) - 5.5\frac{u'_e}{U_e} \tag{2.57}$$

If $\frac{\lambda}{\lambda_{max}} > 0.36$, then

$$\lambda' = \frac{\frac{-u'_e}{u_e}(1 + 9S^{-2}g^* Re^{*0.07})}{0.16 f^* S^3} + \frac{[\frac{u_e U''_e - 2(U'_e)^2}{uu'}](3S^2 * Re^{*0.07})}{0.16 f^* S^3} \tag{2.58}$$

with

$$f^* = (2.434z + 1.443z^2)exp(-44z^6) \tag{2.59}$$

$$g^* = 1 - 2.3z + 1.76z^3 \tag{2.60}$$

$$z = 1 - \frac{\lambda}{\lambda_{max}} \tag{2.61}$$

as in the laminar case, the prime denotes differentiation with respect to the streamline coordinate x (27).

$$C_f(x) = \frac{0.455}{S^2 \ln^2\left(\frac{0.06}{S}\mathrm{Re}_x \frac{\mu_e}{\mu_w}\sqrt{\frac{T_e}{T_w}}\right)} \tag{2.62}$$

The local turbulent skin friction is calculated with equation 2.62

The transition from laminar to turbulent flow is based on experimental data from sharp cones at zero angle of attack (30) and wings with blunt swept edges (27).

$$\log_{10}(\mathrm{Re}_{x_t}) = 6.421 \exp\left(1.209 \times 10^{-4} M_e^{22.641}\right) \tag{2.63}$$

Equation 2.63 gives the Reynolds number for the local transition Re_{x_t} as a function of the Mach number at the local edge M_e (30).

This is then modified for leading edge sweep, giving

$$\frac{(Re\,x_t)_\Lambda}{(Re\,x_t)_{\Lambda=0}} = 0.787 \cos^{4.346}\Lambda - 0.7221 e^{-0.0991\Lambda} + 0.9464 \tag{2.64}$$

Λ is the angle of sweep of the leading edge of the wing, with $(Re\,x_t)_{\Lambda=0}$ taken from equation 2.63. The end of the transition region is then predicted using a relation ship developed by Harris and Blanchard (31), giving the following.

$$x_{te} = x_{ti}\left[1 + 5(\mathrm{Re}_x)_{ti}^{-0.2}\right] \tag{2.65}$$

x_{te}, x_{ti} are the distances along the streamline from the leading edge to the beginning and end of transition. $(\mathrm{Re}_x)_{ti}$ is the local Reynolds number from equation 2.64.

In the transition region, the skin friction coefficient $C_{f_{TR}}$, is assumed to be a linear combination of the laminar C_{f_L} and turbulent C_{f_T} values.

$$C_{f_{TR}}(x) = (1-\xi)C_{f_L} + \xi C_{f_T} \tag{2.66}$$

Where ξ is a weighting factor (27)

$$\xi(x) = 1 - e^{-3[exp\frac{ln2}{5x_{ti}}(Re_x)_{ti}^{0.2}(x-x_{ti})]-1]^2} \tag{2.67}$$

2.3.3. Reference Temperature Method

The reference temperature method of Eckert (26) is another method used to predict the skin friction distribution along the streamlines that form the waverider. It uses a flat plate assumption at each discretized point for laminar and turbulent flow with an estimate for the boundary layer transition point. This method is much simpler than the integral boundary layer method and the results were found to be within 10% of each other (24).

For a flat plate in laminar flow, the local skin friction coefficient is given as equation 2.68 below

$$C_f = 0.664 \frac{1}{\sqrt{Re_x}} \frac{T'^{(\omega-1)/2}}{T_\infty} \tag{2.68}$$

with the local Reynolds number defined as

$$Re_x = \frac{\rho_\infty V_\infty x}{\mu_\infty} \tag{2.69}$$

T' is the reference temperature and is defined as

$$\left(\frac{T'}{T_\infty}\right) = 1 + 0.032M_\infty^2 + 0.58\left(\frac{T_w}{T_\infty} - 1\right) \tag{2.70}$$

ω in equation 2.68 is the exponent of an assumed exponential variation of μ with

$$\left(\frac{\mu'}{\mu_\infty}\right) = \left(\frac{T'}{T_\infty}\right)^\omega \tag{2.71}$$

For a flat plate in turbulent flow, the local skin friction coefficient is given as equation 2.68 below

$$C_f = \frac{0.0592}{(Re'_x)^{0.2}} \tag{2.72}$$

with

$$Re'_x = \frac{\rho'_\infty V_\infty x}{\mu'_\infty} \tag{2.73}$$

with ρ', μ' calculated at the reference temperature.

The boundary layer transition is predicted using experimental data for transition on sharp cones at zero angle of attack, from the work of DiCristina (30), giving the empirical correlation as follows

$$log_{10}Re_{x_t} = 6.421e^{(1.209x10^{-4}M_e^{2.641})} \tag{2.74}$$

2.4 Lift, Drag and Moment Calculations

The lift drag and moment coefficients are calculated by integrating the pressure and shear stresses on the surface of the waverider. The base drag is typically not included in the analysis, as it can be assumed to be negligible compared to the drag of the main body at hypersonic speeds(24) (28).

2.4.1. Inviscid Lift Drag and Moment Coefficients

The inviscid lift L_p is calculated by integrating over the projected planform of the waverider surface in the equation below given in Cartesian coordinates (24). $p(x,z)$ is the pressure distribution, l is the length, $f(z)$ is the function of the waverider planform in the (x,z) plane. 0 denotes the origin beginning at the tip of the nose, and the integration is done over half the symmetric waverider and multiplied by 2 (24).

$$L_p = 2\int_0^l \int_0^{x=f(z)} p(x,z)\,dx\,dz \tag{2.75}$$

The inviscid drag D_p can be estimated if needed by integrating over the base area of the waverider in polar coordinates in Equation 2.76 below. $g(\theta)$ is the function that defines the base of the waverider in the $((x,y)$ plane, and 0 denotes the origin from the centerline.

$$D_p = 2\int_0^{\pi/2}\int_0^{r=g(\theta)} [p(r,\theta) - p_\infty]\, r\, dr\, d\theta \tag{2.76}$$

The inviscid pitching moment M_p has two components, the pitching moment about the nose $M_{p,plan}$ due to the pressure distribution over the planform, and the pitching moment due to the pressure distribution over the base $M_{p,base}$.

$$M_{p,\text{plan}} = 2\int_0^1 \int_0^{x=f(z)} p(x,z)\, z\, dx\, dz \tag{2.77}$$

$$M_{p,\text{base}} = 2\int_0^{\pi/2}\int_0^{r=g(\theta)} p(r,\theta)\, r^2\, dr\, d\theta \tag{2.78}$$

The total pitching moment is being

$$M_p = M_{p,\text{plan}} + M_{p,\text{base}} \tag{2.79}$$

The integrations of Equations 2.75 - 2.78 are done numerically with the composite trapezoidal rule shown in Equation 2.80 below with an arbitrary function, f of two variables x and y (24).

$$\begin{aligned}\int_a^b \int_{c(x)}^{d(x)} f(x,y)dydx = \left[\frac{b-a}{4}\right] [(d[a]-c[a])\ \ (f[a,c(a)] \\ +f[a,d(a)]) + (d[b]-c[b])\ \ (f[b,c(b)] + f[b,d(b)])]\end{aligned} \tag{2.80}$$

2.4.2. Viscous Lift Drag and Moment Coefficients

The calculation of lift, drag, and moment due to skin friction is conceptually similar to that for aerodynamic forces caused by pressure distribution. Shear stress values are known along streamlines that describe the upper and lower surfaces of the waverider.

The surface is divided into triangular panels whose vertices are data points along these streamlines. The average shear stress over a panel is calculated by averaging the shear stress at its three corners:

$$\tau_{\text{avg}} = \frac{1}{3}(\tau_1 + \tau_2 + \tau_3) \tag{2.81}$$

The viscous force on a panel is then:

$$F_{\text{panel}} = \tau_{\text{avg}} A_{\text{panel}} \tag{2.82}$$

where A_{panel} is the area of the triangular panel, calculated by:

$$A_{\text{panel}} = \sqrt{s(s-a)(s-b)(s-c)} \tag{2.83}$$

$$s = \frac{1}{2}(a+b+c) \tag{2.84}$$

with a, b, c being the side lengths of the triangle.
The viscous force on each panel is split into lift and drag components:

$$L_{t,\text{panel}} = F_{\text{panel}} \cos(\theta_{yt}) \tan(\theta_v) \tag{2.85}$$

$$D_{t,\text{panel}} = F_{\text{panel}} \cos(\theta_{yt}) \cos(\theta_{xz}) \tag{2.86}$$

where angles θ_{yt} and θ_{xz} relate to the orientation of the panel relative to the coordinate axes. The force acts at the shear-stress weighted centroid of the panel. The coordinates of the centroid (y_c, z_c) are:

$$y_c = \frac{y_1\tau_1 + y_2\tau_2 + y_3\tau_3}{\tau_1 + \tau_2 + \tau_3} \tag{2.87}$$

$$z_c = \frac{z_1\tau_1 + z_2\tau_2 + z_3\tau_3}{\tau_1 + \tau_2 + \tau_3} \tag{2.88}$$

The contribution to the pitching moment about the leading edge from a panel is:

$$M_{\text{panel}} = y_c F_{\text{panel},x} + z_c F_{\text{panel},z} \tag{2.89}$$

The total lift, total drag, and total pitching moment due to skin friction are obtained by summing the contributions over all panels:

$$L = \sum_{i=1}^{N} L_{t,i} \tag{2.90}$$

$$D = \sum_{i=1}^{N} D_{t,i} \tag{2.91}$$

$$M = \sum_{i=1}^{N} M_{t,i} \tag{2.92}$$

where N is the total number of panels.

The total aerodynamic forces and moments on the waverider are calculated by summing the contributions from both inviscid (pressure) and viscous (shear stress) sources. The total lift L, drag D, and pitching moment M about the leading edge are defined by the following equations:

$$L = L_P + L_T \tag{2.93}$$

$$D = D_P + D_T \tag{2.94}$$

$$M = M_P + M_T \tag{2.95}$$

Here, L_P, D_P, and M_P represent the inviscid (pressure) contributions, while L_T, D_T, and M_T represent the viscous (shear stress) contributions.

Aerodynamic coefficients are then defined for these total quantities. The lift coefficient C_L, drag coefficient C_D, and moment coefficient C_M are given by:

$$C_L = \frac{L}{q_\infty S} \tag{2.96}$$

$$C_D = \frac{D}{q_\infty S} \tag{2.97}$$

$$C_M = \frac{M}{q_\infty S l} \tag{2.98}$$

In these expressions, S is the waverider's planform area, l is the waverider centerline length, and q_∞ is the freestream dynamic pressure defined as:

$$q_\infty = \frac{1}{2}\rho_\infty V_\infty^2 \tag{2.99}$$

Finally, the lift-to-drag ratio is simply defined as the ratio of the lift coefficient to the drag coefficient:

$$\frac{L}{D} = \frac{C_L}{C_D} \tag{2.100}$$

This framework allows the total aerodynamic performance of the waverider, including the combined effects of pressure and shear forces, to be properly evaluated.

2.5 Optimization

The construction and aerodynamic analysis of a single waverider configuration involves steps labeled A through F as shown on Figure 2.12 using a numerical routine.

The optimization is performed by adjusting the shape of the waverider's leading edge curve until an optimum configuration is found that maximizes the lift-to-drag ratio or minimizes total drag.

The Simplex Method, developed by Nelder and Mead, is used for the numerical optimization (24). It is a zero-order method, meaning it relies only on function evaluations, without requiring derivative information. Each function evaluation corresponds to calculating a figure of merit (such as L/D or C_D) for a given waverider shape.

The simplex method minimizes a function of n variables by comparing function values at $n+1$ vertices. The vertex with the highest function value is replaced by a new point through operations such as reflection, expansion, or contraction, moving the simplex toward the minimum of the function surface.

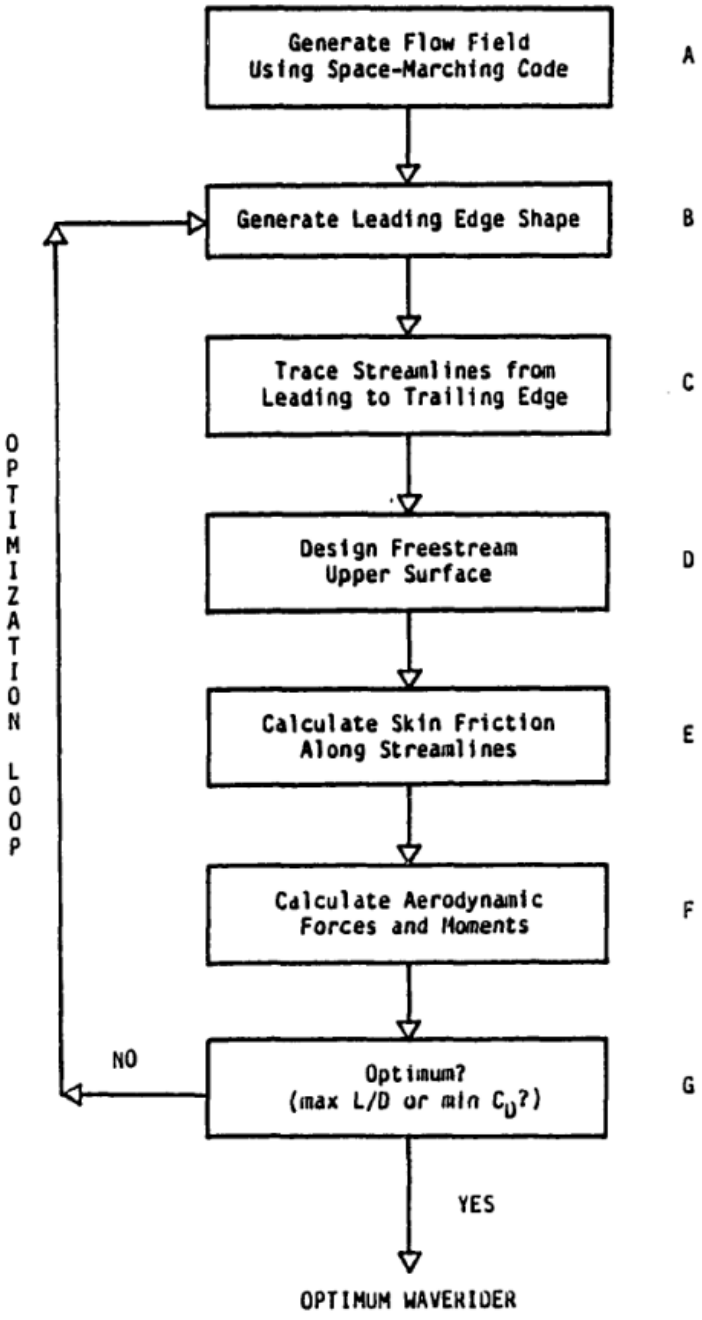

Figure 2.12. Waverider optimization scheme (24).

In general, the Simplex Method is a technique used to find the minimum or maximum of a function when you do not have access to its derivatives, only the values of the function itself.

It works by creating a simplex, which is a geometric figure with $n+1$ points (vertices) in n dimensions. For example, in 2D, a simplex is a triangle; in 3D, it's a tetrahedron.
Here's the basic idea:

At each iteration, the method evaluates the function at all vertices of the simplex. It identifies the vertex where the function is the worst (highest value if minimizing). Then it tries to replace that worst vertex by moving in directions like reflection, expansion, or contraction:

- Reflection: Flip the worst point across the centroid of the remaining points, hoping to find a better one.
- Expansion: If the reflection gives a really good new point, stretch further in that direction.
- Contraction: If the reflection doesn't help, pull the simplex inward toward better points.
- Shrinkage: If nothing works, shrink the whole simplex toward the best point.

The simplex gradually moves and deforms over the surface of the function until it finds the minimum (or maximum).
Key points about the Simplex Method:

- It does not require gradients (no need to compute derivatives).
- It is good for noisy, irregular, or complicated functions.
- It can be slower than methods that use derivatives but is often very robust.

The algorithm follows these steps (24):

First, define the objective function F as a function of n variables.

$$F = F(x_1, x_2, x_3, ..., X_n) \tag{2.101}$$

Then, generate an initial simplex consisting of $n+1$ vertices, each representing a set of variables.

$$X_j = X_j(x_1, x_2, x_3, ..., X_n) \tag{2.102}$$

Evaluate the objective function at each vertex and order the function values. Identify the worst vertex (highest function value) and order the functions such that:

$$F_1 < F_2 < F <_3 ... < F_n < F_{n+1} \tag{2.103}$$

Next, calculate the centroid of the best n vertices.

$$\bar{C} = \frac{1}{N} \sum_{j=1}^{n} X_j \tag{2.104}$$

Generate a new vertex X_r by reflecting the worst vertex across the centroid with α being the reflection coefficient.

$$X_r = \bar{C} + \alpha(\bar{C} - X_{n+1}) \tag{2.105}$$

After evaluating the objective function at the reflected point X_r, three possible actions are considered:

1. Regular Reflection

If the function value at the reflected point satisfies:

$$F_{\text{best}} < F_r < F_{\text{second worst}} \tag{2.106}$$

then X_r is better than the old worst point but not the best overall. In this case, replace the worst vertex X_{n+1} with X_r, and start a new iteration.

2. Expansion

If the reflected point is even better than the current best point, meaning:

$$F_r < F_1 \tag{2.107}$$

then an expansion step is attempted to explore even farther along the same direction. A new point X_e is computed as:

$$X_e = X_r + \gamma(X_r - \bar{C}) \tag{2.108}$$

where γ is the expansion coefficient (usually $\gamma = 2$).

If $F_e < F_r$, then X_e replaces X_{n+1}. Otherwise, keep the reflected point X_r. Then start a new iteration.

—

3. Contraction

If the reflected point is too large, meaning:

$$F_r > F_n \tag{2.109}$$

then a contraction step is attempted. There are two types:
Outside contraction (if $F_r < F_{n+1}$):

$$X_c = \bar{C} + \beta(X_r - \bar{C}) \tag{2.110}$$

Inside contraction (if $F_r > F_{n+1}$):

$$X_c = \bar{C} + \beta(X_{n+1} - \bar{C}) \tag{2.111}$$

where β is the contraction coefficient. If F_c is better than both F_r and F_{n+1}, accept X_c and replace the worst vertex. If contraction fails, shrink the entire simplex toward the best point:

$$X_c = \frac{X_c + X_1}{2} \tag{2.112}$$

Then start a new iteration.

The optimization is stopped after a specified number of iterations. Typically, 100 iterations are used to achieve convergence, with reflection, contraction, and expansion coefficients (α, β, γ) set to 1, 0.5, and 2, respectively (24).

Constraints are enforced as barriers that the simplex is not allowed to cross, ensuring that the geometry remains feasible (24).

The optimization parameter is the leading edge curve of the waverider. This curve is defined by five points in the x-y plane between the centerline and the wingtip. Due to symmetry and geometric constraints, only eight variables actually define the curve (24).

To start the optimization, nine initial leading edge shapes are required, forming the basis simplex (24). These basis shapes are selected to be diverse. Six shapes are polynomials of the form (24):

$$y_{le} = C_1 + C_2 x_{le} + C_3 x_{le}^2 + C_4 x_{le}^3 \tag{2.113}$$

and three of the basis shapes are of the form (24):

$$y_{le} = C_5 + C_6(1 - cos\frac{\pi x_{le}}{r_s}) \tag{2.114}$$

$$y_{le} = C_7 + C_8 sin(\frac{\pi x_{le}}{r_s}) \tag{2.115}$$

x_{le} and y_{le} are the x and y coordinates of the leading edge. r_s is the radius of the shockwave at the base of the waverider (24).

The choice of basis shapes strongly influences the final optimized result. Finally, the optimized leading edge shape is traced by the best configuration found using the simplex method.

3. SolidWorks Flow Simulation Computational Fluid Dynamics (CFD)

The CFD analysis will be performed using SolidWorks Flow Simulation. SolidWorks Flow Simulation is an advanced Computational Fluid Dynamics (CFD) tool integrated within the SolidWorks 2025 student edition provided free to students enrolled at San Jose State University. It is a general parametric flow simulation tool that uses the finite-volume method to ”solve” the Navier-Stokes equations in order to simulate the flow of liquid or gas. It can also simulate heat transfer due to convection, radiation, and conduction.

Flow Simulation solves the Navier-Stokes equations, which represent the conservation of mass, momentum, and energy in fluid flows. These equations are enhanced with state equations and empirical formulas that account for how fluid properties like density, viscosity, and thermal conductivity vary with temperature. For inelastic non-Newtonian fluids, viscosity also depends on shear rate and temperature, while compressible liquids involve density changes with pressure. Each simulation is defined by its specific geometry and boundary and initial conditions (32).

The software models both laminar and turbulent flows. Laminar flow, characterized by smooth and stable motion, occurs at low Reynolds numbers. When the Reynolds number exceeds a critical point, turbulence arises, leading to chaotic and fluctuating flow behavior. Since most engineering flows are turbulent, Flow Simulation is primarily tailored for those conditions (32).

To handle turbulence, the software uses Favre-averaged Navier-Stokes equations, which capture the time-averaged influence of turbulence while still accounting for large-scale, time-dependent phenomena. This introduces turbulent stresses into the equations, which are modeled using the $k-\varepsilon$ turbulence model. This model solves transport equations for turbulent kinetic energy and its dissipation rate, providing the necessary closure for the system (32).

A unified system of equations governs both laminar and turbulent regimes, allowing the simulation to handle transitions between the two. Flow Simulation also accommodates moving walls by applying appropriate boundary conditions, and for rotating components, it operates in a rotating coordinate system (32).

3.1 Favre-averaged Navier-Stokes

As previously stated, Flow Simulation uses the Favre-averaged Navier-Stokes equations along with the $k-\varepsilon$ model to accurately simulate and predict turbulent flows by considering both averaged effects and direct influences of turbulence (33).

The Favre-averaged Navier-Stokes equations come from the formulations of mass, momentum and energy conservation laws and are as follows:

$$\frac{\partial \rho}{\partial t} + \frac{\partial (\rho u_i)}{\partial x_i} = 0 \tag{3.1}$$

$$\frac{\partial(\rho u_i)}{\partial t}+\frac{\partial}{\partial x_i}(\rho u_i u_j)+\frac{\partial P}{\partial x_i}-\frac{\partial}{\partial x_j}(\tau_{ij}+\tau_{ij}^R)+S_i \tag{3.2}$$

$$\frac{\partial \rho H}{\partial t}+\frac{\partial \rho u_i H}{\partial x_i}-\frac{\partial}{\partial x_j}\left(u_i(\tau_{ij}+\tau_{ij}^R)+q_j\right)+\frac{\partial P}{\partial t}-\tau_{ij}^R\frac{\partial u_i}{\partial x_j}+\rho E+S_i u_i+Q_H \tag{3.3}$$

$$H=h+\frac{u^2}{2} \tag{3.4}$$

For calculation of high speed compressible flows with shock waves, the following energy equation is used:

$$\frac{\partial \rho E}{\partial t}+\frac{\partial}{\partial x_i}\left(\rho u_i\left(E+\frac{P}{\rho}\right)-\frac{\partial}{\partial x_j}\left(u_i(\tau_{ij}+\tau_{ij}^v)+q_j\right)-\tau_{ij}^R\frac{\partial u_i}{\partial x_j}+\rho E+S_i u_i+Q_H\right) \tag{3.5}$$

Where

$$E=e+\frac{u^2}{2} \tag{3.6}$$

To predict turbulent flows, the Favre-averaged Navier-Stokes equations (FANS) are employed. These equations account for the time-averaged effects of turbulence on various flow parameters while directly incorporating large-scale, time-dependent phenomena. This approach leads to the emergence of additional terms known as the turbulent stresses, which require supplementary information for their resolution (33).

To close this system of equations, SolidWorks Flow Simulation utilizes transport equations specifically designed for turbulent kinetic energy and its dissipation rate. The model implemented for this purpose is the $k-\varepsilon$ model, which is a widely recognized approach in computational fluid dynamics (CFD) for modeling turbulence (33).

3.2 $k-\varepsilon$ Turbulent Stress Model

The k-epsilon ($k-\varepsilon$) turbulence model is one of the most widely used models in computational fluid dynamics (CFD) for simulating turbulent flow conditions. It is a two-equation model that provides a general description of turbulence through two transport equations: one for turbulent kinetic energy (k) and another for the rate of dissipation of turbulent kinetic energy (ε). This model was developed to improve upon earlier turbulence models, particularly the mixing-length model, by providing a more robust framework for predicting turbulent flows in various applications (33).

The equation governing turbulent kinetic energy (k) is given as:

$$\frac{\partial \rho k}{\partial t}+\frac{\partial \rho k u_i}{\partial x_i}=\frac{\partial}{\partial x_i}\left(\left(\mu+\frac{\mu_t}{\sigma_k}\right)\right)+\tau_{ij}^R\frac{\partial u_i}{\partial x_i}-\rho\varepsilon+\mu_t P_B \tag{3.7}$$

The equation for the dissipation rate (ε) is expressed as:

$$\frac{\partial \rho \varepsilon}{\partial t} + \frac{\partial \rho \varepsilon u_i}{\partial x_i} = \frac{\partial}{\partial x_i}\left(\left(\mu + \frac{\mu_t}{\sigma_\varepsilon}\right)\frac{\partial \varepsilon}{\partial x_i}\right) + C_{\varepsilon 1}\frac{\varepsilon}{k}\left(f_1 \tau_{ij}^R \frac{\partial u_i}{\partial x_i} + C_B \mu_t P_B\right) - f_2 C_{\varepsilon 2}\frac{\rho \varepsilon^2}{k} \quad (3.8)$$

with

$$\tau_{ij} = \mu s_{ij} \quad (3.9)$$

$$\tau_{ij}^R = \mu_t s_{ij} - \frac{2}{3}\rho k \delta_{ij} \quad (3.10)$$

$$s_{ij} = \frac{\partial u_i}{\partial x_j} + \frac{\partial u_j}{\partial x_k} - \frac{2}{3}\delta_{ij}\frac{\partial u_k}{\partial x_k} \quad (3.11)$$

$$P_B = -\frac{g_i}{\sigma_B}\frac{1}{\rho}\frac{\partial \rho}{\partial x_i} \quad (3.12)$$

with the following constants determined empirically:

$$c_\mu = 0.09 \quad (3.13)$$

$$c_{\varepsilon 1} = 1.44 \quad (3.14)$$

$$c_{\varepsilon 2} = 1.92 \quad (3.15)$$

$$\sigma_k = 1 \quad (3.16)$$

$$\sigma_\varepsilon = 1.3 \quad (3.17)$$

$$\sigma_B = 0.9 \quad (3.18)$$

$$c_B = 1 \quad if \quad P_B > 0 \quad (3.19)$$

$$c_B = 0 \quad if \quad P_B < 0 \quad (3.20)$$

The turbulent viscosity term μ_t is determined from :

$$\mu_t = f_u \frac{C_u \rho k^2}{\varepsilon} \quad (3.21)$$

$$f_u = (1 - e^{-0.025 R_y})^2 \left(1 + \frac{20.5}{R_t}\right) \quad (3.22)$$

$$R_y = \frac{\rho\sqrt{k}y}{\mu} \tag{3.23}$$

$$R_t = \frac{\rho k^2}{\mu\varepsilon} \tag{3.24}$$

$$f1 = 1 + \left(\frac{0.05}{f_u}\right)^3 \tag{3.25}$$

$$f_2 = 1 - e^{R_t^2} \tag{3.26}$$

The heat flux q_i is defined by:

$$q_i = \left(\frac{\mu}{Pr} + \frac{\mu_t}{\sigma_c}\right)\frac{\partial h}{\partial x_i} \tag{3.27}$$

3.3 Heat transfer

SolidWorks Flow simulation has the ability to calculate heat transfer through conduction, Joule heating, and radiation. Heat transfer in fluids is described by the energy equation, equation 3.3, while the heat flux is defined by equation 3.27.

3.3.1. Conduction

The phenomenon of heat conduction in solid media is described by the following equation (32):

$$\frac{\partial \rho e}{\partial t} = \frac{\partial}{\partial x_i}\left(\lambda_i \frac{\partial T}{\partial x_i}\right) + Q_H \tag{3.28}$$

where e is the specific internal energy,

$$e = CT \tag{3.29}$$

and C the specific heat and Q_H the specific heat release per unit volume. λ_i are the eigenvalues of the thermal conductivity tensor. For an isotropic medium:

$$\lambda_1 = \lambda_2 = \lambda_3 = \lambda \tag{3.30}$$

3.3.2. Joule Heating

For Joule Heating, the specific Joule heat released from an isentropic material Q_J is given as:

$$Q_J = r \cdot i^2 \tag{3.31}$$

Where r is the solids resistivity and i is the electric current density vector given as:

$$i = -\left(\frac{1}{r_{11}}\frac{\partial \phi}{\partial x_1}, \frac{1}{r_{22}}\frac{\partial \phi}{\partial x_2}, \frac{1}{r_{33}}\frac{\partial \phi}{\partial x_3}, \right) \tag{3.32}$$

The electric current density vector i is found from the electric potential ϕ. Flow Simulation uses the steady state Laplace equation:

$$\frac{\partial}{\partial x_i}\left(\frac{1}{r_{ii}}\frac{\partial \phi}{\partial x_i}\right) = 0 \tag{3.33}$$

The Laplace equation is solved numerically within sub-domains containing electrically conductive materials, excluding dielectric and fluid regions. Users can specify electric current or potential as boundary conditions. Interfaces between conductive solids are assumed to have zero resistance unless a specific contact resistance is defined, which causes Joule heating and creates surface heat sources. Thermal contact resistance is considered between different solid materials, leading to temperature steps at interfaces. Thin material layers are modeled similarly using their thermal conductivity and thickness. Heat exchange between solids and fluids is calculated via normal heat flux, considering surface temperatures, fluid boundary layers, and radiation if applicable (33).

3.3.3. Radiation

For heat transfer through radiation, SolidWorks Flow Simulation offers two simplified models (33):

1) **Ray Tracing**, also known as **Discrete Transfer**
2) **Discrete Ordinates** (Discrete ordinates is only available for the HVAC module and not relevant to aerodynamics)

Ray Tracing assumes diffuse radiation emission and reflection (Lambert's law), with solar and thermal radiation treated separately. Solids can be set as transparent to various types of radiation, with optional refraction. Fluids are transparent to thermal radiation. Surfaces are modeled as gray bodies unless otherwise specified, and spectrum dependency is ignored (33).

The main idea of discrete transfer is that radiation from a surface can be approximated by rays traveling in specific directions. These rays carry heat and are traced through transparent media until they reach another radiative surface. This method, known as ray tracing, enables the calculation of exchange factors, which represent how much radiation energy is transferred between surfaces. The exchange factors are calculated as the fractions of the total radiation energy emitted from one of the radiative surfaces that is intercepted by other radiative surfaces (this quantity is a discrete analog of view factors). The exchange factors between the radiative surface mesh elements are calculated in the initial stage of the solver, it allows one to form a matrix of coefficients for a system of linear equations which is solved on each iteration (32). The following assumptions are made for the Discrete Transfer model (32):

- Diffuse radiation: Emitted and reflected radiation from solid surfaces (except symmetry types) is diffuse, following Lambert's law—radiation intensity is uniform in all directions.
- Graybody assumption: Non-blackbody/whitebody surfaces are treated as ideal graybodies with emissivity independent of wavelength, though it may vary with temperature.
- Solar vs. thermal radiation: Solar radiation interacts with surfaces separately from thermal radiation emitted by other sources.
- Radiation transparency: Specified solids can be transparent to thermal radiation, solar radiation, or both, allowing radiation to pass through without absorption.

In the ray-tracing model, radiative surfaces can emit, absorb, and reflect both solar and thermal radiation. Equation 3.35 defines the thermal radiation.

$$Q_T^{\text{out}} = \varepsilon \cdot \sigma \cdot T^4 \cdot A + (1-\varepsilon) \cdot Q_T^{\text{in}} \tag{3.34}$$

Where ε is the surface emissivity. σ is the Stefan-Boltzmann constant. T is the temperature of the surface. $(\varepsilon \cdot \sigma \cdot T^4)$ is the heat flux radiated by this surface in accordance with the Stefan-Boltzmann law. A is the radiative surface area. Q_T^{in} is the incident thermal radiation that reaches this surface (32).

Equation 3.35 defines the solar radiation. The net radiation Q^{net} for each surface is calculated as the difference between the outgoing radiation Q^{out} and the incoming radiation Q^{in}.

- $Q_s{}^{in}$: solar radiation arriving at the surface
- $Q_s{}^{source}$: solar radiation from solar sources

The net radiation equation 3.36, is calculated for all surfaces involved in radiation heat transfer.

$$Q_s^{\text{out}} = (1-\varepsilon) \cdot (Q_s^{\text{in}} + Q_s^{\text{source}}) \tag{3.35}$$

$$Q^{\text{net}} = Q^{\text{out}} - Q^{\text{in}} = (Q_T^{\text{out}} + Q_s^{\text{out}}) - (Q_T^{\text{in}} + Q_s^{\text{in}}) \tag{3.36}$$

To reduce memory and computational requirements, radiative heat transfer is calculated using a discrete ray Monte Carlo method. This approach begins by clustering mesh cells that approximate radiative surfaces, based on criteria such as face area and orientation. Clusters are formed to minimize the number of radiation rays needed, except when surfaces with different emissivities meet—those cells remain separate. This clustering process is applied after the creation of the mesh and after any adaptive mesh refinement (32).

From each cluster, radiation rays are emitted within a hemisphere defined by the surface normal. This hemisphere is divided into nearly equal solid angles using several zenith (latitudinal) and azimuth (longitudinal) angles. A ray is emitted randomly within each solid angle and traced through fluid and transparent solids until it strikes another radiative surface, known as a target cluster. The number and orientation of these rays determine the accuracy of the heat transfer between surfaces, though the net radiated heat from a surface remains constant regardless of ray count (32).

The total number of rays emitted from each cluster depends on the View Factor resolution level, which can be adjusted by the user. A higher resolution level increases accuracy but also significantly raises computation time and resource demands. During the simulation, the number of emitted rays may automatically increase for clusters with higher surface temperatures and emissivity, helping to evenly distribute heat across solid angles (32).

When a ray reaches a target cluster, the associated heat is evenly distributed over the area of the cluster. If multiple rays strike the same cluster, their heat is similarly shared. To further smooth out any uneven heat distribution, a portion of the incident radiation can also be shared with neighboring clusters. Additionally, solid heat conduction helps to reduce small temperature fluctuations across surfaces (32).

The exchange factor F_{ij} represents the portion of total radiation energy emitted from one cluster that is intercepted by another. To compute this, radiation rays are emitted from the center of a cluster point j in multiple directions and traced until they strike another point i. The incident radiation at point i, Q_i^{in}, is determined by summing the contributions from all rays reaching that point. Incident radiation is divided into two types: thermal and solar.

Incident thermal radiation, equation 3.37 is calculated based on contributions from surrounding radiative surfaces. while the incident solar radiation, equation 3.38 is based on rays originating from solar sources.

$$Q_{Ti}^{in} = \sum_j F_{ij} Q_{Tj}^{out} \tag{3.37}$$

$$Q_{Si}^{in} = \sum_j F_{ij} Q_{Sj}^{out} \tag{3.38}$$

The outgoing radiation from cluster i of Q_i^{out} includes both the portion of incoming radiation that is reflected and the surface's own emitted radiation. Separate expressions are used for thermal and solar radiation components denoted by the subscripts Ti, Si.

$$Q_{Ti}^{out} = (1-\varepsilon_i) Q_{Tj}^{in} + \varepsilon_i \sigma T_i^4 A_i \tag{3.39}$$

$$Q_{Si}^{out} = (1-\varepsilon_i)(Q_{Sj}^{in} + Q_{Sj}^{source}) \tag{3.40}$$

The solar radiation arriving at cluster i from solar sources is calculated using two methods, backward and forward solar ray tracing. In the backward method, rays are traced from the surface toward the solar sources. A ray reaches a boundary or a surface with suitable radiation conditions, and the exchange factor is estimated based on whether the solar source is visible to the cluster. In the forward method, rays are emitted from solar sources and evenly distributed, and the radiation received by each cluster is based on how many rays it intercepts. The forward method is preferred when dealing with refractive or reflective surfaces (32).

Backwards solar ray tracing is calculated with equation 3.41 while forwards solar ray tracing is calculated with equation 3.42 below:

$$Q_{\mathrm{Si}}^{\mathrm{source}} = \sum_k I_{S_k} \cdot F_{S_{ki}} \cdot \delta_{ki} \tag{3.41}$$

$$Q_{\mathrm{Si}}^{\mathrm{source}} = Q_{\mathrm{S}}^{\mathrm{ray}} \cdot N_i \tag{3.42}$$

$F_{S_{ki}}$ is the exchange factor and can be estimated using equation 3.43 below:

$$F_{S_{ki}} = (\eta_{S_k}, \mathbf{n}_i)_+ \cdot A_i \tag{3.43}$$

The I_{S_k} is the solar radiation intensity of the k-th solar source. The value δ_{ki} equals 1 if the i-th cluster is visible for the k-th solar source, and 0 if not (32).

$$Q_{\mathrm{S}}^{\mathrm{ray}} = \frac{\sum_k Q_{\mathrm{S}_k}^{\mathrm{source}}}{N_{\mathrm{rays}}} \tag{3.44}$$

The radiation transferred by each ray, $Q_{\mathrm{S}}^{\mathrm{ray}}$, can be estimated by summing up the radiation emitted by all solar sources, $Q_{\mathrm{S}_k}^{\mathrm{source}}$, and then divided by the number of emitted rays, N_{rays} (32). The value N_i is the number of rays intercepted the i-th cluster. The forward method is recommended in case of refraction and reflection radiative surfaces (32).

Flow Simulation allows users to select the solar ray tracing method and adjust the number of rays traced through the Calculation Control Options. It's important to note that the described equations focus only on cluster-to-cluster radiation transfer and exclude outer boundary and diffusive radiation sources, which are accounted for in the complete model. Heat fluxes from radiation are also taken into account in the energy balance at fluid-solid interfaces and within semi-transparent solids.

The discrete ordinates method (DOM) is a numerical approach used to solve the Radiative Transfer Equation (RTE) in media where radiation interacts with matter through absorption, emission, and sometimes scattering. Instead of treating radiation as traveling in all possible directions continuously, DOM simplifies the problem by dividing the angular domain into a finite set of discrete directions, called ordinates(34). The RTE is then solved along each of these directions.

To implement DOM, the entire solid angle around a point in space is discretized into specific angular segments. For each of these directions, the method calculates the radiation intensity, considering the contributions of emission from the medium, absorption of radiation passing through it, and any scattering that might occur. These individual directional solutions are then combined to compute quantities like the radiative heat flux and source terms through numerical integration over the discrete angles(34).

DOM is particularly useful in handling complex geometries and media with non-uniform properties. It allows detailed modeling of radiative behavior in environments such as combustion chambers, furnaces, and high-temperature flows. However, the accuracy of DOM depends on how finely the angular space is divided; too few directions can result in ray effects, which are artificial patterns in the solution due to limited angular resolution. To

improve accuracy, more discrete directions are used, but this also increases the computational cost (34).

The general form of the Radiative Transfer Equation is:

$$\frac{dI(\mathbf{r},\mathbf{s})}{ds} = -\kappa I(\mathbf{r},\mathbf{s}) + \kappa I_b(\mathbf{r}) + \sigma_s \int_{4\pi} I(\mathbf{r},\mathbf{s}')\Phi(\mathbf{s}',\mathbf{s})d\Omega' \tag{3.45}$$

- $I(\mathbf{r},\mathbf{s})$ is the radiation intensity at position $\mathbf{r}$ in the direction $\mathbf{s}$
- s is the distance along direction $\mathbf{s}$
- κ is the absorption coefficient
- $I_b(\mathbf{r}) = \sigma T^4/\pi$ is the blackbody intensity at local temperature T
- σ_s is the scattering coefficient
- $\Phi(\mathbf{s}',\mathbf{s})$ is the phase function describing scattering from direction $\mathbf{s}'$ to $\mathbf{s}$
- $d\Omega'$ is a differential solid angle element

In DOM, the angular domain 4π is discretized into N discrete directions $\mathbf{s}_n$ with associated weights w_n, and the RTE becomes (34):

$$\mathbf{s}_n \cdot \nabla I_n(\mathbf{r}) + \kappa I_n(\mathbf{r}) = \kappa I_b(\mathbf{r}) + \sigma_s \sum_{m=1}^{N} w_m \Phi(\mathbf{s}_m,\mathbf{s}_n) I_m(\mathbf{r}) \tag{3.46}$$

- $I_n(\mathbf{r})$ is the radiation intensity at point $\mathbf{r}$ in the direction $\mathbf{s}_n$
- The summation over m represents the discretized scattering integral

After solving the RTE for all directions, the radiative heat flux vector $\mathbf{q}_r$ is calculated by summing the directional contributions (34):

$$\mathbf{q}_r(\mathbf{r}) = \sum_{n=1}^{N} w_n I_n(\mathbf{r}) \mathbf{s}_n \tag{3.47}$$

And the radiative source term (used in the energy equation for heat transfer) is (34):

$$S_r(\mathbf{r}) = 4\pi\kappa I_b(\mathbf{r}) - \kappa \sum_{n=1}^{N} w_n I_n(\mathbf{r}) \tag{3.48}$$

These equations allow DOM to capture how radiation interacts with the medium and boundaries across discrete directions. The accuracy of the results depends on the number of directions (ordinates) and the spatial resolution of the problem (34).

3.4 Boundary Layers

SOLIDWORKS Flow Simulation uses non-body-fitted Cartesian meshes to create a seamless CAD/CFD bridge. This approach is ideal for handling native CAD geometry, but resolving near-wall boundary layers on coarse meshes presents challenges. To address this, the software employs an original Two-Scale Wall Function (2SWF) method to accurately model skin friction and heat flux at the wall, even with limited mesh resolution (33). This 2SWF method includes two main approaches (32):

1. **Thin-Boundary-Layer** Treatment is used when the mesh is too coarse to resolve the boundary layer accurately. It uses the Prandtl boundary layer equations integrated along the surface normal, solved along streamlines. For laminar flows, the Shvetz trial functions method is applied; for turbulent or transitional flows, a generalized form using Van Driest's mixing length model is used. This approach also considers surface roughness, turbulence, compressibility, and body forces through empirical corrections. From this, boundary layer thickness (δ), wall shear stress ($\tau^e w$), and wall heat flux ($q^e w$) are derived and used as boundary conditions in the main Navier-Stokes equations (33).

$$\tau_w = \tau_w^e \tag{3.49}$$

$$q_w = q_w^e \tag{3.50}$$

Boundary conditions for k and ε are determined from the condition of turbulence equilibrium in the near-wall computational mesh cell (33):

$$\frac{\partial k}{\partial y} = 0, \tag{3.51}$$

$$\varepsilon = \frac{C_\mu^{0.75} k^{1.5}}{\kappa y} \tag{3.52}$$

2. **Thick-Boundary-Layer** Approach is applied when the mesh has enough resolution (typically more than 10 cells across the boundary layer). Laminar boundary layers are resolved directly with the Navier-Stokes equations. For turbulent flows, a modified wall function is used, based on the full Van Driest velocity profile rather than the classical logarithmic law.

$$u^+ = \int_0^{y^+} \frac{2 \cdot d\eta}{1 + \sqrt{1 + 4 \cdot \kappa^2 \cdot \eta^2 \cdot \left[1 - \exp\left(-\frac{\eta}{A_v}\right)\right]^2}} \tag{3.53}$$

Karman constant:

$$\kappa = 0.4054 \tag{3.54}$$

Van Driest coefficient:

$$A_v = 26 \tag{3.55}$$

For intermediate cases, a smooth transition between the thin and thick models is used, ensuring continuity and accuracy as the mesh changes or the boundary layer evolves along the surface.

This hybrid approach enables SOLIDWORKS Flow Simulation to provide accurate boundary layer predictions directly from CAD models, without needing mesh body-fitted refinements.

3.5 Real Gases

SOLIDWORKS Flow Simulation supports modeling of real gases across a wide range of conditions, including both subcritical and supercritical regions. When a gas approaches the gas-liquid phase transition or exceeds its critical point, the ideal gas law becomes inaccurate, and the real gas model should be enabled to account for intermolecular forces and phenomena like the Joule-Thomson effect (32).

For such scenarios, Flow Simulation uses a modified version of the Redlich-Kwong equation. This equation is applied either in a user-defined or pre-defined form. The user-defined model allows one real gas (possibly mixed with ideal gases) and calculates properties using critical parameters (pressure, temperature, volume, and compressibility factor). Corrections for thermophysical properties like viscosity, thermal conductivity, and specific heat are added using semi-empirical equations (e.g., Jossi-Stiel-Thodos, Stiel-Thodos) depending on whether the gas is polar or non-polar (32).

Modified Redlich-Kwing Equation:

$$P_r = T_r \left(\frac{1}{\Phi_r - b} - \frac{a \cdot F}{\Phi_r \cdot (\Phi_r + c)} \right) \tag{3.56}$$

$$P_r = \frac{P}{P_c} \tag{3.57}$$

$$T_r = \frac{T}{T_c} \tag{3.58}$$

$$\Phi_r = V_r \cdot Z_c \tag{3.59}$$

$$V_r = \frac{V}{V_c} \tag{3.60}$$

$$F = T_r - 1.5 \tag{3.61}$$

The user-specified critical parameters of a gas define the gas's behavior at its critical point are:

- critical pressure (P_c)
- critical temperature (T_c)
- critical specific volume (V_c)

Along with the compressibility factor (Z_c), these parameters are used to calculate the constants a, b, and c in the real gas state equations (such as the modified Redlich-Kwong equation), which are essential for accurately modeling real gas behavior under non-ideal conditions. (33).

In addition to the Redlich-Kwong model, the Wilson, Barnes-King, and Soave modifications can be used to further refine calculations based on temperature dependence and the Pitzer acentricity factor.

Wilson Modification:

$$F = 1 + (1.57 + 1.62\omega)\left(T_r^{-1} - 1\right) \tag{3.62}$$

Barnes King Modification:

$$F = 1 + (0.9 + 1.21\omega)(T_r^{-1.5} - 1) \tag{3.63}$$

Soave Modification

$$F = \frac{1}{T_r}\left[1 + (0.48 + 1.574\omega + 0.176\omega^2)(1 - T_r^{0.5})^2\right]^2 \tag{3.64}$$

The software calculates specific heat at constant pressure (C_p) as a sum of a user-defined temperature-dependent polynomial and an automatically computed correction. C_v is then derived from C_p using the gas state equation.

The basic temperature dependency of a gas's dynamic viscosity (μ) is defined using a power-law function.

$$\mu = a \cdot T^n \tag{3.65}$$

For liquids, viscosity can be defined either with the same power-law form or with the exponential function shown below:

$$\mu = 10^{a\left(\frac{1}{T} - \frac{1}{n}\right)} \tag{3.66}$$

Corrections to these base values are applied depending on the gas's polarity. For non-polar gases, the Jossi-Stiel-Thodos equation is used, while for polar gases, the Stiel-Thodos equations are applied. These corrections account for pressure effects and improve accuracy in non-ideal conditions (32).

Similarly, the thermal conductivity (k) for both gases and liquids can be specified by the user using either a linear:

$$k = a + n \cdot T \tag{3.67}$$

or power-law form:

$$k = a \cdot T^n \tag{3.68}$$

and corrections are again determined using the Stiel-Thodos equations.

All coefficients must be provided in SI units, except those used in the exponential form of liquid viscosity, which must follow values specifically from Ref. 13. This modeling framework ensures accurate property predictions across a wide range of conditions, including subcritical and supercritical regions up to 1.1×Pc (32).

For pre-defined real gases, a variant of the Redlich-Kwong equation is used, where coefficients a, b, and c vary with reduced temperature to accurately represent both phase transitions (at $P < P_c$) and supercritical behavior (at $P > P_c$) (32).

$$P_r = T_r \cdot \left(\frac{1}{\Phi_r - b} - \frac{a}{\Phi_r \cdot (\Phi_r + c)} \right) \tag{3.69}$$

If a real gas is mixed with ideal gases, mixture properties are computed as mass or volume fraction weighted averages as seen in equation 3.70 below. However, mixtures of multiple real gases are not supported.The model has a few limitations:

- Accuracy may drop near the critical point or at supercritical pressures, especially for user-defined gases.
- User-defined property functions must be valid over the entire expected temperature range.
- The minimum temperature (T_{min}) for a user-defined gas must be set 5–10 K above the triple point.

$$v = \sum_{i=1}^{N} y_i v_i \tag{3.70}$$

Warnings are issued if simulation conditions exceed the model's valid range, and properties are then extrapolated linearly outside the supported region.

Compressible, liquids, those whose density varies with pressure and temperature, can be modeled using two main approximations:
1. Logarithmic law:

$$\rho = \rho_0 \cdot \left(1 + C \cdot \ln \left(1 + \frac{P - P_0}{B} \right) \right) \tag{3.71}$$

Here, ρ_0 is the density at reference pressure P_0, and C and B are coefficients that may depend on temperature. P is the computed pressure.
2. Power law:

$$\rho = \rho_0 \cdot \left(1 + \frac{P - P_0}{B} \right)^n \tag{3.72}$$

This form uses the same parameters as the logarithmic law, with the addition of n, a power index that can also vary with temperature.

If the liquid's dynamic viscosity (μ) is pressure-dependent, it can be modeled as:

$$\mu = \mu_0 \cdot \left(1 + a \cdot \ln \left(1 + \frac{P - P_0}{P'} \right) \right) \tag{3.73}$$

Where μ_0 is the viscosity at reference pressure P_0, a is a temperature-dependent coefficient, and $P' = 10^5\,\text{Pa}$ is a constant.

These models provide flexibility for accurately simulating the behavior of compressible liquids under various pressure and temperature conditions.

3.6 Mesh

In Flow Simulation, the meshing process begins with the creation of a rectangular computational domain that encloses the model geometry. This domain, aligned with the

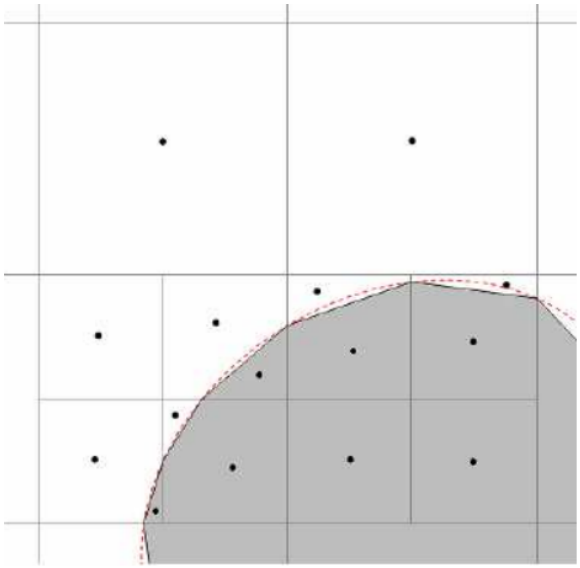

Figure 3.1. Rectangular mesh domain (32).

global coordinate system, is automatically adjusted depending on whether the simulation is internal or external. For internal flows, the domain wraps either around the flow passage or the entire model, depending on whether heat conduction in solids is enabled. For external flows, the domain is expanded away from the model automatically (32).

The meshing itself starts with a basic mesh, which divides the computational domain into uniform rectangular cells referred to as zero-level cells. Based on this foundation, Flow Simulation builds the initial mesh by applying various types of refinement. These refinements subdivide the basic cells further to better represent complex geometry, boundary layers, and regions with high gradients in the flow or temperature fields. Each refinement can occur up to nine levels deep, where each subsequent level represents a cell eight times smaller in volume than the previous (32).

The cells in the computational mesh are categorized as fluid cells, which are fully within the fluid region; solid cells, which are entirely inside solid geometry; and solid-fluid boundary cells, which intersect both regions. The meshing system ensures that these cells conform to a rule called the Cell Mating rule, which restricts neighboring cells to have refinement levels that differ by no more than one. This rule ensures smooth transitions and numerical stability (32).

Mesh refinement is carried out based on specific geometric and physical criteria. Cell Type Refinement ensures that both fluid and solid regions meet a minimum refinement level. Small Solid Features Refinement targets sharp features or small geometries by identifying cells where the angle between surface normals exceeds 120 degrees. Curvature Refinement focuses on smooth but curved surfaces, refining cells where curvature exceeds a user-defined threshold. Tolerance Refinement controls how closely polygonal mesh surfaces approximate actual curved surfaces, splitting cells when this approximation error exceeds a set limi (32)t.

Channel Refinement is applied to resolve narrow flow passages by ensuring a sufficient number of cells across the channel height. It works by evaluating the width between solid-fluid boundary cells and adjusting the mesh to meet the user-defined characteristic number of cells. The refinement occurs only if the resulting cell size does not exceed the maximum allowable refinement level for that region.

Thin walls, unlike channels, can sometimes be resolved within a single cell because their opposite faces may lie within the same computational cell. This technique reduces the need for excessive refinement while maintaining accuracy in heat transfer and flow predictions across thin surfaces.

Flow Simulation includes Automatic Parameters Definition (APD), a tool that sets mesh and refinement settings based on model dimensions, flow type, minimum feature sizes, and initial mesh level. APD configures the computational domain size, control planes, cell count, and refinement levels automatically, ensuring a balanced mesh without manual input (32).

Control planes are used to stretch or contract the basic mesh in targeted regions. By setting these planes along the global coordinate directions and assigning appropriate ratios, users can locally refine or coarsen the mesh to optimize accuracy and performance (32).

Local mesh settings allow more detailed mesh zones within specific areas, using geometric entities like bodies, faces, edges, or volumes. These settings override the global mesh controls and are especially useful for resolving areas with small features, high gradients, or complex boundary interactions. Equidistant Refinement within local settings enables mesh generation based on distance from selected geometry (32).

To ensure the mesh adequately resolves critical features, it is important to test mesh convergence. This involves running multiple simulations with progressively finer meshes and observing whether results such as velocity, pressure, or temperature stabilize. Once additional refinement no longer significantly changes the results, mesh convergence is considered achieved, and the mesh can be deemed sufficiently accurate (32).

3.7 Numerical Solver

Flow Simulation uses a numerical solution technique that typically does not require users to understand or adjust mesh or solver parameters. However, for complex models that demand excessive computational resources, users can manually tune solver settings to optimize performance.

The solver is based on the finite volume method (FVM) applied to a Cartesian coordinate system. For most of the domain, a regular axis-aligned rectangular grid is used. Near geometry boundaries, a Cartesian cut-cell approach is employed. In this approach, standard rectangular cells that intersect the geometry are cut to form polyhedral cells, which better represent the model's surface while still leveraging the efficiency of a regular grid in the bulk domain (32).

Mesh refinement is applied automatically and locally, especially around solid-fluid interfaces and regions with high solution gradients, enhancing accuracy where needed.

Physical quantities such as mass, momentum, and energy are associated with the centers of control volumes, and the solver directly discretizes the integral forms of the governing

equations. This ensures conservation of mass, momentum, and energy in the numerical solution.

Spatial derivatives are approximated using second-order implicit difference schemes, while time derivatives are handled with a first-order implicit Euler method. This combination results in low numerical diffusion and sufficient accuracy for most practical engineering problems.

Flow Simulation uses a Cartesian-based finite volume method with a locally refined rectangular mesh to solve fluid flow and heat transfer problems. The mesh is constructed automatically and aligns with the global coordinate system. Far from geometry boundaries, mesh cells are standard rectangular parallelepipeds. Near geometry boundaries, a cut-cell approach is used: curved surfaces are approximated using flat polygons that cut through the original cells, resulting in polyhedral cells with a mix of axis-aligned and arbitrarily oriented faces. These cells are then classified as fluid or solid volumes. The meshing process follows multiple stages (32):

- A basic mesh is created by slicing the computational domain into uniformly sized cells based on user-defined control planes and cell counts.
- Cells intersecting the solid/fluid interface are recursively refined by dividing them into eight smaller child cells until the target resolution is achieved.
- Further refinement is applied based on the curvature of the solid/fluid interface. Cells are split if the angle between surface normals within the cell exceeds a set threshold.
- Additional refinement is done to resolve narrow channels, ensuring a minimum number of cells exist across a channel in the direction normal to the solid/fluid boundary.

This process produces a final mesh composed of both regular and refined polyhedral cells, optimized for accuracy and computational efficiency.

If more resolution is needed during the simulation, solution-adaptive mesh refinement can be triggered at specific times. This refinement increases resolution in high-gradient regions by splitting cells, while coarsening is applied in low-gradient areas by merging cells (32).

To accurately model boundary layers, Flow Simulation employs the Two-Scales Wall Functions (2SWF) model, which dynamically selects between two wall modeling strategies based on the mesh resolution. When the mesh is fine, with six or more cells across the boundary layer, the thick-boundary-layer approach is applied. In this method, laminar flow is calculated using the Navier-Stokes equations, while turbulent flow relies on a modified wall function. Instead of the classical logarithmic velocity profile, the Van Driest profile is used, with other assumptions remaining similar to the traditional wall function approach (32).

For coarse meshes with four or fewer cells across the boundary layer, the thin-boundary-layer approach is used. This involves solving the Prandtl boundary layer equations integrated from the wall up to the boundary layer thickness along streamlines. In laminar regions, the method uses Shvetz trial functions, and for turbulent or transitional flows, it generalizes this method using Van Driest's hypothesis on mixing length in turbulent boundary layers (32).

In cases where the mesh falls between fine and coarse, a combination of both approaches ensures a smooth transition between models as the boundary layer develops or the mesh is refined (32).

Additionally, the thin-channel approach is used to simulate flow through narrow slots or channels when the mesh across the slot has seven or fewer cells. This method estimates shear stress and heat flux near walls using approximations derived from experimental data (32).

The simulation software automatically selects the most appropriate model based on mesh resolution. Generally, all these approaches maintain good accuracy, even with a coarse mesh. However, accuracy may drop when the mesh is too fine for the thin-boundary-layer approach but not refined enough for the thick-boundary-layer model. In such cases, improving the mesh resolution can gradually enhance the accuracy of the solution (32).

The cell-centered finite volume (FV) method is used to obtain conservative approximations of the governing equations on a locally refined grid. This grid is made up of parallelepipeds and more complex polyhedrons near boundaries. The FV method involves integrating the governing equations over each control volume, which corresponds to a mesh cell, and then approximating them. All primary variables are associated with the mass centers of the control volumes, and these cell-centered values are used for the approximations.

The integral conservation laws are expressed through cell volume and surface integrals:

$$\frac{\partial}{\partial t}\int U\,dv + \oint \mathbf{F}\,ds = \int Q\,dv \tag{3.74}$$

which are then converted into discrete the form:

$$\frac{\partial}{\partial t}(U \cdot v) + \sum_{N_c} F \cdot S = Q \cdot v \tag{3.75}$$

with N_c being the number of faces of the cell in the formulation. Fluxes (F) across cell faces are approximated based on the type of face. Faces are categorized into two groups: axis-oriented faces common to two adjacent control volumes, and arbitrarily oriented boundary faces. Different approximation strategies are applied to each group.

For faces shared by two adjacent cells, second-order approximations are used. Convective fluxes are treated using an upwind approach, and nonlinear approximations with limiters are applied to ensure monotonic discrete solutions. For diffusive terms, a central difference approximation is employed. All these approximations are treated implicitly.

To ensure high fidelity to the original differential equations, Flow Simulation uses particularly consistent approximations for convective terms by employing 'div' and 'grad' operators. This method not only preserves the conservation of mass, momentum, and energy but also maintains key properties of the original mathematical problem.

On arbitrarily oriented boundary faces, the fluxes are approximated according to the specified boundary conditions while also considering the effects of curved boundary geometries. To accurately calculate boundary fluxes at the solid/fluid interface, Flow Simulation uses an advanced boundary layer model.

Conjugate heat transfer between fluid and solid regions is handled simultaneously as a single unified problem, rather than splitting it into two separate, explicitly connected problems. This approach ensures a more accurate and consistent simulation of thermal interactions across interfaces.

The time derivatives are approximated using an implicit first-order Euler scheme. The continuity and convection/diffusion equations for quantities like momentum and temperature are treated with time-implicit approximations combined with an operator-splitting technique. This technique improves efficiency and addresses the issue of pressure-velocity decoupling.

Using a SIMPLE-like approach (33), an elliptic-type discrete pressure equation is derived by algebraically transforming the discrete mass and momentum equations while incorporating the boundary conditions for velocity. This method ensures stable and accurate coupling between pressure and velocity fields during the simulation.

The numerical algorithm for advancing from time-level n to $n+1$ uses intermediate flow parameter values, denoted by an asterisk (*), and follows a structured multi-step process using the equations below:

$$\frac{U^* - U^n}{\Delta t} + A_u(U^n, p^n)U^* = S^n \tag{3.76}$$

$$L_h \delta P = \frac{\mathrm{div}_h(\rho \mathbf{u}^*)}{\Delta t} + \frac{1}{\Delta t}\frac{\dot{\rho} - \rho^n}{\rho^n} \tag{3.77}$$

$$\rho^* = \rho(p^n + \delta p, T^*, y^*) \tag{3.78}$$

$$\rho^{n+1} = \rho^* - \Delta t \cdot \nabla \cdot \delta P \tag{3.79}$$

$$p^{n+1} = p^n + \delta p \tag{3.80}$$

$$\rho T^{n+1} = \rho T^* \tag{3.81}$$

$$\rho K^{n+1} = \rho K^* \tag{3.82}$$

$$\rho e^{n+1} = \rho e^* \tag{3.83}$$

$$\rho y^{n+1} = \rho y^* \tag{3.84}$$

$$\rho^{n+1} = \rho\left(\mathbf{p}^{n+1}, T^{n+1}, \mathbf{y}^{n+1}\right) \tag{3.85}$$

The full set of basic flow variables, excluding pressure, is grouped into a vector $U = (\rho u, \rho T, \rho \kappa, \rho \varepsilon, \rho y)^T$, where $u = (u_1, u_2, u_3)^T$ is the velocity vector, and $y = (y_1, y_2, ..., y_M)^T$ represents component concentrations in fluid mixtures. Pressure correction, denoted as $\delta p = p^{n+1} - p^n$, is introduced to properly adjust the velocity field.

The discrete functions U, u, and δp are all stored at the centers of mesh cells, and discrete operators A_h, div_h, grad_h, and $L_h = \mathrm{div}_h \mathrm{grad}_h$ are used to approximate the corresponding differential operators with second-order accuracy.

The algorithm proceeds as follows:

First, equation 3.76 is solved to obtain intermediate values. This step involves solving fully implicit discrete convection-diffusion equations for momentum, as well as final values for turbulent parameters, temperature, and species concentrations.

Next, equation 3.77, an elliptic-type equation, is solved to compute the pressure correction δp. The pressure correction ensures that the final momentum field ρu^{n+1}, obtained from adjusting the intermediate momentum field, satisfies the fully implicit discrete continuity equation.

After obtaining the pressure correction, final updated values for flow parameters are determined through equations 3.79 to 3.85, completing the advancement to time-level $n+1$.

This process ensures that mass, momentum, energy, and species conservation laws are all satisfied with high accuracy while maintaining numerical stability.

Several methods are used to solve the linear algebraic systems that arise from discretizing the governing equations.

For non-symmetric problems, such as those resulting from the approximations of momentum, temperature, and species equations (described in equation 3.76), a preconditioned generalized conjugate gradient method is employed. In this method, an incomplete LU factorization is used as the preconditioner to accelerate convergence.

For symmetric problems, particularly the pressure-correction equation (3.77), a double-preconditioned iterative procedure is applied. This approach is based on a specially developed multi-grid method designed for high efficiency.

The multi-grid method itself is a key acceleration technique. It constructs a hierarchy of coarser grids from the original mesh. The residuals of the algebraic systems are transferred to these coarser grids to form new right-hand sides. Solutions on coarse grids are interpolated back to finer grids as corrections, and smoothing iterations are performed at each level. This multilevel procedure greatly reduces the overall solution time. The system coefficients for each grid level are computed once and stored to optimize performance.

Additionally, Flow Simulation applies a technique called nested iterations. Instead of solving the full non-linear set of equations with non-linear boundary conditions simultaneously, each equation is solved separately in a linearized form. Within each time step, nested iterations are carried out, treating the interaction between flow parameters and non-linear terms more accurately. These iterations are repeated until solver convergence is achieved, a maximum number of iterations is reached, or all conservation law convergence conditions (mass, energy, and momentum) are satisfied.

The convergence criteria for mass, energy, and momentum equations during nested iterations are based on residual errors and corresponding reference residual values. These ensure that the solution is sufficiently accurate at each time step before moving forward.

3.7.1. Criterion for Mass Equation Convergence

At each nested iteration, the residual error for mass conservation is calculated by comparing the predicted density ρ_k at $t+\Delta t$ with the initial density ρ_0. k being a number of the nested iteration. The residual over the domain is computed as:

$$r^k_{\text{mass}} = \left\| r^k_{mass,cv} \right\| = \sum_{\Omega} \left| r^k_{mass,cv} \right| \tag{3.86}$$

with $\sum_{\Omega}$ being the sum over all the control volume domains.

$$r^k_{mass,cv} = \frac{\rho^k - \rho^0}{\Delta t} V_{cv} + \sum_{f_{cv}} j^k_{fcv} \tag{3.87}$$

where $j_{mass,f_{cv}}$ is the mass flux at the control volume face (f_{cv}).
The reference residual value $r^{\text{ref}}_{\text{mass}}$ is defined based on the sum of inlet and outlet mass fluxes across each control volume.

$$r^k_{mass,ref} = \sum_{\Omega} r^k_{mass,cv,ref} = \sum_{\Omega} \sum_{f_{cv}} \left| j^k_{mass,f_{cv}} \right| = 2 \left\langle j_{mass,cv} \right\rangle \tag{3.88}$$

The stopping criterion for mass is:

$$r^k_{\text{mass}} \leq \varepsilon_{\text{mass}} \cdot r^k_{\text{mass, ref}} \tag{3.89}$$

where $\varepsilon_{\text{mass}}$ is a small tolerance value (user-defined or default).

$$\frac{\left\langle r_{mass,cv} \right\rangle^k}{2 \left\langle j_{mass,cv} \right\rangle^k} \leq \varepsilon_{mass} \tag{3.90}$$

3.7.2. Criterion for Energy Equation Convergence

Similarly, the residual error for the energy equation r^k_{en} is based on the difference between the calculated and expected heat transfer.

$$r^k_{\text{en},cv} = \left\| r^k_{en,cv} \right\|_1 = \sum_{\Omega} \left| r^k_{en,cv} \right| \tag{3.91}$$

It uses a discrete operator L that approximates the convection and diffusion terms in the control volume.

$$L^k_{H,Conv+Diff}(H^k) = \sum_{j=\omega_{cv}} c_j \cdot H^k_j \tag{3.92}$$

ω_{cv} is a stencil of the operator L at the control volume (cv), c_0 is a coefficient for H in the control volume under consideration, and $c_{j(j\neq 0)}$ are coefficients for other control volumes from the stencil.

$$c_j \sim \left[\rho u_n + \frac{\frac{\lambda_h}{h_{cv}}}{2} \right] S_{f_{cv}} \tag{3.93}$$

u_n is the velocity component normal to the face and h_{cv} is the characteristic size of the control volume. The explicit member f_H^k contains approximations of other terms of the equation and the heat source at the face of the control volume is equal to $q \cdot V_{cv}$.
The residual error per control volume is:

$$r_{\text{en},cv}^k = \rho^0 \frac{(H^k + H^0)}{\Delta t} V_{cv} + L_{H,Conv+Diff}^k(H^k) - f_H^k \tag{3.94}$$

where H represents the enthalpy.
The reference value $r_{\text{en,ref}}^k$ is based on both convection/diffusion heat fluxes and internal heat sources.

$$r_{\text{en,ref}}^k = \sum_{\Omega} r_{en,cv,ref}^k = \sum_{\Omega} \left(max \left(\left| c_0 + \frac{\rho^0}{\Delta t} V_{cv} \right|, max_{j \in \omega, j \neq 0} |c_j| \right) \cdot |H^k| + \left| f_H^k + \frac{\rho^0 H^0}{\Delta t} V_{cv} \right| \right) \tag{3.95}$$

If $\Delta t \gg \frac{h_{cv}}{u_n} + \frac{h_{cv}^2}{\lambda_H / \rho}$, the first summation is the reference value of the energy flux through the control volume (cv). The second summation is the reference value of the energy flux in/out of the control volume due to the heat source $q \cdot V_{cv}$.

If Δt is small:

$$r_{en,cv,ref}^k \longrightarrow \infty \quad \text{as} \quad \Delta t \to 0 \tag{3.96}$$

The stopping criterion for energy is:

$$r_{\text{en}}^k \leq \varepsilon_{\text{en}} \cdot r_{\text{en,ref}}^k \tag{3.97}$$

$$\frac{\langle r_{en,cv} \rangle^k}{\langle j_{en,cv} \rangle^k} \leq \varepsilon_{en} \tag{3.98}$$

3.7.3. Criterion for Momentum Equation Convergence

The residual error for the momentum equation r_{mom}^k is computed similarly. It involves the difference between the intermediate momentum and the expected momentum, considering pressure gradients and external forces.

$$r_{mom}^k = \left\| r_{mom,cv}^k \right\|_1 = \sum_{\Omega} \left(\left| r_{mom_0 cv}^k \right| + |r_{mom_1 cv}^k| + |r_{mom_2 cv}^k| \right) \tag{3.99}$$

For each component of the velocity, the residual error at each ith component of the control volume is:

$$r^k_{mom,cv} = \frac{(m^i_k - m^0_i)}{\Delta t} V_b + L_{m_i,Conv+Diff}(m^k_i) - F^k_{m_i},\ i = 0,1,2 \tag{3.100}$$

$$L_{m_i,Conv+Diff}(m^k_i) = \sum_{j \in \omega_{cv}} c_{ij} \cdot m^k_{ij} \tag{3.101}$$

$$c_{ij} \sim \left(u_n + \frac{\mu + \mu_t}{\frac{h_{cv}}{2}} \right) S_{f_{cv}} \tag{3.102}$$

The reference value $r^k_{\text{mom,cv,ref}}$ is based on the momentum flux ($j_{mom,cv}$) through the control volume.

$$r^k_{mom,ref} = \sum_{\Omega} \left(\left| r^k_{mom_0,cv,ref} \right| + |r^k_{mom_1,cv,ref}| + |r^k_{mom_2,cv,ref}| \right) \tag{3.103}$$

$$r^k_{mom_i,cv,ref} = \sum_{\Omega} \left(max \left(\left| c_{i0} + \frac{V_b}{\Delta t} \right|, max_{j \in \omega, j \neq 0} |c_{ij}| \right) \cdot |m^k| + \left| f^k_{m_i} + \frac{m^0_i}{\Delta t} V_b \right| \right) \tag{3.104}$$

The stopping criterion for momentum is:

$$r^k_{\text{mom}} \leq \varepsilon_{\text{mom}} \cdot r^k_{\text{mom,ref}} \tag{3.105}$$

$$\frac{\langle r_{mom,cv} \rangle^k}{\langle j_{mom,cv} \rangle^k} \leq \varepsilon_{mom} \tag{3.106}$$

For each equation, convergence is achieved when the normalized residual error becomes smaller than a small fraction (like 10^{-3} or 10^{-4}) of the corresponding reference value. This ensures that all the physical conservation laws are accurately satisfied before moving on.

3.7.4. Residuals

Residuals provide a measure of how well the numerical solution satisfies the discrete equations, but they do not directly indicate the actual accuracy of the solution. In complex flows, it is often difficult to determine the correct time scale for unsteady processes. If the time step used in the simulation is too large compared to the characteristic time scale of the flow, the residuals may not decrease significantly, even though the physical process is being captured correctly.

Importantly, low residuals do not guarantee an accurate solution, and high residuals do not necessarily imply an incorrect solution. Residual behavior mainly reflects how well the numerical solver is balancing the current form of the equations, not the true physical fidelity.

To assess the accuracy of the simulation, convergence studies must be performed by decreasing the time step size and observing whether the physical parameters, such as pressure,

velocity, or temperature, converge toward consistent values. Only this method can reliably indicate the quality of the discrete solution.

4. SolidWorks Flow Simulation Martian Waverider Simulation

The waverider model selected for simulation in this study is based on the University of Maryland's viscous-optimized waverider design for Mars, as detailed in the work by Anderson Jr. (21). This particular configuration was chosen because of the availability of published data, including lift-to-drag (L/D) ratios, which serve as a benchmark for evaluating the accuracy of the present CFD simulations.

The selected waverider is specifically designed to perform an aero-gravity assist maneuver by executing a high-speed atmospheric flyby of Mars. During this maneuver, the vehicle dips into the upper layers of the Martian atmosphere, utilizing the lift generated at hypersonic speeds to alter its trajectory more significantly than would be possible through gravitational interaction alone. This aerodynamic contribution enhances the angular deflection of the spacecraft's path, allowing it to exit the flyby with a beneficial change in velocity vector. This technique can be especially valuable for interplanetary missions seeking fuel-efficient trajectory modifications without requiring significant propulsion expenditure.

To maximize aerodynamic efficiency during the maneuver, the waverider is designed to invert (fly upside down) upon atmospheric entry. This orientation allows it to generate lift in the direction that augments the natural curvature of its trajectory around the planet, effectively increasing the magnitude of the gravity assist. The ability of the waverider to maintain shock-attached flow along its leading edges ensures high lift and low wave drag throughout the maneuver, a performance advantage critical for hypersonic planetary applications.

The viscous-optimized design used here accounts for boundary layer growth and skin friction, which are especially important in Mars' thin, low-density atmosphere. By simulating this specific waverider configuration in SolidWorks Flow Simulation and comparing the resulting aerodynamic forces - particularly lift, drag, and L / D ratio with published values from (21), the study aims to validate the CFD model and assess its suitability for preliminary analysis of aeroassist trajectories. The ability to match or closely approximate the benchmark L/D values serves as an important metric for evaluating both the physical accuracy and computational reliability of the SolidWorks Flow Simulation framework under Martian hypersonic conditions.

The waverider CAD model, figure 4.1 used in this study was obtained from the open-source platform Thingiverse (22), which hosts publicly shared 3D models.

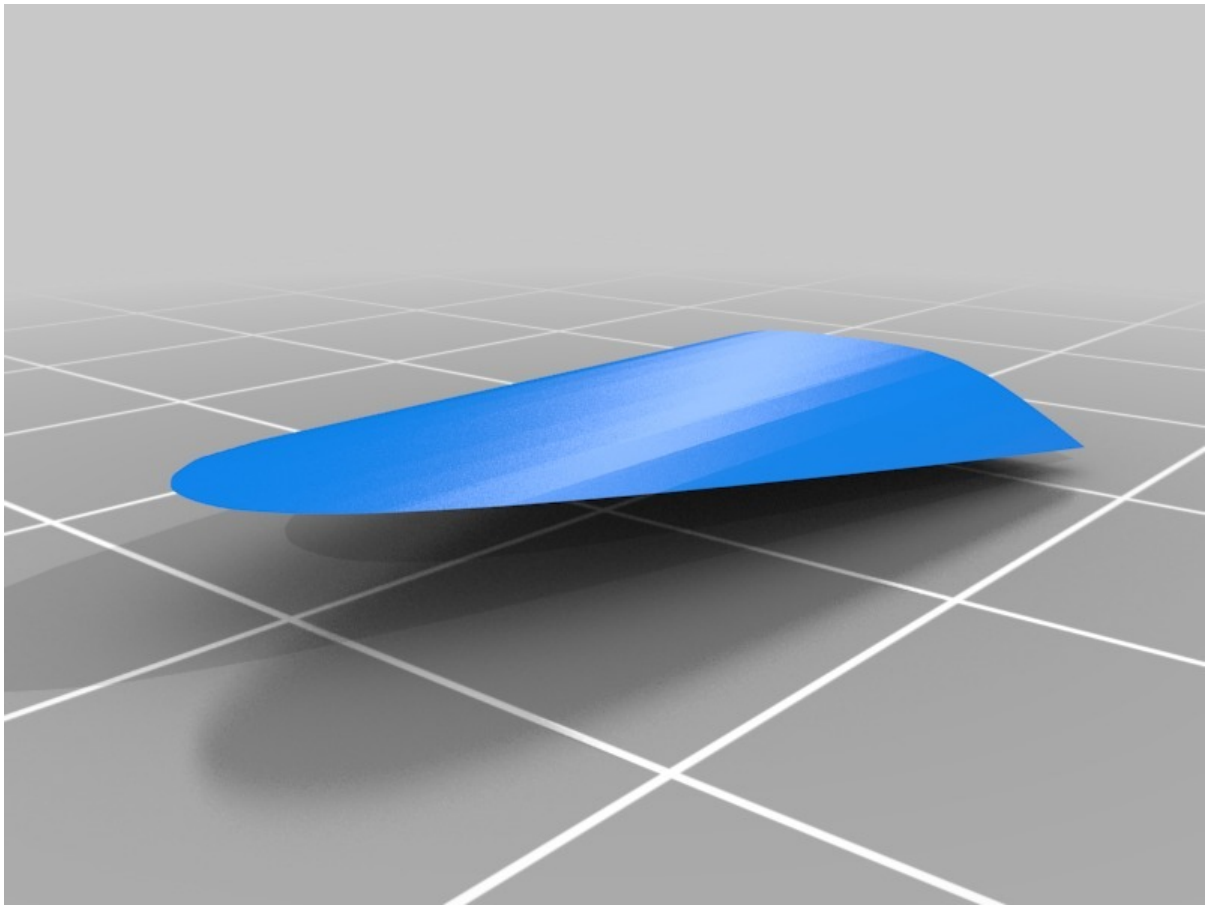

Figure 4.1. Conical waverider designed for Mars 3D CAD model (22).

4.1 Simulation Setup

The flow simulation setup for this study was established as an external compressible flow analysis using SolidWorks Flow Simulation, leveraging its seamless CAD integration to simulate aerodynamic performance around complex geometries. The waverider model, based on the University of Maryland's viscous-optimized Mars entry design (21), was imported into SolidWorks and processed using Boolean geometry recognition, allowing the software to clearly distinguish between the solid body and the surrounding fluid domain. This setting is depicted in Figure 4.2.

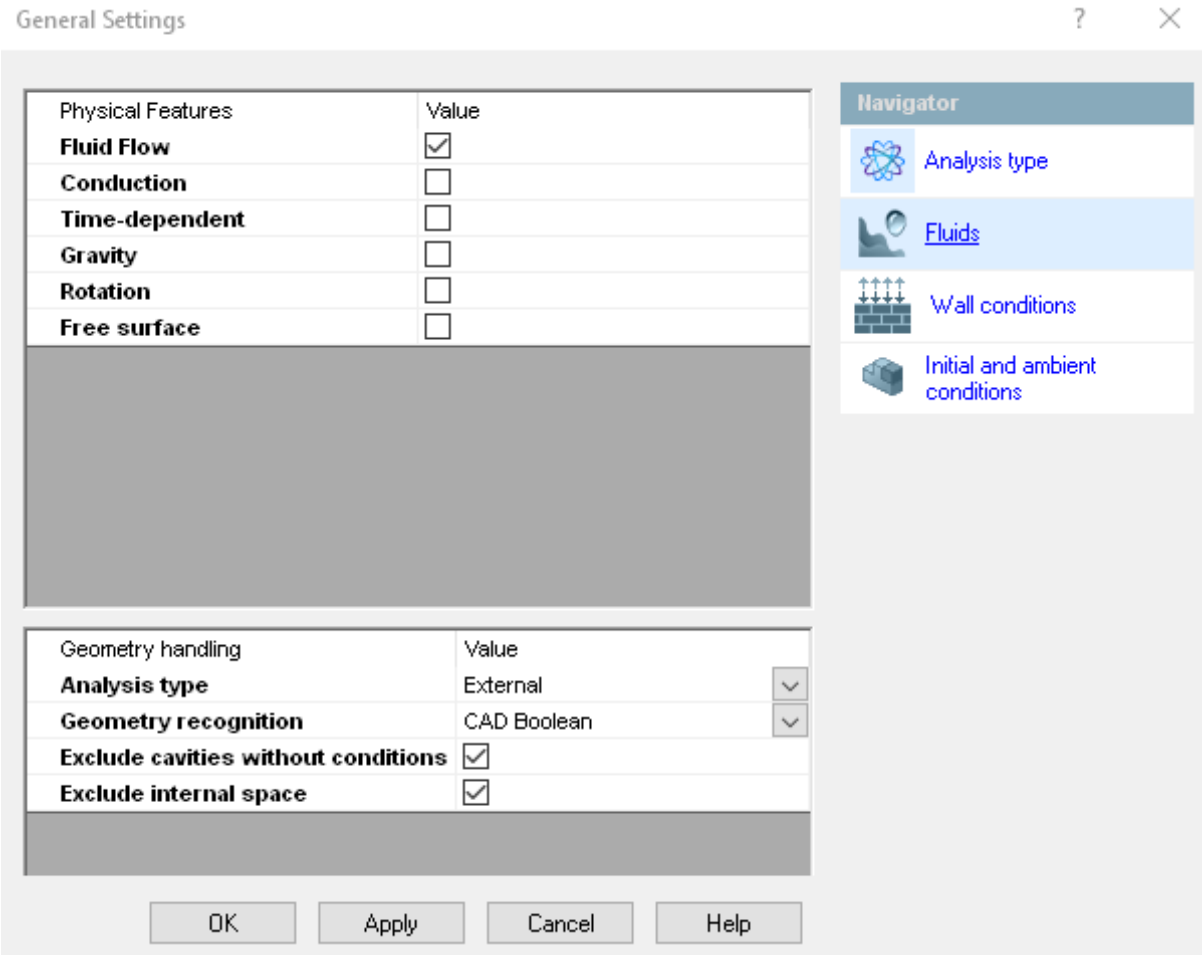

Figure 4.2. Analysis type.

To accurately replicate Martian flight conditions, the fluid domain was configured to simulate a perfect gas, with thermophysical properties aligned with a carbon dioxide-dominated atmosphere, as found on Mars. SolidWorks Flow Simulation includes a predefined gas model for the Martian atmosphere, available from its integrated engineering database, as shown in Figure 4.3. This simplifies the model setup for simulating compressible high-speed external flow over a hypersonic vehicle.

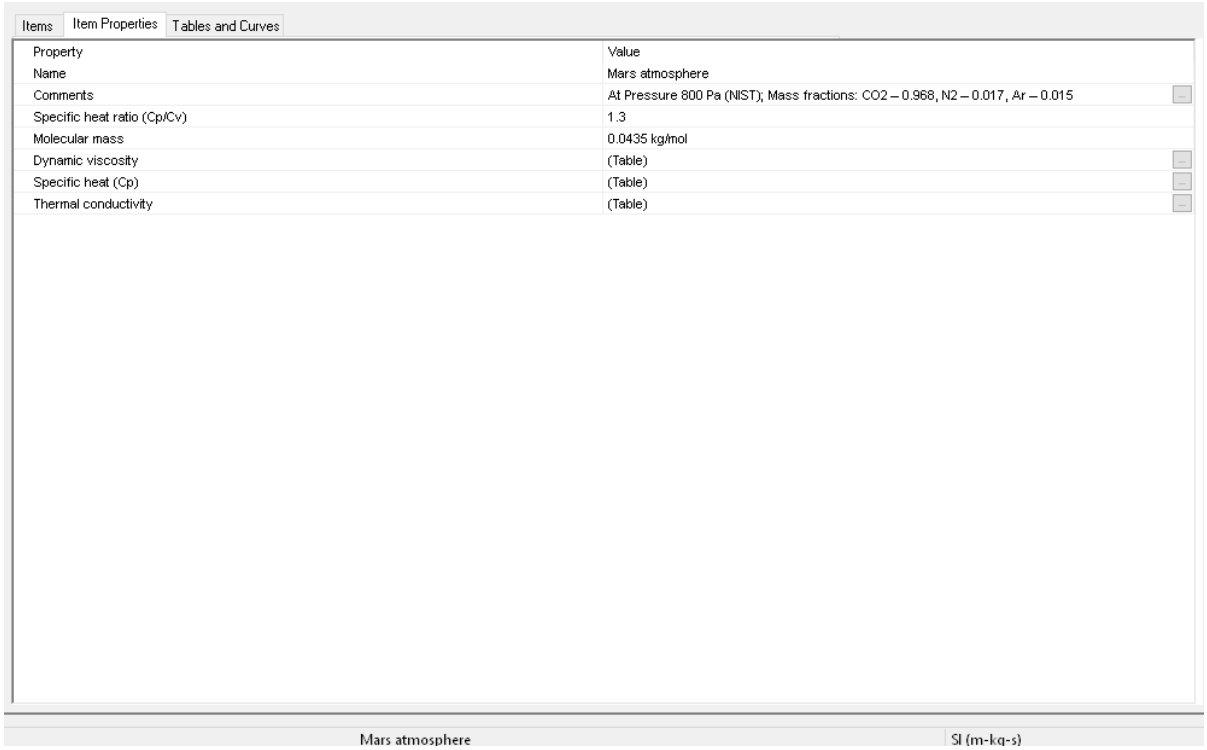

Figure 4.3. Mars atmosphere model.

Although SolidWorks treats carbon dioxide as a perfect gas in this configuration (i.e., assuming constant specific heats and neglecting real-gas or chemical reaction effects), this simplification is valid for the entry altitudes (20–30 km) and temperatures (1000 K) considered. These conditions fall below the thresholds where thermal dissociation or vibrational excitation become dominant. As such, the perfect gas assumption is sufficient for evaluating pressure distribution, skin friction, and lift-to-drag ratios, which are the primary aerodynamic metrics of interest in this preliminary design study.

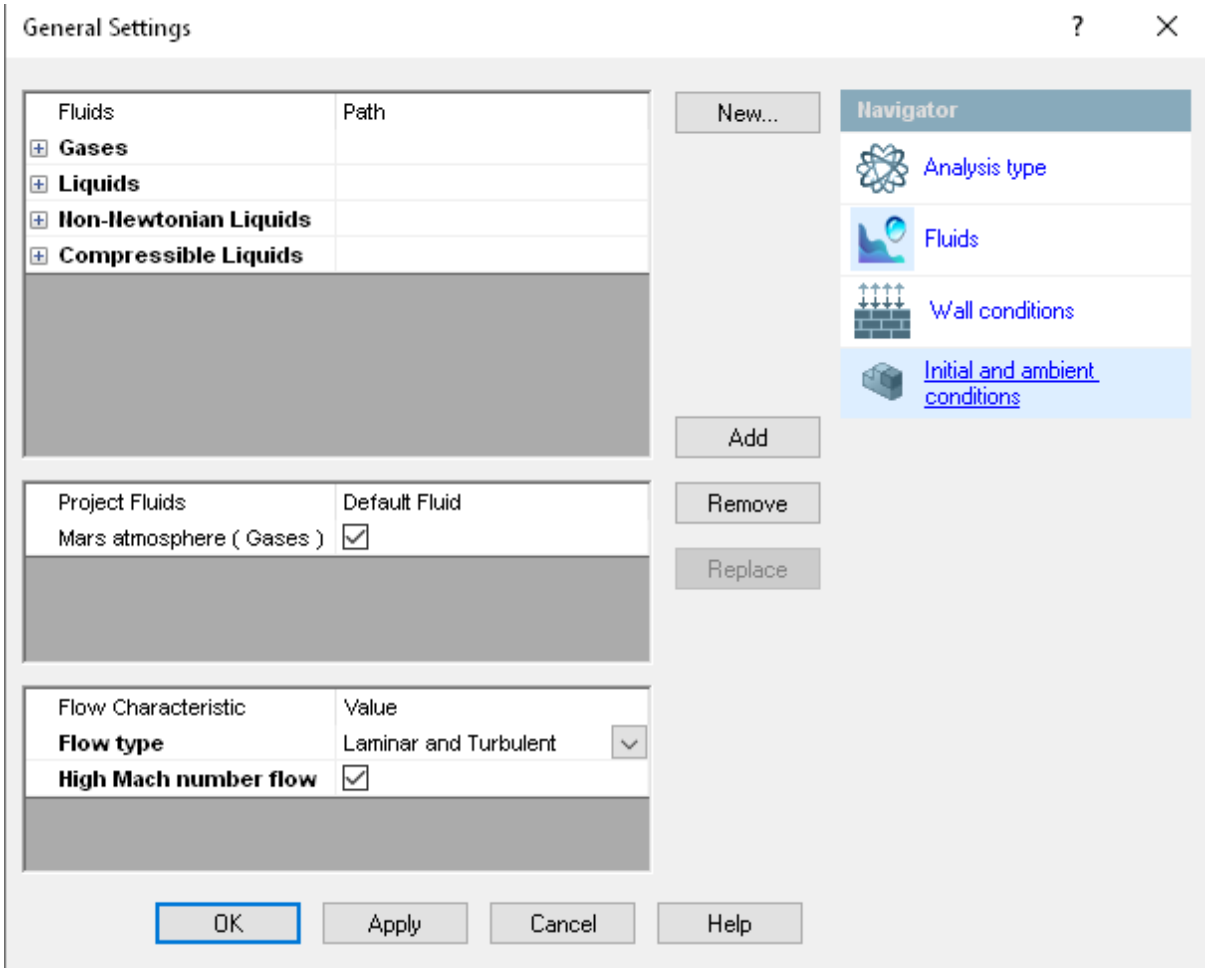

Figure 4.4. Fluids model.

Three distinct flow regimes were investigated to account for different possible boundary layer behaviors and to understand the sensitivity of the aerodynamic outputs to turbulence modeling:

- A fully laminar model, which assumes that the boundary layer remains stable and smooth throughout the body, a condition more likely in low Reynolds number flows at high altitudes or along short flow paths.
- A fully turbulent model, representing the opposite extreme, assuming that the flow transitions to turbulence immediately at the leading edge. This often leads to overestimated skin friction and heat transfer, providing conservative performance estimates.
- A transitional flow model that allows the flow to transition between laminar and turbulent behavior based on local flow parameters, as permitted by the integrated transition modeling of SolidWorks.

The thermal boundary condition applied to the waverider surface was a fixed wall temperature of 1000 K, consistent with the design assumptions in the University of Maryland's Martian waverider study (21). This value approximates radiative equilibrium conditions expected during hypersonic planetary entry. In addition, the waverider surface was assumed to be perfectly smooth, with zero surface roughness, to eliminate additional flow disturbances and match the baseline configuration used in the reference work.

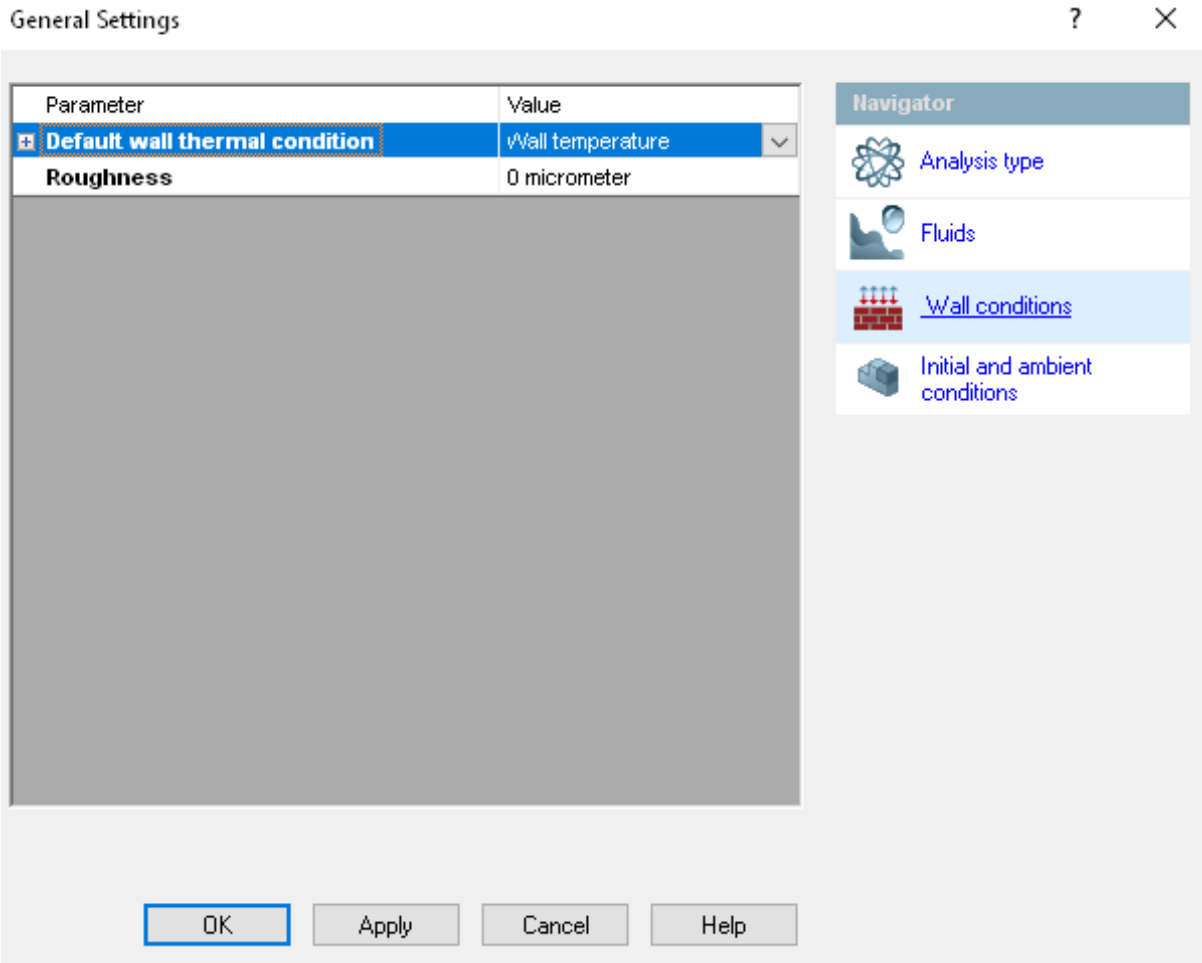

Figure 4.5. Wall condition.

To represent realistic Martian entry environments, the simulations were conducted at two representative altitudes: 20 km and 30 km. These altitudes were chosen because reference data is available for comparison of the simulation results. The ambient atmospheric conditions for each altitude were derived from data collected by NASA's Viking 1 mission, which provided one of the most reliable profiles of the Martian atmosphere following its landing in 1976. These conditions were implemented manually within the simulation environment and include:

At 20 km altitude: Ambient pressure of 205 Pa, ambient temperature of 116 K.

At 30 km altitude: Ambient pressure of 47 Pa, ambient temperature of 183 K. These parameters are presented in Figure 4.6, and ensure that the simulations reflect the thermal and dynamic state of the actual Martian atmosphere.

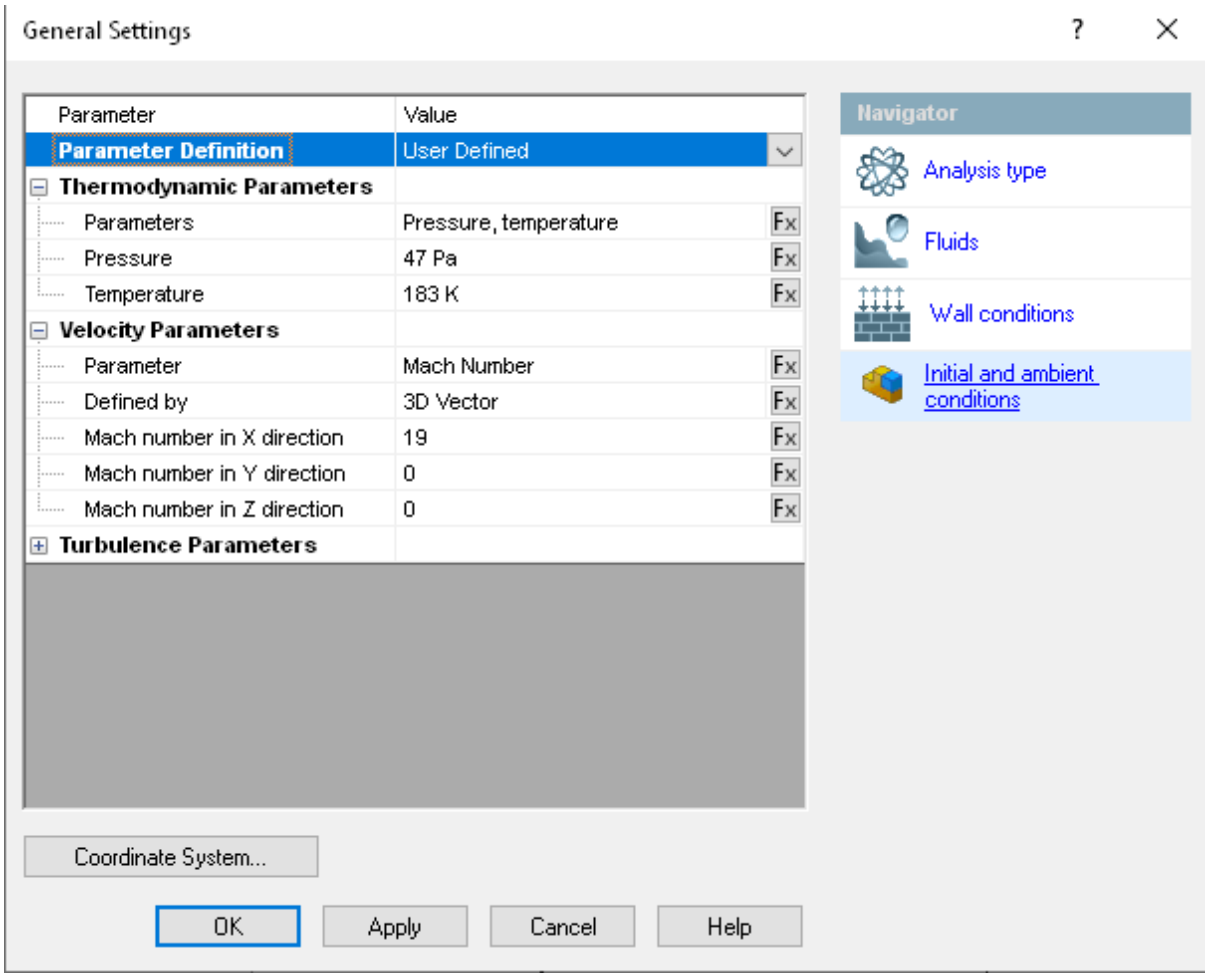

Figure 4.6. Initial and ambient conditions.

The freestream Mach number was fixed at Mach 19 for all simulation cases, consistent with expected entry velocities resulting from gravity-assist flybys or high-energy Mars transfer trajectories. The freestream flow vector was defined along the X-axis, representing level flight at a zero-degree angle of attack. While future work may consider varying angles of attack to study control and trim characteristics, this initial zero-angle assumption is consistent with the assumptions in the University of Maryland's Martian waverider study (21)..

For computational efficiency, the flow domain was reduced by symmetry. A symmetry plane was applied along the centerline of the vehicle, reducing the model to a half-domain without sacrificing accuracy due to the symmetric nature of both the geometry and the flow

field at zero angle of attack. This setup is shown in Figure 4.7, where the computational domain and mesh are visualized.

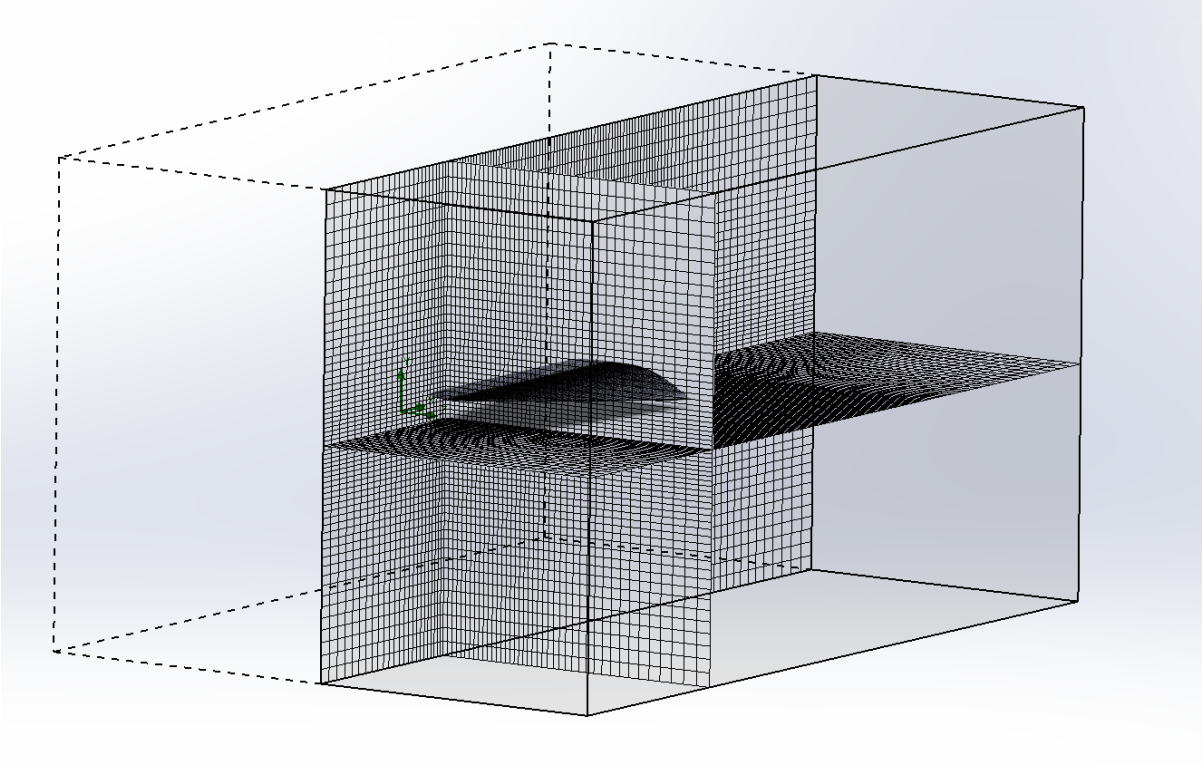

Figure 4.7. Computational domain and mesh.

The computational mesh was generated using SolidWorks' automatic meshing algorithm, which applies local refinement based on geometry curvature, flow gradients, and boundary proximity. The mesh was allowed to automatically densify near regions of high curvature (e.g., leading edges and compression surfaces), which is essential for capturing shock–boundary layer interaction and flow separation, especially in hypersonic flow fields. Although SolidWorks does not offer fine-grained control over boundary-layer inflation layers like specialized CFD packages (e.g., ANSYS Fluent or OpenFOAM), the automatic mesh has been validated in multiple external flow studies for producing accurate integral results such as drag and pressure distribution. Mesh independence was not explicitly tested in this initial study, but the literature (33) suggests that the default mesh setting in SolidWorks provides adequate resolution for preliminary aerodynamic evaluations in external flows.

In total, six simulation cases were executed to span the combination of altitude and flow regime parameters. These cases are summarized in the table below:

TABLE 4.1. Summary of CFD simulation cases in Mars atmosphere

Case	Altitude (km)	Flow Regime	Mach	Wall Temp (K)	AOA (°)
1	20	Laminar	19	1000	0
2	20	Turbulent	19	1000	0
3	20	Transitional	19	1000	0
4	30	Laminar	19	1000	0
5	30	Turbulent	19	1000	0
6	30	Transitional	19	1000	0

4.2 Results

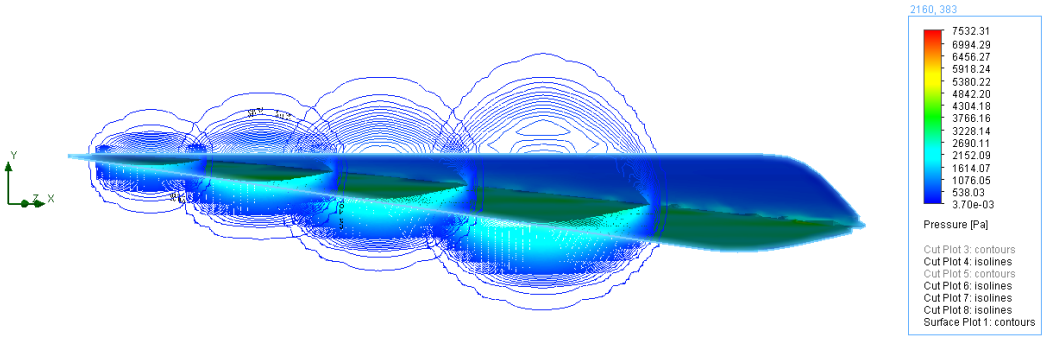

Figure 4.8. Fully laminar at 20 km.

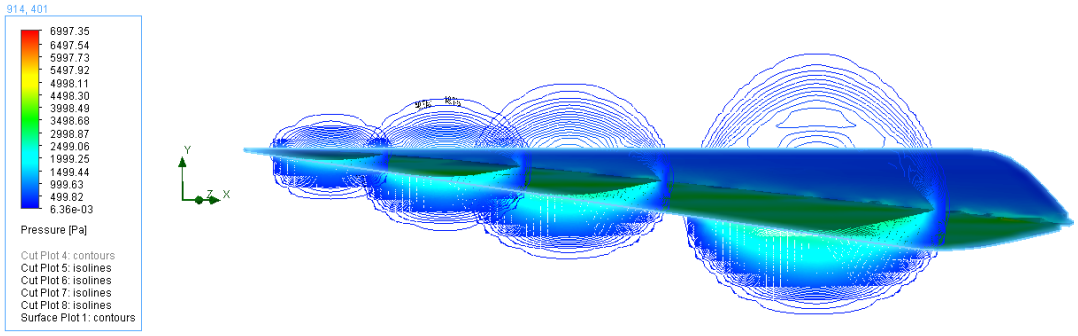

Figure 4.9. Fully turbulent at 20 km.

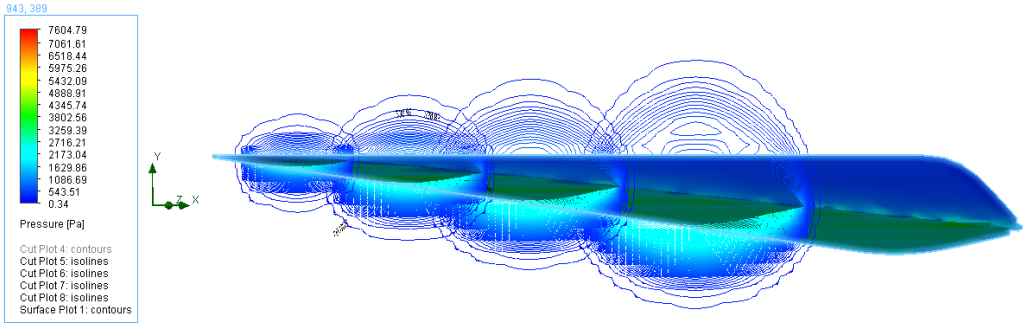

Figure 4.10. Transition at 20 km.

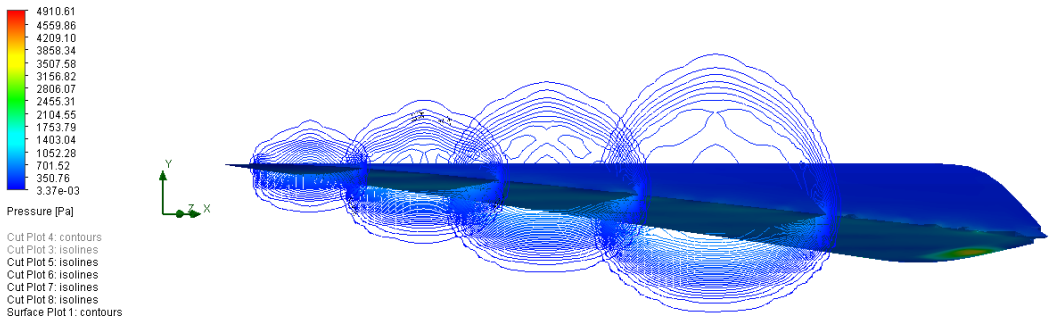

Figure 4.11. Fully laminar at 30 km.

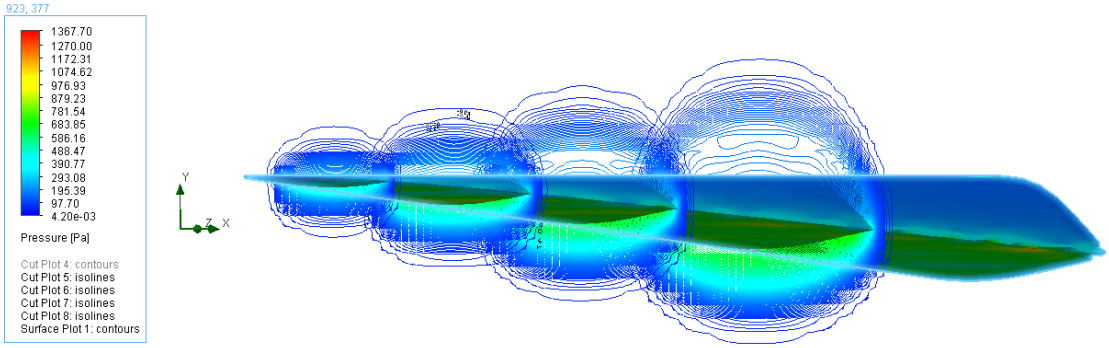

Figure 4.12. Fully turbulent at 30 km.

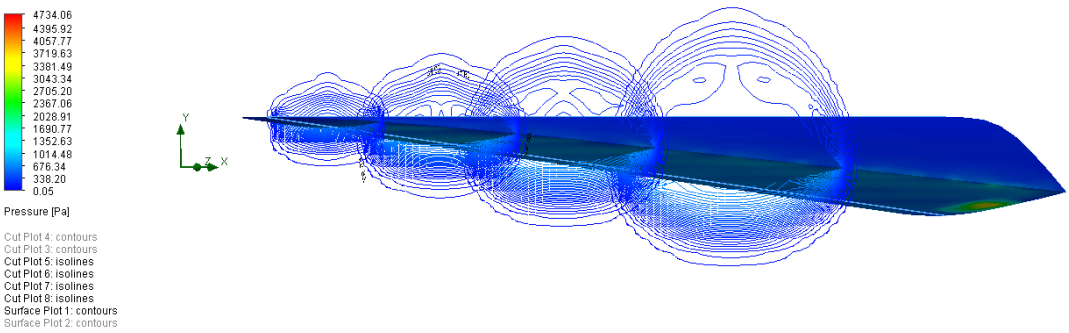

Figure 4.13. Transition at 30 km.

Figures 4.8 through 4.13 present the static pressure contours and isolines around the waverider geometry in the Martian atmosphere at Mach 19 for three different flow regimes: laminar, turbulent, and transitional, at two distinct altitudes: 20 km and 30 km. These visualizations provide critical information on the shock structure, flow field behavior, and aerodynamic loading experienced by the vehicle under hypersonic entry conditions.

Across all six images, a prominent feature is the presence of well-defined shock structures that remain mostly attached to the leading edges of the waverider. Although there is evidence of a weak, localized shock spillover near the leading edge of the waverider, particularly visible in some of the turbulent and high-altitude flow cases. This shock appears to extend slightly beyond the intended compression surface, failing to remain perfectly aligned with the vehicle's leading edge as designed. While minor, this deviation may result in a portion of the high-energy flow bypassing the lower surface, thereby reducing pressure recovery and diminishing lift generation in that region.

One plausible explanation for this effect is the presence of numerical integration errors inherent in the discretization methods used by SolidWorks Flow Simulation. Finite-volume solvers, particularly those relying on cell-centered schemes and default mesh settings, may struggle to resolve very sharp gradients—such as those present across a hypersonic shock—without sufficient mesh refinement. When the mesh resolution near the leading edge or within the shock region is too coarse, or when the numerical dissipation of the scheme is relatively high, the solver may smear or misalign the shock, causing a partial detachment or "leakage" of the shock over the surface.

Additionally, the simplified turbulence and transition models in SolidWorks may not fully capture the complex interactions between the shock and the boundary layer, further contributing to slight discrepancies in shock placement. These small deviations do not indicate

a failure of the solver, but rather reflect the limits of accuracy in capturing steep gradients within commercial CFD packages not explicitly tailored for high-fidelity hypersonic flow prediction. Although the observed shock spillover is minimal, it may result from a combination of numerical artifacts, mesh limitations, and modeling simplifications.

Nevertheless, this observation is consistent with the theoretical intent of the waverider configuration, which is designed to ride its own attached oblique shock wave to maximize lift and aerodynamic efficiency. The fact that the bow and oblique shocks are clearly attached—rather than detached or smeared—validates both the geometric fidelity of the conical waverider and the adequacy of the mesh and solver resolution in capturing shock behavior.

Another consistent trend observed in all cases is the significantly higher static pressure distribution along the lower surface of the waverider compared to the upper surface. This pressure differential is most pronounced near the leading edge and first compression surface, where flow impingement is strongest and compression is maximized. On the upper surface, pressures remain relatively low due to flow expansion and minimal surface interaction. This contrast between upper and lower surface pressures confirms that the waverider is generating net positive lift, even at zero angle of attack, as intended by its aerodynamic design.

Notably, the pressure contours also reveal secondary shock structures forming along surface deflections and compression ramps on the underside of the vehicle. These features contribute to additional pressure buildup on the lower surface, enhancing lift further. In several cases, shock reflections or shock-shock interactions can be identified downstream, particularly in the turbulent and transitional flow regimes, where boundary layer development and shock-boundary layer interaction become more complex.

At the higher altitude of 30 km, the images show slightly more diffuse pressure gradients and weaker shock strength, consistent with the reduced atmospheric density at this elevation. While the shock remains attached in all cases, the bow shock stand-off distance appears slightly greater, and overall pressure levels are lower—particularly in the laminar and turbulent cases—demonstrating the sensitivity of hypersonic aerodynamic behavior to ambient density.

These pressure contour plots provide clear visual confirmation of key aerodynamic principles central to the waverider concept. The attachment of oblique shocks, the high-pressure recovery on the lower surface, and the consistent lift generation across varying flow regimes and altitudes all support the aerodynamic viability of the conical waverider for Mars entry missions. These findings reinforce the waverider theory and further validate the use of SolidWorks Flow Simulation for qualitative hypersonic flow field analysis.

The aerodynamic force results in this study were obtained from SolidWorks Flow Simulation by evaluating the total integrated forces acting on the external surface of the waverider geometry. These forces are calculated by numerically integrating both pressure forces (arising from the normal component of the stress tensor) and viscous shear forces (tangential components) across the entire surface mesh. The result is a total aerodynamic force vector resolved in the Cartesian coordinate system defined within the simulation environment, where the X-axis is aligned with the freestream flow direction, and the Y-axis represents the vertical (lift-producing) direction.

The total lift force was determined by extracting the Y-component of the total aerodynamic force vector. This component corresponds to the net vertical force generated due to pressure differentials between the lower (compression) and upper (freestream-facing) surfaces of the waverider. Because the waverider is designed to ride its attached shockwave and maintain high pressure on the underside of the vehicle, it generates lift without requiring large angles of attack. In this study, the vehicle was evaluated at zero angle of attack, simulating level flight, and the lift arose purely from the shaping and flow compression inherent to the waverider configuration.

The drag force, acting in opposition to the direction of motion, was computed as the X-component of the total force vector. SolidWorks separates the total drag into two components:

Pressure drag (also called wave drag in hypersonic regimes), which is derived from the X-component of the normal force vector. This drag arises primarily from the vehicle's interaction with compressible shock waves, expansion fans, and the pressure gradients generated by the sharp leading edges and compression surfaces. In hypersonic flow, pressure drag can be particularly dominant due to the strong bow shocks and highly compressed flow regions.

Friction drag, which is calculated based on the viscous shear stresses acting tangentially across the waverider surface. SolidWorks Flow Simulation automatically computes the local shear stress at each surface element, which is then integrated over the full surface area to obtain the total viscous drag force. This component becomes significant in high-speed flows with large wetted surface areas, such as those found in waverider configurations. In planetary atmospheres like that of Mars, where Reynolds numbers are relatively low, friction drag can constitute a larger percentage of total drag compared to similar vehicles flying in denser Earth conditions.

By summing the pressure drag and friction drag, the total drag force is obtained. This total drag aligns with the X-component of the net aerodynamic force vector and represents the actual retarding force the vehicle experiences during flight. The ability to distinguish between pressure and viscous contributions to drag is essential for evaluating design efficiency and for identifying aerodynamic optimization opportunities.

Summary of the lift and drag components:

- Lift $\rightarrow$ Y-component of the total force
- Total Drag $\rightarrow$ X-component of the total force
- Pressure Drag $\rightarrow$ X-component of normal force
- Friction Drag $\rightarrow$ Derived from integrated shear force on all surfaces

This decomposition of forces not only facilitates the calculation of key aerodynamic coefficients, such as the lift coefficient (C_L), the pressure drag coefficient (C_{D_p}), the friction drag coefficient (C_{D_f}), and the total drag coefficient $(C_{D_{total}})$, but also allows a nuanced analysis of the lift-to-drag ratio (L/D), a primary performance metric for hypersonic vehicles performing aeroassist maneuvers or atmospheric entry.

After the surface forces were calculated from the CFD simulation, they were normalized to obtain dimensionless aerodynamic coefficients, allowing for meaningful comparison across different flow conditions, vehicle sizes, and altitudes. This normalization process involved converting the raw lift and drag forces into their respective coefficients of lift (C_L) and

drag ((C_D)), which are the standard parameters used in aerodynamic analysis to describe performance independently of scale.

The normalization was achieved by dividing the computed forces by the product of the dynamic pressure (q) and the reference area (S) of the waverider. The dynamic pressure is a function of the freestream density (ρ) and velocity (u), and is given by:

$$q = \frac{1}{2}\rho u^2 \tag{4.1}$$

TABLE 4.2. Dynamic pressure parameters

Parameter	**20 km**	**30 km**
$S\ [m^2]$	5.7686×10^{-4}	5.7686×10^{-4}
$\rho\ \left[\frac{kg}{m^3}\right]$	9.25×10^{-3}	1.34×10^{-3}
$u\ \left[\frac{m}{s}\right]$	3225.708	4051.554

This represents the kinetic energy per unit volume of the oncoming flow and serves as a reference quantity for force based coefficients in compressible flow. The reference area *S*, in this case, is the wetted surface area of the waverider, which is appropriate for hypersonic vehicles where the entire body interacts with the flow and contributes to both lift and drag production.

The lift coefficient (C_L) and drag coefficient (C_D) are thus calculated using the following relationships:

$$C_L = \frac{L}{qS} \tag{4.2}$$

$$C_D = \frac{D}{qS} \tag{4.3}$$

where L is the lift force (Y-component of the total aerodynamic force), and D is the total drag force (X-component of the total aerodynamic force, including both pressure and friction components).

These coefficients provide a normalized basis for evaluating aerodynamic efficiency across a range of test conditions. For example, the ratio $\frac{C_L}{C_D}$, commonly referred to as the lift-to-drag ratio (L/D), is a key performance metric used to assess a vehicle's ability to produce lift relative to its aerodynamic resistance. Maximizing the L/D directly contributes to extending glide range, improving trajectory control, and minimizing heat loads through optimized atmospheric flight profiles. By converting the raw forces to non-dimensional coefficients, ensures that the aerodynamic results are directly comparable with existing literature'

The results of the simulation, including both the raw aerodynamic forces (lift, pressure drag, friction drag, and total drag) and their corresponding dimensionless aerodynamic coefficients, are systematically summarized in the tables presented below. These values

were extracted directly from SolidWorks Flow Simulation post-processing tools, which compute surface-integrated force vectors and decompose them into their respective Cartesian components.

Each table reports the aerodynamic performance of the waverider configuration under specific Martian atmospheric conditions—at altitudes of 20 km and 30 km, and across three distinct flow regimes: laminar, turbulent, and transitional. For each case, the raw force outputs are presented in units of Newtons (N), reflecting the total lift force, pressure drag, friction drag, and the resultant total drag acting on the waverider and their nondimensional coefficients during hypersonic flight at Mach 19.

TABLE 4.3. Aerodynamic outputs for hypersonic waverider at 20 km Mars altitude (Mach 19)

Parameter	Laminar	Turbulent	Transitional
Lift, L [N]	0.502	0.514	0.503
Pressure Drag, D_p [N]	0.081	0.081	0.081
Friction Drag, D_f [N]	0.168	0.177	0.166
Total Drag, D_{tot} [N]	0.249	0.258	0.247
C_L	0.0180	0.0185	0.0181
C_{D_p}	0.00291	0.00291	0.00291
C_{D_f}	0.00604	0.00638	0.00598
$C_{D_{tot}}$	0.00895	0.00929	0.00889
L/D_p	6.19	6.34	6.21
L/D_f	2.99	2.90	3.03
L/D_{tot}	2.01	1.99	2.03

TABLE 4.4. Aerodynamic outputs for hypersonic waverider at 30 km Mars altitude (Mach 19)

Parameter	Laminar	Turbulent	Transitional
Lift, L [N]	0.121	0.111	0.121
Pressure Drag, D_p [N]	0.021	0.020	0.021
Friction Drag, D_f [N]	0.094	0.093	0.115
Total Drag, D_{tot} [N]	0.115	0.113	0.136
C_L	0.0191	0.0175	0.0191
C_{D_p}	0.0033	0.0032	0.0033
C_{D_f}	0.0148	0.00147	0.0181
$C_{D_{tot}}$	0.0184	0.0178	0.0214
L/D_p	5.76	5.55	5.76
L/D_f	1.29	1.19	1.05
L/D_{tot}	1.05	0.982	0.89

4.3 Analysis

A particularly notable outcome from the CFD simulations is observed in Table 4.3, which summarizes the aerodynamic performance at 20 km altitude in the Martian atmosphere. Counterintuitively, the fully turbulent model produced the highest lift, exceeding the laminar and transitional models. This result may be explained by the increased momentum transport

within a turbulent boundary layer. In high-speed external flows, turbulent eddies enhance the mixing of momentum perpendicular to the wall, making the boundary layer more robust and resistant to flow separation. This phenomenon leads to improved pressure recovery on the compression surface of the waverider and results in increased lift.

However, under hypersonic conditions, the boundary layer is already heavily energized due to the high freestream kinetic energy, and flow separation is less likely to occur even in laminar regimes. Therefore, the increase in lift from turbulence may not solely be due to delayed separation, but rather due to numerical factors within the turbulence model amplifying the surface pressure differentials, particularly on the lower (compression) surface of the vehicle.

As expected, the fully turbulent model also generated the highest friction drag, attributed to the enhanced shear forces resulting from a turbulent boundary layer. In contrast to laminar flow, where near-wall velocity gradients are smoother, turbulent flow features steeper gradients and higher eddy viscosity, both of which increase wall shear stress. Despite this, pressure drag remained nearly constant across all three cases. This indicates that the shock structure and pressure distribution—primarily governed by the vehicle's geometry and Mach number—were largely unaffected by the turbulence model.

Due to the significant rise in friction drag, the overall lift-to-drag ratio (L/D) for the turbulent case was the lowest among the three. While the increased lift is favorable, the accompanying drag penalty offsets any aerodynamic gains.

Interestingly, the transitional model yielded the highest L/D, representing the optimal trade-off between lift enhancement and drag minimization. This suggests that the transitional flow may have energized the boundary layer just enough to delay or mitigate separation—similar to the turbulent case—but without fully incurring the high skin friction penalties associated with fully turbulent flow. This behavior reinforces the importance of accurate transition modeling in hypersonic vehicle simulations, where small changes in surface shear and pressure gradients can have large impacts on overall aerodynamic efficiency.

Surprisingly, the laminar case produced the lowest lift but also showed relatively high friction drag, which deviates from expected trends. Typically, laminar flows yield lower skin friction due to smoother velocity profiles. However, in hypersonic flows, this may be offset by localized thermal effects, low Reynolds numbers, and potentially under-resolved boundary layer behavior in the CFD mesh, leading to overestimation of shear forces.

At 30 km altitude, as shown in Table 4.4, the flow regime behavior shifts. At this higher altitude, where the Martian atmosphere is thinner and freestream density is lower, the turbulent case generated the least lift. This is in contrast to the 20 km results and may be due to diminished boundary layer development, as the low-density environment provides less mass and energy to support a strong turbulent boundary layer. The lack of strong momentum exchange in the boundary layer reduces compression surface pressure recovery, thus lowering lift.

Both the laminar and transitional models produced identical lift values, suggesting that at this altitude, the effect of flow regime on pressure-driven lift may be minimized due to the already thin atmosphere.

However, a significant departure from expected trends is that the transitional case produced the highest friction drag, surpassing even the fully turbulent model. This could be due to localized shock–boundary layer interactions, which are known to occur in hypersonic flow over curved or compression surfaces. If captured by SolidWorks Flow Simulation's transition model, these interactions could cause intensified shear stress in transitional zones—leading to spikes in skin friction. Such interactions are highly sensitive to surface curvature, thermal gradients, and flow alignment, and are known contributors to drag and surface heating in reentry applications.

Notably, the laminar case achieved the highest L/D at 30 km, which aligns with expectations. In low-density atmospheres, turbulence tends to be suppressed, and the reduced energy available to sustain turbulence makes laminar flow more efficient. Additionally, the low atmospheric density results in lower dynamic pressure and therefore reduced skin friction—favoring laminar flow in terms of drag minimization.

These findings highlight the sensitivity of aerodynamic performance to flow regime modeling, especially in the unique atmospheric conditions of Mars. The fully turbulent model enhances lift but at the cost of higher friction drag, lowering efficiency. The transitional model provides an ideal balance, especially at moderate altitudes where it can leverage turbulent benefits without the full penalties. At higher altitudes, laminar flow becomes more efficient, and turbulence contributes little to performance improvement.

$$\text{Percent Difference} = \frac{|X_{\text{sim}} - X_{\text{ref}}|}{\frac{X_{\text{sim}} + X_{\text{ref}}}{2}} \times 100 \tag{4.4}$$

TABLE 4.5. Percent difference between reference values (20 km)

	Reference	**Laminar**	**% Diff**	**Turbulent**	**% Diff**	**Transitional**	**% Diff**
C_L	0.0342	0.0180	62	0.0185	60	0.0181	61
C_{D_p}	0.0039	0.00291	28	0.00291	28	0.00291	28
C_{D_f}	0.0013	0.00604	129	0.00638	132	0.00598	129
$C_{D_{tot}}$	0.0052	0.00895	54	0.00929	57	0.00889	53
L/D_p	8.88	**6.19**	35	**6.34**	33	**6.21**	35
L/D_f	26.3	2.99	159	2.90	160	3.03	159
L/D_{tot}	**6.63**	2.01	107	1.99	108	2.03	106

TABLE 4.6. Percent difference between reference values (30 km)

	Reference	**Laminar**	**% Diff**	**Turbulent**	**% Diff**	**Transitional**	**% Diff**
C_L	0.334	0.0191	178	0.0175	180	0.0191	178
C_{D_p}	.00363	0.0033	9	0.0032	14	0.0033	9
C_{D_f}	.00266	0.0148	139	0.00147	139	0.0181	149
$C_{D_{tot}}$	.00629	0.0184	97	0.0178	96	0.0214	109
L/D_p	9.2	**5.76**	46	**5.55**	49	**5.76**	46
L/D_f	12.554	1.29	163	1.19	165	1.05	169
L/D_{tot}	**5.38**	1.05	135	0.982	138	0.89	143

When comparing the lift-to-drag ratios obtained from the current CFD simulations in SolidWorks Flow Simulation to the reference values published by the University of Maryland's study on the Martian waverider (21), the results are wildly inconsistent, especially in the context of total aerodynamic efficiency. Tables 4.5 and 4.6 present a detailed comparison of all key aerodynamic coefficients along with the percent difference of each quantity relative to the reference case.

The most striking discrepancy appears in the final row of both tables, where the computed lift-to-drag ratios diverge from the reference values by over 100% in all flow regimes. In particular, the lift generated in all SolidWorks simulations is significantly lower than the reference values, with the percent difference in lift more than doubling between 20 km and 30 km altitudes. This increasing disparity with altitude may reflect SolidWorks' difficulty in resolving accurate lift forces under extreme low-density conditions, common in the Martian upper atmosphere, especially when relying on RANS-based turbulence models not originally designed for such thin flow environments.

One potential explanation for this discrepancy lies in the treatment of the waverider base. The University of Maryland study have excluded the contribution of the base surface in their aerodynamic calculations, an omission that can significantly affect drag predictions. In hypersonic flows, the base of the waverider is a major contributor to pressure drag due to low pressure recovery and potential flow separation in the aft region. If base drag is excluded in the reference model but included in the SolidWorks simulations, this would artificially inflate the drag in the present results and explain the large deviations in C_D and L/D values.

Despite these discrepancies, the pressure drag values computed in SolidWorks show relatively small deviations from the reference, confirming the University of Maryland's assumption in which the drag contribution from the waverider base is negligible. In contrast, the friction drag is consistently over predicted across all altitudes and flow regimes. As discussed previously, this may stem from SolidWorks Flow Simulation capturing localized shock–boundary layer interactions, especially near surface discontinuities and sharp gradients. These interactions are known to cause spikes in skin friction, particularly in high-speed, high-Reynolds-number boundary layers where laminar-turbulent transition or shock impingement can intensify wall shear stress.

A particularly insightful observation emerges when only pressure drag is considered in the lift-to-drag ratio calculation. In this simplified form, the simulated L/D_p values closely match the total L/D values reported in the reference study, as shown in bold in the tables. This convergence strongly implies that the discrepancies in L/D are driven almost entirely by excessive friction drag in the SolidWorks model, rather than differences in pressure-induced forces. Therefore, the reference study's simplification of friction drag, possibly due to the use of inviscid or semi-viscous approximations, may explain why their total L/D values align more closely with SolidWorks' L/D_p values rather than with full drag-inclusive results.

This finding underscores an important limitation in comparing viscous-optimized waverider performance across different CFD frameworks. High-fidelity viscous modeling—especially in thin planetary atmospheres like Mars—requires not only accurate turbulence modeling but also careful treatment of wall boundary conditions, thermal loads, and transition behavior, all

of which can significantly affect shear forces and therefore drag. Furthermore, it highlights the sensitivity of hypersonic vehicle performance metrics to the treatment of the vehicle's aft geometry, which in high-Mach environments, contributes disproportionately to drag and thermal loading.

While SolidWorks Flow Simulation appears capable of predicting pressure-related aerodynamic behavior with reasonable accuracy, its estimates for friction drag may be overly conservative, leading to underpredicted lift-to-drag ratios. This work supports the use of SolidWorks for preliminary hypersonic design and entry analysis, but also emphasizes the need for supplementary validation using higher-fidelity solvers or experimental data when precise drag breakdown and heat transfer characteristics are critical for mission design. Further investigation into mesh resolution near boundary layers and advanced wall modeling could help reduce these discrepancies in future work.

5. Conclusion

This project presented a computational fluid dynamics (CFD) analysis of a viscous-optimized conical waverider designed for hypersonic entry into the Martian atmosphere. The waverider concept, originally introduced by Terence Nonweiler and later refined by Bowcutt, Anderson, and others, has long been recognized for its potential to achieve high lift-to-drag ratios (L/D) by maintaining an attached shock wave along the leading edge. This design principle enables superior aerodynamic efficiency, especially in high-Mach, high-altitude flight regimes, where traditional blunt-body configurations become drag-dominated and offer limited control.

The primary objective of this study was to evaluate the aerodynamic performance of such a waverider under realistic Martian entry conditions and to assess the capabilities and limitations of using SolidWorks Flow Simulation as a CFD tool for hypersonic planetary entry modeling. SolidWorks, while not traditionally used for hypersonic flow analysis, offers a user-friendly and CAD-integrated platform suitable for preliminary aerodynamic investigations, particularly in educational or early-phase design settings.

The waverider model was based on previous work of a viscous-optimized design developed at the University of Maryland. The simulations included modeling hypersonic flow at Mach 19 across two altitudes representative of Mars' upper atmosphere, 20 km and 30 km, across three different flow regimes: laminar, turbulent, and transitional. These conditions were selected to evaluate how atmospheric density and boundary layer development influence the lift, drag, and overall aerodynamic efficiency of the vehicle.

The CFD results provided several key insights:

- At 20 km altitude, the higher atmospheric density enabled greater aerodynamic force generation. The fully turbulent model yielded the highest lift due to increased momentum mixing in the boundary layer, which enhances pressure recovery on the lower surface. However, this came at the cost of significantly increased skin friction drag, resulting in the lowest L/D ratio among the three regimes.
- The transitional flow regime consistently delivered the best balance between lift and drag, achieving the highest L/D ratios at both altitudes. This outcome suggests that controlled boundary layer transition, whether natural or induced, can offer performance benefits by energizing the flow without incurring the full penalties of turbulence.
- At 30 km altitude, all aerodynamic forces were significantly reduced due to the thinner atmosphere. Interestingly, the turbulent model performed worse in terms of lift generation, possibly because the reduced atmospheric density weakens turbulent mixing. The laminar case exhibited the highest L/D at this altitude, demonstrating that turbulence may not be beneficial in extremely low Reynolds number environments.
- Friction drag was the dominant contributor to total drag in nearly all simulation cases, with the pressure drag remaining nearly constant. This result underscores the importance of accurately modeling wall shear stress in hypersonic CFD, particularly when using simulation tools that rely on wall functions or approximate turbulence models.

- Comparing the SolidWorks results to the University of Maryland reference data revealed notable discrepancies in total drag and L/D values. While pressure drag closely matched the reference data, friction drag was consistently overpredicted. This may be attributed to SolidWorks' tendency to overestimate shear stress due to coarse mesh resolution near walls or limitations in turbulence and transition modeling.
- A particularly insightful result emerged when only the pressure drag was used to compute L/D. In this case, the computed ratios more closely matched the reference values, suggesting that the main source of deviation lies in the overprediction of skin friction rather than in the resolution of the pressure field. This finding highlights the need for careful interpretation of friction drag in simulations conducted using general-purpose CFD software.

Overall, this study demonstrates that SolidWorks Flow Simulation can provide reasonable estimates for hypersonic aerodynamic behavior in Martian conditions, particularly in terms of pressure-related forces. The software's limitations are more evident in its handling of skin friction and transitional flow dynamics, which are critical in low-density environments like Mars. Nevertheless, for preliminary design studies, parametric comparisons, or educational purposes, SolidWorks can serve as a valuable tool. The research also reinforces several broader themes in hypersonic vehicle design:

- Viscous effects are not just secondary corrections to inviscid models—they are integral to accurate performance prediction in planetary entry scenarios.
- Boundary layer transition modeling can have a profound impact on drag prediction and, consequently, on mission-critical parameters such as entry heating, deceleration rates, and trajectory shaping.
- Hypersonic CFD must balance model fidelity, computational cost, and solver capability. In design phases where high accuracy is not yet required, accessible platforms like SolidWorks can bridge the gap before high-fidelity tools such as DPLR, US3D, or FUN3D are employed.

5.1 Recommendations for Future Work

This investigation opens the door for several areas of future research:

- **Mesh refinement studies** should be conducted to assess the sensitivity of wall shear stress and boundary layer resolution to grid density near the surface, particularly around leading edges and compression surfaces.
- **Alternative turbulence models**, such as k -ω SST or Spalart-Allmaras, may be explored to determine whether improved friction drag predictions can be achieved.
- **Higher-fidelity solvers** that support advanced transition modeling and real gas effects should be used to validate the results obtained here. This would help determine how much of the observed discrepancy is due to solver limitations versus modeling assumptions.
- **Parametric geometry variations**, including angle of attack, planform curvature, and leading-edge bluntness, could be studied to identify optimal configurations for Martian entry and aero-gravity assist missions.

- **Thermal analysis coupling** with structural materials and TPS (thermal protection systems) could extend the model to assess survivability, not just aerodynamic performance.

References

[1] Anderson, J. D., *Fundamentals of Aerodynamics*, chap. Elements of Hypersonic Flow, McGraw-Hill Education, New York, 5th ed., 2011, p. 880.

[2] Lunan, D., "Waverider, A Revised Chronology," *AIAA Paper*, July 2015.

[3] Ferguson, F., Dasque, N., and Dhanasar, M., "The Design, Analysis and Performance Evaluation of Waverider Configurations for Hypersonic Vehicle Applications," *53rd AIAA Aerospace Sciences Meeting*, January 2015.

[4] Girdwood, I., "Prof. Terence Nonweiler with origami 'teaching aid," *theorkneynews*, 1988, https://theorkneynews.scot/2022/11/27/waverider-part-1-a-spacecraft-in-waiting/.

[5] Cockrell Jr, C., "Interpretation of Waverider Performance Data Using Computational Fluid Dynamics," *23rd Fluid Dynamics, Plasmadynamics, and Lasers Conference*, 1993.

[6] Anderson, J. D., *Fundamentals of aerodynamics*, McGraw-Hill Education, New York, 5th ed., 2011, p. 882.

[7] Bryant, R., Dillon, J., Grewe, G., Mcmorrow, J., Melton, C., Rainey, G., Rinko, J., Singh, D., and Yen, T., "Project Exodus," *NASA Technical Report Server*, May 1990.

[8] Anderson, J. D., *Fundamentals of aerodynamics*, McGraw-Hill Education, New York, 5th ed., 2011, p. 886.

[9] Schwelkart, L., "The Hypersonic Revolution. Case Studies in the History of Hypersonic Technology," *volume 3: The quest for the orbital jet: The national aero-space plane program (1983-1995)*, Air Force Historical Studies Office, 1998.

[10] "Hypersonic Vehicle Applications," *Aerospace Web*, 2023, https://aerospaceweb.org/design/waverider/examples.shtml.

[11] Barthelemy, R. R., "The National Aerospace Plane Program: A Revolutionary Concept," *Johns Hopkins APL Technical Digest*, Vol. 11, No. 3 and 4, 1990.

[12] "Artist's concept of X-43A with scramjet attached to the underside," *Wikipedia*, 1999, https://en.wikipedia.org/wiki/NASA_X-43#/media/File:X43a2_nasa_scramjet.jpg.

[13] "Hypersonic Vehicle Design," *Aerospace Web*, 2025, https://aerospaceweb.org/design/waverider/design.shtml.

[14] Anderson, J. D., *Fundamentals of Aerodynamics*, chap. Oblique Shocks and Expansion Waves, McGraw-Hill Education, New York, 5th ed., 2011, p. 643.

[15] Csank, J. and Stueber, T., "A Turbine Based Combined Cycle Engine Inlet Model and Mode Transition Simulation Based on HiTECC Tool," *NASA Technical Reports Server*, 2012.

[16] "X-15 after igniting rocket engine," *Wikipedia*, 1959, https://en.wikipedia.org/wiki/North_American_X-15.

[17] "X-43A and Pegasus Booster Rocket Attached to B-52," *NASA*, 2004, https://www.nasa.gov/image-article/x-43a-pegasus-booster-rocket-attached-b-52/.

[18] "Illustration of Hypersonic Test Vehicle (HTV) 2 reentry phase," *Wikipedia*, 2010, https://en.wikipedia.org/wiki/DARPA_Falcon_Project.

[19] "Buran OK-1.01 orbiter general layout," *Wikipedia*, 2020, https://en.wikipedia.org/wiki/Buran_(spacecraft).

[20] "Xingkong-2 / Starry Sky 2," *globalsecurity*, 2021, https://www.globalsecurity.org/wmd/world/china/xingkong-2.htm.
[21] Anderson, J. J., Lewis, M., Kothari, A., , and Corda, S., "Hypersonic Waveriders for Planetary Atmospheres," *Journal of Spacecraft and Rockets, Vol. 28*, JULY-AUGUST 1991.
[22] "Conical Waverider Designed for Mars," *Ultimaker Thingiverse*, September 2015, https://www.thingiverse.com/thing:1012227.
[23] Anderson Jr., J. D., *Fundamentals of Aerodynamics*, McGraw-Hill, 2011.
[24] Corda, S., *Viscous Optimized Hypersonic Waveriders Designed from Flows Over Cones and Minimum drag Bodies*, Master's thesis, University of Maryland College Park, 1988.
[25] Walz, A., *Boundary Layers of Flow and Temperature*, M.I.T. Press, Cambridge, Mass, 1969.
[26] Eckert, E. R. G., "Engineering Relations for Heat Transfer and Friction in High-Velocity Laminar and Turbulent Boundary-Layer Flow Over Surfaces With Constant Pressure and Temperature," *Transactions of the ASME, Vol. 78, No. 6*, Aug. 1956.
[27] K. G. Bowcutt, J. D. Anderson, D. C., "Viscous Optimized Hypersonic Waveriders," *AIAA 25th Aerospace Sciences Meeting*, 1987.
[28] Bowcutt, K. G., *Optimiaztion of Hypersonic Waveriders Derived from Cone Flows Including Viscous Effects*, Ph.D. thesis, University of Maryland, 1986.
[29] White, F., *Viscous Fluid Flow*, McGraw-Hill, New York, 1974, pp. 653–657.
[30] DiCristina, V., "Three-Dimensional Laminar Boundary Transition on a Sharp 8 Degree Cone at Mach 10," *AIAA Journal, Vol. 8*, May 1970, p. 855.
[31] Harris, J. and Blanchard, O., "Computer Program for Solving Laminar, Transitional, and Turbulent Compressible Boundary Layer Equations for Two Dimensional and Axisymnetric Flows," Tech. rep., NASA, 1982.
[32] "SolidWorks Flow Simulation," Tech. rep., Dassault Systemes, 2021.
[33] Sobachkin, A. and Dumnov, G., "Numerical Basis of CAD-Embedded CFD," Tech. rep., SolidWorks, 2014.
[34] Modest, M. F., *Radiative Heat Transfer (3rd ed.)*, Academic Press, 2013.

Appendix A.
Matlab Code for % Difference Calculations

```
clc
clear
close all
%% 20

rho=9.25e-03;
u=3225.708;
L=[.502 .514 .503];
D_p=[.081 .081 .081];
D_f=[.168 .177 .166];
D_tot=D_p+D_f;

S=576.85786/1000^2;
Q=.5*rho*u^2;


CL=L/(Q*S);
CD_p=D_p/(Q*S);
CD_f=D_f/(Q*S);
CD_tot=CD_p+CD_f;

LD_p=CL./CD_p;
LD_f=CL./CD_f;
LD=CL./CD_tot;

ref=[.0342  .00515-.0013 .0013 .00515 .0342/(.00515-.0013)
   .0342/.0013 6.63]';
x=[CL; CD_p; CD_f; CD_tot; LD_p; LD_f; LD;];
xref=repelem(ref,1,3);
y=(xref+x)/2;
PerD=abs(xref-x)./y*100;
%% 30

rho=1.34e-03;
u=4051.554;
L=[.121 .111 .121];
D_p=[.021 .02 .021];
D_f=[.094 .093 .115];
```

```
D_tot=D_p+D_f;

S=576.85786/1000^2;
Q=.5*rho*u^2;


CL=L/(Q*S);
CD_p=D_p/(Q*S);
CD_f=D_f/(Q*S);
CD_tot=CD_p+CD_f;

LD_p=CL./CD_p;
LD_f=CL./CD_f;
LD=CL./CD_tot;

ref=[.334 .00363 .00266 .00629 9.2 12.554 5.38]';
x=[CL; CD_p; CD_f; CD_tot; LD_p; LD_f; LD;];
xref=repelem(ref,1,3);
y=(xref+x)/2;
PerD=100*abs(xref-x)./y;
```